

Thermal effects on particle deposition in microchannels

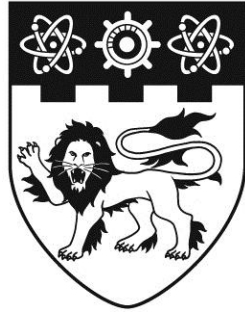
Yan, Zhibin

2016

Yan, Z. (2016). Thermal effects on particle deposition in microchannels. Doctoral thesis, Nanyang Technological University, Singapore.

<https://hdl.handle.net/10356/68632>

<https://doi.org/10.32657/10356/68632>



**NANYANG
TECHNOLOGICAL
UNIVERSITY**

**THERMAL EFFECTS ON PARTICLE DEPOSITION IN
MICROCHANNELS**

YAN ZHIBIN

SCHOOL OF MECHANICAL AND AEROSPACE ENGINEERING

2016

THERMAL EFFECTS ON PARTICLE DEPOSITION IN MICROCHANNELS

YAN ZHIBIN

School of Mechanical and Aerospace Engineering

A thesis submitted to the Nanyang Technological University
in partial fulfillment of the requirement for the Degree of
Doctor of Philosophy

2016

To the memory of my mother

Acknowledgements

First and foremost, I would like to acknowledge the guidance and support of my supervisors: Professors Huang Xiaoyang and Charles Yang Chun. Without their precious suggestions, I would not have worked out so many problems in the project. They have shared with me their priceless research experiences, and always encouraged me to have a critical thinking and attain essential insights on my research. I always obtain inspiring ideas through discussions with them. I also would like to thank Prof. Fei Duan for his constant encouragement and help during my study in NTU.

I would like to appreciate the financial support received from Nanyang Technological University. Without the scholarship, this research would not have been feasible.

I also acknowledge technical staff, Messrs. Yuan Kee Hock and Yap Pow Khim and for their assistance in the experiments. They taught me many lessons around the laboratories and workshops. I have been very lucky to work side by side with the distinguished students in Thermal and Fluids Laboratory who have helped me a lot. This report also significantly benefited from the discussions with my friends, Dr. Zhao Cunlu, Dr. Che Zhizhao, Dr. Li Haiwang, Dr. Liang Qian, Dr. Zhou Yi, Dr. Suhanya Duraiswamy, Mr. Zhao Yugang, Mr. Shang Xiaopeng, Dr. Phan Dinh Tuan and Mr. Dhiman Das.

Finally, I would not be able to complete this thesis without the support of my family. My parents, sister and wife encouraged me constantly, and the sacrifices they have made for me are priceless. I will be forever grateful.

Abstract

Transport and interactions of colloidal particles and biomolecules in microchannels are of great importance to many microfluidic applications, such as drug delivery in life science, microscale heat exchangers in electronic cooling, food processing industry etc. The phenomenon that particles suspended in liquid are captured by a solid surface (e.g. microchannel wall) is referred to as *particle deposition*. Particle deposition plays a crucial role in numerous practical applications, and is also of fundamental interest to the field of colloid science. This thesis presents studies of the thermal effects on particle deposition in microchannels, which has been a frequently “ignored” but is an important factor for thermal driven particle deposition processes at elevated temperatures. In the present study, both experimental investigation and theoretical modelling are carried out to characterise the thermal effects, including the effects of bulk solution temperature and temperature gradient in a microfluidic system. To the best knowledge of the author, this is the first attempt to investigate the thermal effect on particle deposition in microchannels.

The effects of bulk solution temperature on particle deposition are investigated in a thermostatic microfluidic chip, consisting of one deposition microchannel and two minichannels used for heating from both sides of the deposition channel. This microfluidic chip provides a well-controlled bulk temperature with a good uniformity for the particle suspension (diameter: 930 nm), and allows a direct visualisation of the dynamic process of particle deposition at elevated temperatures with aid of a microscope. Experimental measurements were conducted to obtain the number of deposited particles onto the microchannel surface at various bulk solution temperatures. The experimental results show that the particle deposition rate, which is characterised by the Sherwood number, is increased by 265% with increase of the bulk solution temperature from room temperature (297.25 K) to 339.25 K. A theoretical model was derived based on the Derjaguin-Landau-Verwey-Overbeek (DLVO) theory. This model simplifies the three-dimensional particle transport phenomenon in a microchannel to a one-dimensional mass

transport problem, taking into account of temperature dependence of physicochemical parameters involved in the particle deposition process. The numerically solved particle deposition rates from the one-dimensional mass transfer model agree reasonably with the experimental measurements. The model provides the interaction potential curves to describe the interactions between a microparticle and the microchannel at different temperatures. These curves show that the enhanced particle deposition observed in experiments is caused by the increased attractive interactions (van der Waals force and gravity) and the reduced repulsive interactions (electric double layer force) when increasing the bulk solution temperature. Therefore, it leads to reduced energy barriers for particle deposition at elevated temperatures. Besides, the effect of electrolyte concentration was further investigated for the particle deposition processes at elevated temperatures.

The effects of temperature gradient on particle deposition were studied in a microfluidic device. The device consists of a PDMS microchannel for easy observation, an Indium tin oxide (ITO) coated glass for heating and a thermoelectric (TEC) unit for cooling to form a stable and adjustable temperature gradient across the channel. This design enables the dynamic particle deposition processes to be directly observed along the direction of the applied temperature gradient, thereby providing an effective microfluidic platform for investigating the particle-surface interaction phenomena under non-equilibrium thermal environment. Both experimental and numerical studies were carried out to examine the particle deposition under different temperature gradients. The experimental results show that the particle deposition rate (Sherwood number) is reduced by 56% when the temperature gradient inside the microchannel was increased by three orders from 78.9 K/m to 6846.9 K/m. The numerical results of particle deposition rate agree reasonably with the experimental measurements. The interaction potential curves from the numerical model suggest that the particles could experience larger resistance arising from the increased thermophoretic force in the presence of the temperature gradient, at large particle-wall distance fewer particles are transported from the bulk solution to the near-wall region. In addition,

the particles need to overcome a higher energy barrier caused by the reduced bulk solution temperature in the vicinity of the channel surface, leading to the reduced particle deposition rate under a temperature gradient. Besides, for a given thermal condition, the particle deposition was observed to be further enhanced when the electrolyte concentration of the particle suspension is increased.

The effects of hydrodynamic flow on the particle deposition at elevated temperatures were investigated by applying a steady flow and a pulsatile flow in the microchannel. For the steady flow, the Sherwood number is reduced with increasing the Reynolds number of the hydrodynamic flow. The reduction of particle deposition rate with Reynolds number is attributed to the increased hydrodynamic lift force which hinders the transport of particles from the bulk solution to the near-wall region. For the pulsatile flow which is generated by a specially designed pulsation generation unit, an oscillatory flow component is superimposed onto the steady flow of the particle suspension. Experiments were conducted to investigate the effect of the pulsatile flow on the particle deposition rate at different flow oscillation frequencies. The results show that the particle deposition rate can be reduced by 50% with increasing the flow oscillation frequency from 0 Hz to 1 Hz at elevated temperatures with the steady flow component being fixed at 1 mL/h.

CONTENT

ABSTRACT	1
CHAPTER 1 INTRODUCTION.....	17
1.1 BACKGROUND AND MOTIVATION	17
1.2 OBJECTIVE AND SCOPE	19
1.3 OUTLINE OF REPORT.....	20
CHAPTER 2 LITERATURE REVIEW.....	21
2.1 TYPES OF FOULING	21
2.2 PARTICLE DEPOSITION.....	23
2.3 THEORY OF SURFACE FORCES.....	24
2.3.1 <i>Derjaguin-Landau-Verwey-Overbeek (DLVO) theory</i>	25
2.2.1.1 van der Waals force.....	25
2.2.1.2 Electrostatic double-Layer force	28
2.3.2 <i>Non-DLVO forces</i>	33
2.4 TEMPERATURE CONTROL IN MICROFLUIDIC SYSTEMS	35
2.4.1 <i>Bulk temperature</i>	35
2.4.2 <i>Temperature gradient</i>	39
2.5 PARTICLE DEPOSITION IN MICROCHANNELS	43
2.5.1 <i>Experimental studies</i>	43
2.5.1.1 Effect of pH on particle deposition	43
2.5.1.2 Effect of ion concentration on particle deposition.....	43
2.5.1.3 Effect of properties of particle and wall on particle deposition	44
2.5.1.4 Effect of external field on particle deposition	45
2.5.2 <i>Theoretical modelling/studies</i>	46
2.6 FOULING MITIGATION TECHNIQUES.....	49
2.6.1 <i>Solution</i>	49
2.6.2 <i>Heat transfer surface</i>	50
2.6.3 <i>External field</i>	51

2.7 SUMMARY	52
CHAPTER 3 MODELLING FOR PARTICLE DEPOSITION IN MICROCHANNELS AT ELEVATED TEMPERATURES	53
3.1 MASS TRANSPORT EQUATION	54
3.2 BOUNDARY CONDITIONS	58
3.3 DETERMINATION OF PARTICLE DEPOSITION RATE.....	59
3.4 COLLOIDAL AND EXTERNAL FORCES	60
<i>3.4.1 Colloidal forces.....</i>	<i>60</i>
3.4.1.1 Electric double layer (EDL) force	61
3.4.1.2 van der Waals force.....	67
<i>3.4.2 External forces.....</i>	<i>70</i>
3.4.2.1 Gravity force	70
3.4.2.2 Hydrodynamic lift force	71
3.4.2.3 Thermophoretic force.....	73
3.5 SUMMARY	74
CHAPTER 4 EFFECT OF BULK TEMPERATURE ON PARTICLE DEPOSITION IN MICROCHANNELS.....	75
4.1 EXPERIMENT	75
<i>4.1.1 Experimental setup.....</i>	<i>76</i>
4.1.1.1 Materials	77
4.1.1.2 Microchip.....	77
4.1.1.3 Characterisation of thermal field in microchannel	78
<i>4.1.2 Experimental procedures</i>	<i>81</i>
<i>4.1.3 Uncertainty analysis in measurements.....</i>	<i>84</i>
4.2 THEORETICAL MODELLING	85
4.3 RESULTS AND DISCUSSION	87
<i>4.3.1 Effect of solution temperature.....</i>	<i>87</i>
<i>4.3.2 Effect of electrolyte concentration at elevated temperatures.....</i>	<i>94</i>
4.4 SUMMARY	99

CHAPTER 5 EFFECT OF TEMPERATURE GRADIENT ON PARTICLE DEPOSITION IN MICROCHANNELS.....100

5.1 EXPERIMENT	100
5.1.1 <i>Experimental setup</i>	100
5.1.1.1 Materials	101
5.1.1.2 Temperature-gradient microchip	102
5.1.1.3 Characterisation of thermal field in microchannel	105
5.1.2 <i>Experimental procedures</i>	108
5.1.3 <i>Uncertainty analysis in measurements</i>	111
5.2 THEORETICAL MODELLING.....	111
5.3 RESULTS AND DISCUSSION	113
5.3.1 <i>Effect of temperature gradient on particle deposition</i>	114
5.3.2 <i>Effect of electrolyte concentration on particle deposition under temperature gradients</i>	119
5.4 SUMMARY	125

CHAPTER 6 EFFECT OF HYDRODYNAMIC FLOW ON PARTICLE DEPOSITION IN MICROCHANNELS AT ELEVATED TEMPERATURES126

6.1 INTRODUCTION	126
6.2 EXPERIMENT	128
6.2.1 <i>Experimental setup</i>	128
6.2.1.1 Materials	129
6.2.1.2 Pulsation generation unit.....	129
6.2.1.3 Characterisation of the oscillatory flow generated by the pulsation generation unit	130
6.2.2 <i>Experimental procedures</i>	134
6.2.3 <i>Uncertainty analysis in measurements</i>	135
6.3 THEORETICAL MODELLING.....	136
6.4 RESULTS AND DISCUSSION	138
6.4.1 <i>Effect of flow rate of particle solution (Steady flow)</i>	138
6.4.2 <i>Effect of flow oscillation frequency (pulsatile flow)</i>	146
6.5 SUMMARY	148

CHAPTER 7 CONCLUSIONS AND RECOMMENDATIONS	150
7.1 CONCLUSIONS	150
7.2 RECOMMENDATIONS	153
REFERENCES	154
APPENDIX A PARAMETERS FOR TEMPERATURE DEPENDENCE OF WATER PROPERTIES.....	164
APPENDIX B PROTOCOL FOR ITO GLASS ETCHING.....	166
PUBLICATIONS ARISING FROM THIS THESIS	169

List of Figures

Figure 2.1 Interaction between sphere and plate.....	28
Figure 2.2 Schematic of a diffuse double layer of (a) a charged particle, (b) a charged particle in the vicinity of a charged solid/wall surface.	29
Figure 2.3 Example diagram of potential energy vs separation distance (Perry and Kandlikar 2008)	33
Figure 2.4 (a) A schematic of the temperature control device by an external Peltier element; the yeast channel is placed below the temperature control channel (Velve Casquillas et al. 2011). (b) Schematic of the dual Peltier assembly for rapid thermal cycling followed by electrophoretic analysis on-chip (Khandurina et al. 2000).	36
Figure 2.5 (a) Peltier thermocycler for the PCR micro reactor; (b) a photograph of the serpentine polycarbonate microchannel (Yang et al. 2002).	36
Figure 2.6 (a) Top view of the ultrafast polymerase chain reaction device. Visible is the heatsink-Peltier-phenolic-Peltier-heatsink sandwich that contained the gallium eutectic used for thermal transfer to the sample tube placed where the dummy sample sensor is visible in this photo. (b) Cross section of the heatsink-Peltier-phenolic-Peltier-heatsink sandwich where the sample tube and 2.3 ml gallium eutectic reservoir are visible (Maltezos et al. 2010).	37
Figure 2.7 Top view of the microchip showing the patterned heaters and temperature sensors (Lao et al. 2000).	37
Figure 2.8 Schematic of microfluidic device incorporating co-running heating channels. The working (sample) channel is shown in black and the co-running heating channel in grey (de Mello et al. 2004).	38
Figure 2.9 (a) Processing flow of conductive microwire inside PDMS using molding injection. (b) Optical images of the microheater and thermal sensor. The upper view is the longitudinal view and the lower, the cross-sectional view (Wu et al. 2009).	38
Figure 2.10 (A) Two reactant channels (RC) merging into a temperature control channel (TCC). (B) Layout of the device used for demonstration experiments (Guijt et al. 2003).	39
Figure 2.11 (a) Schematic diagram of a device with an on-chip linear temperature gradient. (b) A plot of temperature vs position of the temperature gradient device (Mao et al. 2002).	40
Figure 2.12 A schematic of the device: (a) the empty channel, (b) a channel is filled with a conductive epoxy, (c) the channel is heated until the epoxy solidifies after inserting wires for the electrical connection (Vigolo et al. 2010).	41
Figure 2.13 Schematic drawing of temperature gradient focusing apparatus (Matsui et al. 2007).	42
Figure 2.14 (a) Top and side view of the device with four gold heaters placed along a square (Jiao et al. 2007). (b) Schematic of the microchannel system with platinum microheater (Yap et al. 2009).	42
Figure 2.15 (a) cross section view of the deposition chamber, (b) flow cell on substrate without clamping (Mustin and Stoeber 2016).	45

Figure 2.16 Schematics of parallel-plate and cylindrical channels (Adamczyk and Van De Ven 1981)	47
Figure 2.17 Schematic of the parallel-plate channel and force analysis (Unni and Yang 2009) ...	48
Figure 2.18 Schematic of the patchy heterogeneous cylindrical microchannels (Chatterjee et al. 2012)	48
Figure 3.1 Flow chart of the modelling for the particle deposition in microchannels at elevated temperatures.....	54
Figure 3.2 Schematic of microparticle transport in a microchannel. The forces on the particle are van der Waals force (F_{vdw}), gravity force (F_G), electric double layer force (F_{edl}), thermophoretic force (F_T), and hydrodynamic lift force (F_L). The radius of the particle is a_p , the minimum separation distance between the particle surface and the bottom surface of the microchannel is h , the flow velocity distribution is $U(y)$, and applied temperature gradient in the microchannel is ∇T . (The figure is not drawn to scale)	55
Figure 3.3 zeta potentials of particle and channel surfaces in DI water vs. temperature. Solid square (-■-) indicates the zeta potential of polystyrene particle, and solid triangle (-▲-) indicates the zeta potential of the microchannel surface. Data are calculated for the particles and the microchannel contacting with DI water according to Eq. (3.31).	63
Figure 3.4 zeta potentials of particle and channel surfaces vs. electrolyte concentration. Solid square (-■-) indicates the zeta potential of polystyrene particle, and solid triangle (-▲-) indicates the zeta potential of the microchannel surface (PMMA and PDMS). Data are calculated for the particles and the microchannel contacting with DI water according to Eq. (3.32) while the solution temperature is fixed at 50 °C.....	64
Figure 3.5 Dielectric constant of water versus temperature. Data are calculated for DI water according to Eqs. (3.35-3.36).....	65
Figure 3.6 Debye length (κ^{-1}) defined Eq. (3.30) in water versus the solution temperature. The solid square (-■-) denotes the Debye length (the thickness of electric double layer). Data are calculated for DI water with consideration of the temperature dependence of the ion concentration, n_∞ shown in Eqs. (3.33-3.34), and the dielectric constant of water, ϵ shown in in Eqs. (3.35-3.36). The change of Debye length arises from the variation of bulk ion concentration in addition to dielectric constant of DI water.	66
Figure 3.7 Refractive index of water n_3 (-■-) versus the solution temperature. Data are calculated for DI water according to Eqs. (3.40-3.43) with varying temperature from 10 °C to 90 °C.....	69
Figure 3.8 Hamaker constant (A_{132} defined in Eq. (3.39)) versus temperature. Data are calculated for the Hamaker constant of the polystyrene particle interacting with PMMA/PDMS surface via DI water. The solution temperature varies from 10 °C to 90 °C. The temperature dependence of Hamaker constant arises from the variation of the static dielectric constant and refractive index of water.....	70
Figure 4.1 Schematic of the microfluidic system for the direct observation of the particle deposition kinetics in microchannels. Inset: Cross-section view of the microchip. Three thermocouples are used to measure the solution temperature in the deposition channel (unit: mm). (Figure is not drawn to scale).....	76
Figure 4.2 Schematic of the microchannels (a) Isometric view, (b) Cross-section view, (c) Image of the microchip used in the experiments. The microchannels are formed by thermally bonding	

one PMMA plate with designed patterns and one plain PMMA plate together. Inset shows the dimensions of microchannels. Three thermocouples (TC1, TC2, TC3) are used to measure the solution temperature in the deposition channel (unit: mm) (Figure is not drawn to scale)..... 78

Figure 4.3 The relationship between the measured temperature by the thermocouples and the standard temperature of the calibrator. Linear fitting curve of the data points provides a calibrated function for converting the temperatures measured by thermocouple to the real temperatures. ... 79

Figure 4.4 Temperature profile along the xperiment of the deposition channel. Data are obtained by a two-dimensional simulation with boundary conditions. Inset: wall temperatures of heating channels of 339.25 K and heat convection between the chip and the ambient air of $h = 10 \text{ W/m}^2 \text{ K}$ 81

Figure 4.5 Videomicroscopic images of $0.93 \text{ }\mu\text{m}$ polystyrene particles captured using 15X objective lens under the heating condition of 339.25 K solution temperature at 0min, 30min, 60min and 90min. Particles are shown as black dots..... 83

Figure 4.6 Number of deposited particles per unit area versus deposition time for five different solution temperatures at 297.25 K, 317.35 K, 324.85 K, 331.85 K and 339.25 K. Data are for fluorescent polystyrene particles dispersed in DI water (stationary fluid). The solution temperature is determined by an average reading of three thermocouples. Hot water is supplied through the heating channels at 15 min after starting each experiment. 88

Figure 4.7 Dimensionless static deposition rate (Sherwood number) as a function of the temperature of solution at five different temperatures, 297.25 K, 317.35 K, 324.85 K, 331.85 K and 339.25 K. Solid squares (■) indicate the measured Sherwood number Sh_{exp} shown in Eq. (4.2) from experiments, and empty squares (□) show the calculated Sherwood number Sh_{num} by Eq. (4.6) from modelling. The dotted line shows the least-square fitting line. Data are for fluorescent polystyrene particles dispersed in DI water (stationary fluid). 89

Figure 4.8 (a) Dimensionless particle-microchannel interaction potential \bar{V} versus the dimensionless separation distance H for different bulk solution temperatures. (b) The energy barrier as a function of the solution temperature in a stationary fluid. Data are calculated based on Eq. (3.18) for fluorescent polystyrene particles dispersed in stationary DI water. The dotted square PEM indicates the primary energy minimum (PEM) region..... 91

Figure 4.9 (a) Computational dimensionless particle concentration \bar{n} versus the dimensionless separation distance H for different bulk solution temperatures. (b) The dimensionless particle concentration in the vicinity of the microchannel surface ($H = 0 \sim 0.8$). The depletion zone is shrunk with increasing temperature. Data are calculated based on Eq. (3.20) for fluorescent polystyrene particles dispersed in stationary DI water. 93

Figure 4.10 Number of deposited particles per unit area versus deposition time at different electrolyte concentrations with fixed solution temperature (324.85 K). Data are for fluorescent polystyrene particles dispersed in DI water and NaCl solutions (Stationary fluid). Hot water is supplied through the heating channels at 15 min after starting each experiment. 94

Figure 4.11 Dimensionless static deposition rate (Sherwood number) versus the electrolyte concentration for DI water, $5 \times 10^{-5} \text{ M}$, $5 \times 10^{-4} \text{ M}$ and $5 \times 10^{-3} \text{ M}$. Solid squares (■) indicate the measured Sherwood number Sh_{exp} shown in Eq. (4.2) from experiments, and empty squares (□) show the calculated Sherwood number Sh_{num} shown in Eq. (4.6) from modelling. The dotted line shows the least-square fitting line. Inset shows the thickness of electric double layer (Debye length) as a function of the electrolyte concentration. Data are for fluorescent polystyrene particles dispersed in DI water and NaCl solutions (stationary fluid). The solution temperature is kept at 324.85 K..... 95

Figure 4.12 (a) Dimensionless particle-microchannel interaction potential \bar{V} versus the dimensionless separation distance H for DI water and *NaCl* solutions (5×10^{-5} M, 5×10^{-4} M and 5×10^{-3} M). (b) The energy barrier as a function of the electrolyte concentration in a stationary fluid. Data are calculated based on Eq. (3.18) for fluorescent polystyrene particles dispersed in DI water and *NaCl* solution (stationary fluid). The solution temperature is kept at 324.85 K. The dotted square SEM indicates the secondary energy minimum region, and the dotted square PEM indicates the primary energy minimum region. 98

Figure 5.1 Schematic of the microfluidic system used for the direct observation of the particle deposition kinetics along the direction of applied temperature gradient. Two thermocouples (TC 1, TC 2) are used to measure the temperatures on the top surface of the PDMS block and bottom surface of the ITO coated glass slide (Figure is not drawn to scale)..... 101

Figure 5.2 Schematic of the temperature-gradient microchip, consisting of the PDMS microchannel, the glass slide coated with ITO film and the TEC unit. Various temperature gradients can be achieved by cooling the top surface of the microchip with the TEC unit and heating the bottom surface with the ITO film heater. (a) Isometric view, (b) Cross section view, (c) A picture of the integrated temperature-gradient microchip and top view of the PDMS microchannel bonded with the ITO coated glass slide. (Figure is for not drawn to scale) 104

Figure 5.3 (a) Temperatures (T_{ITO} , T_{TEC}) and temperature differences (ΔT) measured by two thermocouples at various power inputs to TEC cooling unit (P_{TEC}) and ITO film heater (P_{ITO}). (b) Schematic of the temperature measurement in the experiment. The empty triangles indicate the temperature (T_{ITO}) measured on the bottom surface of the ITO film heater in Figure 5.2. The empty circles indicate the temperature (T_{TEC}) measured on the top surface of the PDMS block in Figure 5.2. The empty squares indicate the temperature difference ($\Delta T = T_{ITO} - T_{TEC}$) between the top surface of the PDMS block and the bottom surface of the ITO film heater. 106

Figure 5.4 (a) The numerical model consisting of the microchannel and the PDMS block and the glass slide. (b) Temperature gradient ($-\square-$) along the centreline (CD shown in Section A-A) of the microchannel and bulk temperature ($-\blacksquare-$) in the observation region versus the power inputs to the TEC cooling unit (P_{TEC}) and ITO film heater (P_{ITO}). The bulk temperature is estimated as the average temperature along the centreline, $(T_C + T_D)/2$. Data are obtained by a three-dimensional simulation with boundary conditions: The surface temperature covered by TEC unit is set as constant ($T = T_{TEC}$), Constant surface heat source is applied onto the ITO film heater ($Q = P_{ITO}$), and convective heat transfer ($h = 30 \text{ W/m}^2 \text{ K}$ for bottom surface and $5 \text{ W/m}^2 \text{ K}$ for side and top surfaces of the PDMS block) is set between the chip and the ambient air to account for heat loss, a hydrodynamic flow with constant flow rate (0.1 mL/h) and inlet temperature (25°C) is applied inside the microchannel..... 108

Figure 5.5 Videomicroscopic images of $0.93 \mu\text{m}$ polystyrene particles captured using 10X objective lens under temperature gradient maintained at 6846.9 K/m (0.1 mL/h , *NaCl*: 5×10^{-4} M) at 0min, 20min, 40min and 60min. Particles are shown as black dots..... 110

Figure 5.6 Number of deposited particles per unit area versus deposition time for four different temperature gradients at 78.9 K/m , 2136.5 K/m , 5516.1 K/m and 6846.9 K/m . Data are for fluorescent polystyrene particles dispersed in a *NaCl* solution (5×10^{-4} M). The sample flow rate is fixed at 0.1 mL/h . Sample solution is supplied to the microchannel after a stable temperature gradient is formed inside the microchannel. 114

Figure 5.7 Dimensionless static deposition rate (Sherwood number) as a function of the temperature gradients at 78.9 K/m , 2136.5 K/m , 3385.7 K/m , 5516.1 K/m and 6846.9 K/m . Solid squares (\blacksquare) indicate the measured Sherwood number Sh_{exp} shown in Eq. (5.1) from experiments,

and empty squares (\square) show the calculated Sherwood number Sh_{num} by Eq. (5.4) from modelling. The dotted line shows the least-square fitting line. Data are for fluorescent polystyrene particles dispersed in a *NaCl* solution (5×10^{-4} M) with fixed flow rate 0.1 mL/h. 115

Figure 5.8 (a) Dimensionless particle-microchannel interaction potential \bar{V} versus the dimensionless separation distance H for different temperature gradients. (b) The energy barrier (shown by $-\blacksquare-$) and the interaction potential at $H = 10$ (shown by $-\square-$) as a function of the temperature gradient. Data are calculated based on Eq. (3.18) for fluorescent polystyrene particles dispersed in a *NaCl* solution (5×10^{-4} M) with a fixed sample flow rate 0.1 mL/h. The dotted square SEM indicates the secondary energy minimum region, and the dotted square PEM indicates the primary energy minimum region. 118

Figure 5.9 Number of deposited particles per unit area versus deposition time at different electrolyte concentrations with fixed temperature gradient at 6846.9 K/m and constant sample flow rate at 0.1 mL/h. Data are for fluorescent polystyrene particles dispersed in DI water and *NaCl* solutions (5×10^{-4} M, 5×10^{-2} M). Sample solution is supplied to the microchannel after a stable temperature gradient is formed inside the microchannel. 120

Figure 5.10 Dimensionless static deposition rate (Sherwood number) versus the electrolyte concentration for DI water, 5×10^{-4} M and 5×10^{-3} M. Solid symbols indicate the measured Sherwood number Sh_{exp} shown in Eq. (5.1) from experiments, and empty symbols show the calculated Sherwood number Sh_{num} by Eq. (5.4) from modelling. Squares show the results for the temperature gradient of 78.9 K/m. Triangles show the results for the temperature gradient of 3385.7 K/m. Circles show the results for the temperature gradient of 6846.9 K/m. Data are for fluorescent polystyrene particles dispersed in DI water and *NaCl* solutions. The sample flow rate is fixed at 0.1 mL/h. 121

Figure 5.11 (a) Dimensionless particle-microchannel interaction potential \bar{V} versus the dimensionless separation distance H for three electrolyte concentrations: DI water, 5×10^{-4} M and 5×10^{-2} M under different temperature gradients (1: 78.9 K/m, 2: 3385.7 K/m, 3: 6846.9 K/m), Inset shows the enlarged view for the electrolyte concentrations at 5×10^{-4} M and 5×10^{-2} M. (b) The energy barrier as a function of the electrolyte concentration for three different temperature gradients. Data are calculated based on Eq. (3.18) for fluorescent polystyrene particles dispersed in DI water and *NaCl* solution (Sample flow rate: 0.1 mL/h). The dotted square SEM indicates the secondary energy minimum region, and the dotted square PEM indicates the primary energy minimum region. 124

Figure 6.1 Characteristics of steady flow and pulsatile flow. (a) and (b) Schematics of axial velocity profiles across channels, (c) and (d) Schematics of flow rate versus time for steady flow and pulsatile flow, respectively. Area filled by colour indicates the volume of fluid moved during a certain period of time. The volume of fluid moved by pulsatile flow can be decomposed to a steady component from steady flow and an oscillating component from oscillatory flow (Figures are not drawn to scale). 127

Figure 6.2 The layout of the microfluidic system. (a) Schematic of the microfluidic system with pulsatile flow for the direct observation of the particle deposition kinetics in microchannels. Inset: Cross-section view of pulsation generation unit. A pulsation generation unit (PGU) connecting to a function generator is implemented to generate a controllable flow pulsation into the hydrodynamic flow in the microchannel. (b) Photo of the microchip used in the experiments (Figure is not drawn to scale). 128

Figure 6.3 Schematic of pulsation generation unit, (a) isometric view, (b) cross-section view, (c) and (d) Images of the fabricated pulsation generation unit. The piezoelectric (PZT) disk is connected to a function generator to generate a controllable pulsation in the sample flow. The

frequency and amplitude of the PZT disk is well controlled by regulating the sinusoidal signal from the function generator.....	130
Figure 6.4 (a) Schematic of the experimental setup for characterisation of the oscillatory flow generated by the pulsation generation unit, (b) Photo of the flow rate measurement of the oscillatory flow.	131
Figure 6.5 Displacement of the centre point of the water/air interface versus time. Solid squares (■) denote the measured data, and dot line indicates the sine curve fit. Data were obtained with the sinusoidal signal of peak-to-peak voltage, 0.5 V, and frequency, 0.6 Hz.	132
Figure 6.6 Amplitude of the volume flow rate of the oscillatory flow (Q_{amp}) versus the oscillation frequency (f). Experiments were conducted with constant voltage of the sinusoidal signal to the PZT disk ($V_{pp} = 0.5$ V). Dot line represents the average value of the amplitude of oscillatory flow rate.....	133
Figure 6.7 Number of deposited particles per unit area versus time for different sample flow rates inside the microchannel (0.01 mL/h, 0.025 mL/h, 0.1 mL/h, 0.5 mL/h, 2 mL/h) Data are for fluorescent polystyrene particles dispersed in <i>NaCl</i> solution (5×10^{-4} M). The solution temperature is kept at 324.85 K.	139
Figure 6.8 Dimensionless static deposition rate (Sherwood number) versus the Reynolds number of the sample flow. Solid squares (■) indicate the measured Sherwood number Sh_{exp} shown in Eq. (6.7) from experiments, and empty squares (□) show the calculated Sherwood number Sh_{num} by Eq. (6.11) from modelling. The dotted line shows the least-square fitting line. Inset shows the Reynolds numbers of the sample fluid as a function of the sample flow rates. Data are for fluorescent polystyrene particles dispersed in stationary <i>NaCl</i> solution (5×10^{-4} M). The solution temperature is kept at 324.85 K.	140
Figure 6.9 (a) Dimensionless particle-microchannel interaction potential \bar{V} versus the dimensionless separation distance H for different Reynolds number of the sample flow. (b) The energy barrier (shown by - □-) and the interaction potential at $H = 10$ (shown by -■-) as a function of the Reynolds number of the sample flow. Data are calculated based on Eq. (3.18) for fluorescent polystyrene particles dispersed in a <i>NaCl</i> solution (5×10^{-4} M). The solution temperature is kept at 324.85 K. The dotted square SEM indicates the secondary energy minimum region, and the dotted square PEM indicates the primary energy minimum region.	143
Figure 6.10 Number of deposited particles in area of interest versus time for different solution temperature in a hydrodynamic flow. Data are for fluorescent polystyrene particles dispersed in <i>NaCl</i> solution (5×10^{-4} M) while the sample flow rate is fixed at 0.1 mL/h ($Re = 0.091$).	144
Figure 6.11 Dimensionless static deposition rate (Sherwood number) as a function of the temperature of solution at three different temperatures, 297.25 K, 324.85 K and 339.25 K. Solid squares (■) indicate the measured Sherwood number Sh_{exp} shown in Eq. (6.7) from experiments, and empty squares (□) show the calculated Sherwood number Sh_{num} shown in Eq. (6.11) from modelling. The dotted line shows the least-square fitting line. Data are for fluorescent polystyrene particles dispersed in a <i>NaCl</i> solution (5×10^{-4} M) while the sample flow rate is fixed at 0.1 mL/h ($Re=0.091$).	145
Figure 6.12 The normalised particle deposition rate sh/sh_0 in Eq. (6.8) versus the flow oscillation frequency for the microfluidic flow. Data are for the PMMA microchannel and the polystyrene microparticles (Diameter: 930 nm) suspended in a <i>NaCl</i> solution (5×10^{-4} M). The flow rate of the steady flow is maintained at 1 mL/h, and the solution temperature is kept at 51.6 °C. The amplitude of the PZT disk is fixed at 0.5 V and the average amplitude of the flow oscillation (Q_{amp}) is 0.09 mL/h. The dotted line represents the least-squares fitting curve.	147

List of Tables

Table 3.1 Property table of materials (Pressure: 0.101325 Mpa, Temperature: 25 °C)	68
Table 3.2 Property table of water at various temperatures (Pressure: 0.101325 Mpa)	71
Table 4.1 Temperatures measured in microchannel with constant flow rate of hot water (6 ml/min)	80
Table 4.2 Values of the parameters used for modelling at different temperatures	86
Table 5.1 Values of the parameters used for modelling at different temperatures	113
Table A.1 Parameter table for the calculation of the static dielectric constant, ϵ , in Eq. 3.35.....	164
Table A.2 Coefficient for calculation of Harris-Alderg-factor, g in Eq. 3.36.....	164
Table A.3 Coefficient for calculation of the refractive index, n , in Eq. 3.40.....	165

List of Symbols

a_p	Particle radius (m)
a_1	Radius of interacting particle 1 (m)
a_2	Radius of interacting particle 2 (m)
A_{132}	Hamaker constant for interaction between substances 1 and 2 in medium 3 (J)
B	Width of the microchannel (m)
w	Half channel height (m)
D_x	Diffusivity in X direction (m^2/s)
D_y	Diffusivity in Y direction (m^2/s)
D_T	Thermal diffusion coefficient (m^2/s)
D_∞	Stokes-Einstein diffusivity (m^2/s)
DI	Double layer number in the HHF expression for EDL interaction
Da	Double layer asymmetry number in the HHF expression for EDL interaction
$f_1(H)$	UHCC correction function for diffusivity perpendicular to the solid surface
$f_3(H)$	UHCC correction function for diffusivity parallel to the solid surface
$f_4(H)$	UHCC correction function for diffusivity along the flow direction (X)
F_x	X component of the total force exerted on the particle (N)
F_y	Y component of the total force exerted on the particle (N)
\bar{F}_{edl}	Dimensionless EDL interaction force
\bar{F}_{vdw}	Dimensionless van der Waals interaction force
\bar{F}_G	Dimensionless gravity force
\bar{F}_L	Dimensionless hydrodynamic lift force
\bar{F}_T	Dimensionless thermophoretic force
h	Minimum separation distance between particle and wall (m)
H	Dimensionless particle-wall separation
H_0	Dimensionless primary energy minimum separation
H_∞	Dimensionless particle-wall separation in bulk fluid
j_x	Particle flux in X direction ($\text{m}^{-2}\cdot\text{s}^{-1}$)
j_y	Particle flux in Y direction ($\text{m}^{-2}\cdot\text{s}^{-1}$)
\bar{J}_x	Dimensionless mass flux in X direction
\bar{J}_y	Dimensionless mass flux in Y direction
k_B	Boltzmann's constant ($1.38064852 \times 10^{-23}$ J/K)
L	Length of the microchannel (m)

n	Particle number concentration (/m ³)
\bar{n}	Dimensionless particle number concentration
$n_{\infty,p}$	Particle number concentration in bulk liquid (/m ³)
Pe	Peclet number based on average flow velocity
Q	Volume flow rate of liquid (m ³ /s)
Re	Reynolds number based on average flow velocity
Sh	Sherwood number
t	Time (s)
T	Absolute temperature (K)
T_0	Reference temperature (293.15 K)
U_{avg}	Average flow velocity in microchannels (m/s)
\bar{V}	Dimensionless total interaction potential
\bar{V}_{edl}	Dimensionless EDL interaction potential
\bar{V}_{vdw}	Dimensionless van der Waals interaction potential
\bar{V}_G	Dimensionless gravity potential
\bar{V}_L	Dimensionless lift potential
\bar{V}_T	Dimensionless thermophoretic potential
z	Ionic valence
e	Elementary electric charge ($1.602176620898 \times 10^{-19}$ C)

Greek symbols

ε	Dielectric constant
ε_0	Absolute dielectric constant of vacuum (8.845×10^{-12} C ² /N·m ²)
ζ	Zeta potential (V)
λ	London retardation wavelength (100 nm)
κ	Debye-Huckel parameter (/m)
μ	Dynamic viscosity of liquid (N·s/m ²)
ν	Kinematic viscosity of liquid (m ² /s)
ρ	Density (kg/m ³)
ψ	Electric potential (V)
τ	Ratio of particle radius (a_p) to the Debye length (κ^{-1})
ω	Mobility of particle

Chapter 1

Introduction

In this chapter, the background and motivation of this study are briefly introduced. The research objective and scope are also stated to give an overall view of this research. Finally, the outline of this thesis is presented.

1.1 BACKGROUND AND MOTIVATION

Deposition of colloid particles is a common and crucial phenomenon in numerous natural and practical processes, such as water filtration (Wang and Keller 2009), drug delivery (Sabirianov et al. 2011), and heat exchangers for dairy or semiconductors applications (Perry and Kandlikar 2008, Tuckerman et al. 2011). Due to accumulation of the deposited particles on solid surfaces, particulate fouling would occur and become a major challenge in these processes. Serious particulate fouling would reduce the effectiveness and increase the energy consumptions, even damage the relevant equipment and thus affect whole process. In addition to the practical aspects, fundamental understanding the deposition mechanism of colloidal particles is of great interest to colloidal science. Useful information can be extracted from the kinetics of various particle deposition processes for developing the colloidal deposition theories. Because of its importance, particle deposition has been extensively investigated both experimentally and theoretically. A significant number of researches has been conducted on various parameters, such as particle size, pH of solution, surface properties etc. (Elimelech et al. 1995, Song and Elimelech 1995, Yang et al. 1998, Unni and Yang 2009). However, previous research works on the deposition of micro/nano particles are mainly concentrated on studies under room temperature condition. Studies of thermal effect on particle deposition are rare, including the influences of bulk temperature and temperature gradient. Thermal effects are particularly important to

thermally driven particle deposition processes because the temperature-dependent thermophysical and electric properties would be very different from those at room temperature.

On the other hand, microfluidic systems have received considerable attention due to their high throughput, low energy consumption, compact size and most importantly controllable and well-defined physical and chemical conditions in the past two decades. Microfluidic systems have been intensively studied for thermal management of high-power microelectronic devices (Park and Thome 2010, Marcinichen et al. 2013). It was reported that microchannel cooling can successfully dissipate waste heat with a heat flux up to 1000 W/cm^2 (Incropera and Dewitt 2002). To further improve its heat performance for the rapid development of microelectronic chips in the future, nanofluids are proposed to be a promising option. Superior thermal performance can be further improved by suspending nanoparticles in microfluidic flows, because the nanoparticles can improve the thermal conductivity of heat transfer fluids (Lee et al. 1999). However, the abrasive nanoparticles may induce erosion and clogging in fine microchannels under elevated temperatures. This would result in prohibitively large pressure drop across channels and deteriorate overall performance of the device. Recently, microchannel systems have also been employed for the high-temperature short-time (HTST) milk pasteurization in dairy industry (Tuckerman et al. 2011). The microscale ultrahigh temperature pasteurizer has successfully demonstrated an advantageous high efficiency of the energy consumption compared with the conventional bulky milk pasteurizer. However, the milk fouling in microchannel became a big challenge for reliable and long-term performance of the pasteurization process. This further emphasizes the needs for investigating the particle deposition in a microfluidic device at elevated temperatures.

Therefore, it would be meaningful and imperative to conduct fundamental researches on the kinetics of the particle deposition at elevated temperatures while microfluidic devices can provide effective platforms for well-defined model systems.

1.2 OBJECTIVE AND SCOPE

Motivated by the fundamental and practical demands of the particle deposition in microchannels, this study is to investigate the interaction between micro/nano particles and microchannel wall, so as to achieve a better understanding of the thermal effects on particle deposition. It consists of the following two parts:

- 1) To develop microfluidic systems for direct observation of micro/nano particle deposition in microchannels under controllable thermal environments for different bulk temperatures and temperature gradients.
- 2) To theoretically model and analyse the thermal effect on particle deposition in microchannels, including elevated bulk temperature and temperature gradient.
- 3) To explore an approach for mitigating particle deposition in microchannels at elevated temperatures by manipulating hydrodynamic flows.

The detailed research scope of this study is shown as follows:

- 1) Perform theoretical modelling of the thermal effects on particle deposition in microchannels at elevated temperatures by considering temperature-dependent parameters based on the framework of the Derjaguin-Landau-Verwey-Overbeek (DLVO) theory.
- 2) Design and fabricate microfluidic devices with capability of providing various bulk temperatures in microchannels. Carry out experiments to measure the particle deposition rate at different temperatures.
- 3) Design and fabricate microfluidic devices with capability of providing various temperature gradients in microchannels. Carry out experiments to measure the particle deposition rate at different temperature gradients.
- 4) Design and fabricate microfluidic devices with capability of providing various hydrodynamic flows in microchannels, including steady flow and pulsatile flow.

Conduct experiments to examine the mitigation performances of different flow conditions for the particle deposition at elevated temperatures.

1.3 OUTLINE OF REPORT

The dissertation consists of the following chapters: The preceding section of Chapter 1 introduces the background of this study. The motivation of this research is to gain fundamental understanding of the thermal effects on particle deposition in microchannels at elevated temperatures. The objective and scope of this research are also stated. Chapter 2 presents an extensive literature review on particle deposition and fouling and other issues associated with the present study. In Chapter 3, a theoretical model for particle deposition is developed with consideration of the bulk temperature and the temperature gradient based on the framework of the DLVO theory. Chapter 4 presents an experimental investigation of the bulk temperature on the particle deposition with dilute hydrophobic polystyrene particles (930 nm) in DI water and *NaCl* electrolyte solutions. The details of the designed microfluidic device for controlling the bulk temperature and measurements are introduced. Then the experimental results are analysed by implementing the proposed model. Chapter 5 reports both experimental and numerical studies on the effect of the temperature gradients. The details of a new microchip for generating temperature gradient are described. The proposed model is used to analyse the experimental results. Chapter 6 reports the effect of hydrodynamic flow on particle deposition at elevated temperatures, including both steady and pulsatile flows. The mitigation performance for particle deposition is reported by comparing the results of two different flows. Chapter 7 concludes the major experimental and numerical simulation results from the present study, where recommendations for future work are also included.

Chapter 2

Literature Review

Due to its importance in filtration, food process and heat exchanger, particle deposition has been investigated extensively by researchers. This chapter summarizes research works on fouling and colloidal particle depositions in various environments based on the available publications.

2.1 TYPES OF FOULING

Fouling was first used in the oil and gas industry and started to be widely used to describe any undesirable deposit which resulted in increased thermal resistance of heat exchanger or flow resistance of fluid pipes (Liu, 1999). Most of available literatures on fouling are concentrated on macro-scale phenomena and results, such as change of thermal resistance and hydraulic performances. Generally, fouling can be categorised into various types according to different causes of formation (Bott 1995).

(1) Particulate fouling

Particulate fouling refers to that finely suspended solid particles accumulate onto solid surfaces. The particles are usually with diameters less than microns. Normally, the deposit formed by particulate fouling is thin and easily removed unless accompanied by some other mechanisms which have the particles firmly attached onto the solid surface.

(2) Crystallization fouling or scale formation

Crystallization fouling is deposit of salt crystal onto the heat transfer surface due to the fact that the solubility of the dissolved ions changes with temperature in salt solution. Scale formation could occur when supersaturation of the depositing species in solution is present near the heat transfer surface.

(3) Chemical reaction fouling

Chemical reaction fouling is the deposition formed on the heat transfer surface due to chemical reactions in which solid phases are produced and the surface material is not a reactant. The temperature range for chemical fouling is wide from ambient temperature up to combustion temperature of 2000K. Moreover, it is usually more remarkable at higher temperature range.

(4) *Corrosion fouling*

Corrosion fouling is the deposits accumulate on the surface in a corrosive way when the heat transfer material is chemically attacked by the working fluid. A common example of corrosion fouling is formation of an iron oxide or oxyhydroxide deposit from corrosion of the carbon steel in electrolyte solutions.

(5) *Biological fouling*

Biological fouling usually involves the attachment and subsequent growth of both macro-organisms (e.g. mussels, barnacles and vegetation) and micro-organisms (e.g. bacteria, fungi, algae) onto the heat transfer surface. Because it deals with living matter, the temperature range is limited. Typically, it is between 0 and 90 degree Celsius for biological fouling (Bott, 1995).

(6) *Solidification fouling*

Solidification fouling refers to a pure liquid or one component from a liquid phase frozen onto a subcooled surface. The temperature of the heat transfer surface needs to be lower than the solidification point of the foulant.

(7) *Mixed fouling*

Mixed fouling occurs when two or more of the above fouling mechanisms work simultaneously. During the process, the multiple foulants or fouling mechanisms could interact with each other. This synergistic fouling cannot be simply treated as arithmetic sum of the individual components.

In this report, the author will concentrate on the study on particulate fouling which is relevant to microfluidic applications.

2.2 PARTICLE DEPOSITION

Particulate fouling arises from particle deposition onto the collector/solid surface, which is a complex process influenced by diffusion, convection, colloidal and external interaction forces. To facilitate understanding of the physical process of particle deposition, it can be conceptually divided into three steps (Yang et al. 1998):

(1) Particle transport/diffusion

When particles are at large distances from the collector surface, the particles are transported from the bulk fluid to the collector by diffusion, flow convection and migration due to external forces. Particle concentration gradients usually exist between the bulk fluids to the collector surfaces, and drive the suspended particles approaching the collector surfaces. Flow convection, especially in turbulent flow, could give particles momentum to move across the bulk fluid towards the collector surface. Besides, particles would migrate to the collector when they are affected by external fields, such as gravity field and electric field.

(2) Particle-wall hydrodynamic interaction

When particles get close to the collector within a distance comparable to the particle radius, the motion of the fluid between the particle surface and the collector surface becomes much more difficult compared to the scenario at large distances. It is because that the particles need to experience additional hydrodynamic drag caused by the presence of the collector surface. Thus, the reduction of particle mobility is commonly attributed to the particle-wall hydrodynamic interaction.

(3) Particle adhesion

As particles approach the collector at even closer distances, typically less than 100 nm, the motion of the particles is influenced by colloidal forces besides the hydrodynamic interaction. Within such extremely short distance, the influences of the colloidal forces are overwhelmingly stronger than those of external forces. Thus, the particle adhesion onto the collector is mainly determined by the competition of the attractive and repulsive colloidal forces. The colloidal

forces consist of the universal van der Waals (VDW) force and the electric double layer (EDL) force. These two interaction forces form the basis of the Derjaguin-Landau-Verwey-Overbeek (DLVO) theory of colloidal chemistry. The van der Waals force originates from spontaneous electrical and magnetic polarizations, which generate a fluctuating electromagnetic field within the particle and the collector as well as in the gap between them. Solid surfaces in aqueous media (electrolyte solution) are always charged because of the dissociation of ionisable surface sites or the adsorption of ionic surface active sites. As a result, electric double layers are formed in the vicinity of both the particle and the collector surfaces. When these two charged surfaces approach each other in the electrolyte solution, two electric double layers overlap and a repulsive interaction is developed in this region if the particle and the collector carry the same sign of charge. This repulsive interaction is known as the electric double layer force. In addition, other non-DLVO colloidal interactions might affect the particle deposition in short ranges (0.5 – 5 nm) under certain physicochemical conditions.

2.3 THEORY OF SURFACE FORCES

Particulate fouling or particle deposition are determined by the interaction forces that is exerted on colloidal particles suspended in aqueous media. It is because that the behaviours of particles are dependent on the magnitude and range of the interaction forces between particles and solid surfaces (Liang et al. 2007). In this section, the colloidal forces between particles and surfaces are briefly reviewed. The most familiar colloidal interaction forces are van der Waals attraction force and electrical double layer repulsion force. These two forces form the basis of the Derjaguin-Landau-Verwey-Overbeek (DLVO) theory, which were independently developed by Derjaguin and Landau (1941) from Soviet/Russian and Verwey and Overbeek (1948) from Netherlands. Other than DLVO forces, there are several non-DLVO forces invoked in particle deposition and aggregation, such as hydrophobic forces, steric forces, solvation forces or polymer bridging.

2.3.1 DERJAGUIN-LANDAU-VERWEY-OVERBEEK (DLVO)

THEORY

The DLVO theory proposed that van der Waals attraction and electrostatic repulsion can describe the dominant interactions between two charged lyophobic or hydrophobic particles in electrolyte solution. Besides, it is assumed that the total interaction between particles and solid surfaces in a liquid can be treated as the sum of the two interactions. This is the first theory enabling to explain and predict the experimental data of particle deposition and aggregation in a quantitative way. The van der Waals force is caused by the electromagnetic effects of the molecules composing the particles while the electric double layer force arises from the overlapping of the electric double layer in an aqueous medium. Normally, the former is always attractive and the latter is always repulsive, depending on the material properties (Liang et al. 2007).

2.2.1.1 VAN DER WAALS FORCE

The van der Waals force, also known as London-van der Waals force, originates from the spontaneous magnetic and electrical polarisation which generates a fluctuating electromagnetic field in particles and between particle and solid surface. The van der Waals force can be either attractive or repulsive depending on the material property, and is always attractive between identical materials. A number of methods have been proposed to calculate the van der Waals interaction energy (Hamaker 1937, Dzyaloshinskii et al. 1961, Ninham and Parsegian 1970, Hough and White 1980, Bowen and Jenner 1995). Generally, there are two kinds of methods to calculate the van der Waals interaction: the microscopic and the macroscopic.

For the microscopic methods, Wang (1927) and London (1930) initially used the perturbation theory to solve the Schrödinger equation for the interactions between two hydrogen atoms at a large separation distance, and took consideration of the interactions between the protons and

electrons of the two atoms. Their works provide a basis of quantum-mechanical analysis of the interaction between two non-polar molecules. Thereafter, Margenau (1931) improved the analysis by considering higher moments, and Casimir and Polder (1948) investigated the retardation effect for the interactions with extremely short separation distance shorter than the characteristic wavelength of radiation. Subsequently, Hamaker (1937) proposed a simplified microscopic approximation that the interaction is pair-wise additive. If one simply sums the force over all pairs of atoms in both solids, the total interaction force can be obtained. However, Hamaker's microscopic theory neglects many-body interactions and retardation. Especially for condensed media such as liquid, the influence of neighbouring atoms cannot be ignored. Moreover, the pair additivity is normally difficult to be implemented for bodies interacting in an aqueous medium.

A more rigorous approach accounting for the aforementioned challenges is called the "macroscopic theory". Dzyaloshinskii et al. (1961) proposed a so-called Lifshitz theory to avoid the problem of additivity encountered in the microscopic methods. In their theory, large subjects are taken as continuous media without considering the atomic structure and the interaction forces are calculated based on the bulk material properties, such as refractive indices and dielectric constants. The retardation is implicitly included in the full Lifshitz treatment, but it is fairly easy to modify the Hamaker constant to take account of the effect. The Hamaker constant can be calculated in various approaches and details can be found in the literatures (Gregory 1970, Israelachvili 1972, Horn and Israelachvili 1981, Prieve and Russel 1988).

Hamaker constants are most accurately calculated by Lifshitz theory, which determines the magnitude of interaction through the frequency dependent dielectric properties of the intervening media (Dzyaloshinskii et al. 1961, Horn and Israelachvili 1981). The Hamaker constant is estimated from the frequency dependent dielectric properties of the individual materials comprising the system as

$$A_{132} = \frac{3}{2} kT \left[\frac{I}{2} \left(\frac{\varepsilon_1(iv_0) - \varepsilon_3(iv_0)}{\varepsilon_1(iv_0) + \varepsilon_3(iv_0)} \right) \left(\frac{\varepsilon_2(iv_0) - \varepsilon_1(iv_0)}{\varepsilon_2(iv_0) + \varepsilon_1(iv_0)} \right) + \sum_{j=1}^{\infty} \left(\frac{\varepsilon_1(iv_j) - \varepsilon_3(iv_j)}{\varepsilon_1(iv_j) + \varepsilon_3(iv_j)} \right) \left(\frac{\varepsilon_2(iv_j) - \varepsilon_1(iv_j)}{\varepsilon_2(iv_j) + \varepsilon_1(iv_j)} \right) \right] \quad (2.1)$$

Israelachvili (1992) proposed a simplified expression for the function $\varepsilon(iv_j)$ based on the refractive index and the absorption frequency of materials.

$$\varepsilon(iv_j) = I + \frac{n^2 - I}{v^2} \quad (2.2)$$

The main drawback of this expression is the difficulty to obtain all the parameters used in it, mainly the absorption frequency. Assuming the absorption frequencies of the three media are the same, the Tabor-Winterton (TW) expression was developed to overcome the difficulties, shown as (Tabor and Winterton 1969)

$$A_{132} \approx \frac{3}{4} k_B T \left(\frac{\varepsilon_1 - \varepsilon_3}{\varepsilon_1 + \varepsilon_3} \right) \left(\frac{\varepsilon_2 - \varepsilon_3}{\varepsilon_2 + \varepsilon_3} \right) + \frac{3h\nu_e}{8\sqrt{2}} \frac{(n_1^2 - n_3^2)(n_2^2 - n_3^2)}{(n_1^2 + n_3^2)^{0.5} (n_2^2 + n_3^2)^{0.5} \left[(n_1^2 + n_3^2)^{0.5} + (n_2^2 + n_3^2)^{0.5} \right]} \quad (2.3)$$

where the zero frequency term $\varepsilon_{0,i}$ and refractive index n_i are the temperature-dependent contributions to van der Waals interaction. Because water has a dielectric constant of about 80 at room temperature and non-polar media have values in the range 2-3, the zero frequency term for most of aqueous colloids is about equal to $3kT/4$ or around 3×10^{-21} J.

Suzuki and Higuchi (1969) proposed an expression to approximate the van der Waals interaction potential between sphere and plate with retardation effect, shown as

$$F_{vdw} = \frac{-A_{132}}{6kT} \frac{\bar{\lambda}(\bar{\lambda} + 22.232H)}{H^2(\bar{\lambda} + 11.116H)^2} \quad (2.4)$$

where A_{132} is the Hamaker constant between particles '1' and the plate '3' in medium '2', and is a measure of the magnitude of interaction between two surfaces; $\bar{\lambda}$ denotes the characteristic wavelength of the interaction which has value of about 100 nm for most materials. As shown in Figure 2.1, h is the minimum surface-to-surface separation between sphere and plate, a is the radii

of particle, $\bar{\lambda}$ (λ/a) and H (h/a) are the dimensionless characteristic wavelength and separation distance between the sphere and plate surface.

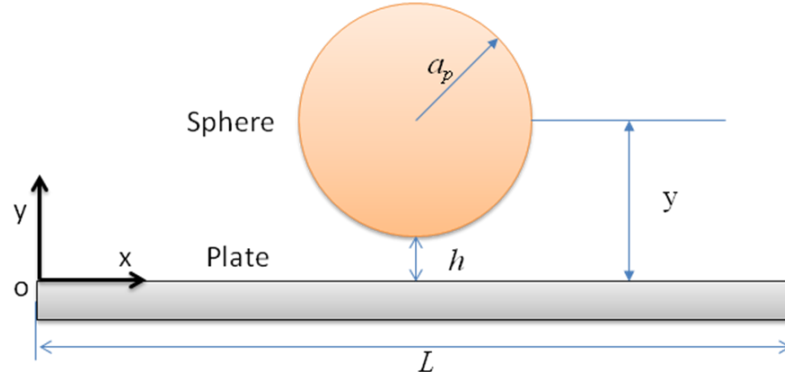


Figure 2.1 Interaction between sphere and plate

2.2.1.2 ELECTROSTATIC DOUBLE-LAYER FORCE

Particle can be well dispersed in liquids other than aggregate together because of the electric double layer (EDL) force. This force originates from the fact that particles and solid surfaces immersed in liquids of high dielectric constants are always charged and the charges form a so-called electric double layer around the particles and the solid surfaces. The charging mechanism of a solid surface in a liquid can be categorised into two: (1) dissociation or ionization of surface groups for the solid surface, (2) binding or adsorption of ions from electrolyte solution onto an originally uncharged solid surface or surface with oppositely charged sites. As shown in Figure 2.2-a, for a single particle immersed in a liquid, the particle is surrounded by the electric double layer. Considering the finite size of ions, Stern (1924) proposed an electric double layer model in which one layer of ions is absorbed and immobilized onto the particle surface and the other layer consists of diffusive space charge from the liquid (Figure 2.2). The former layer is called as Stern layer and the latter layer is termed as Gouy or diffuse layer.

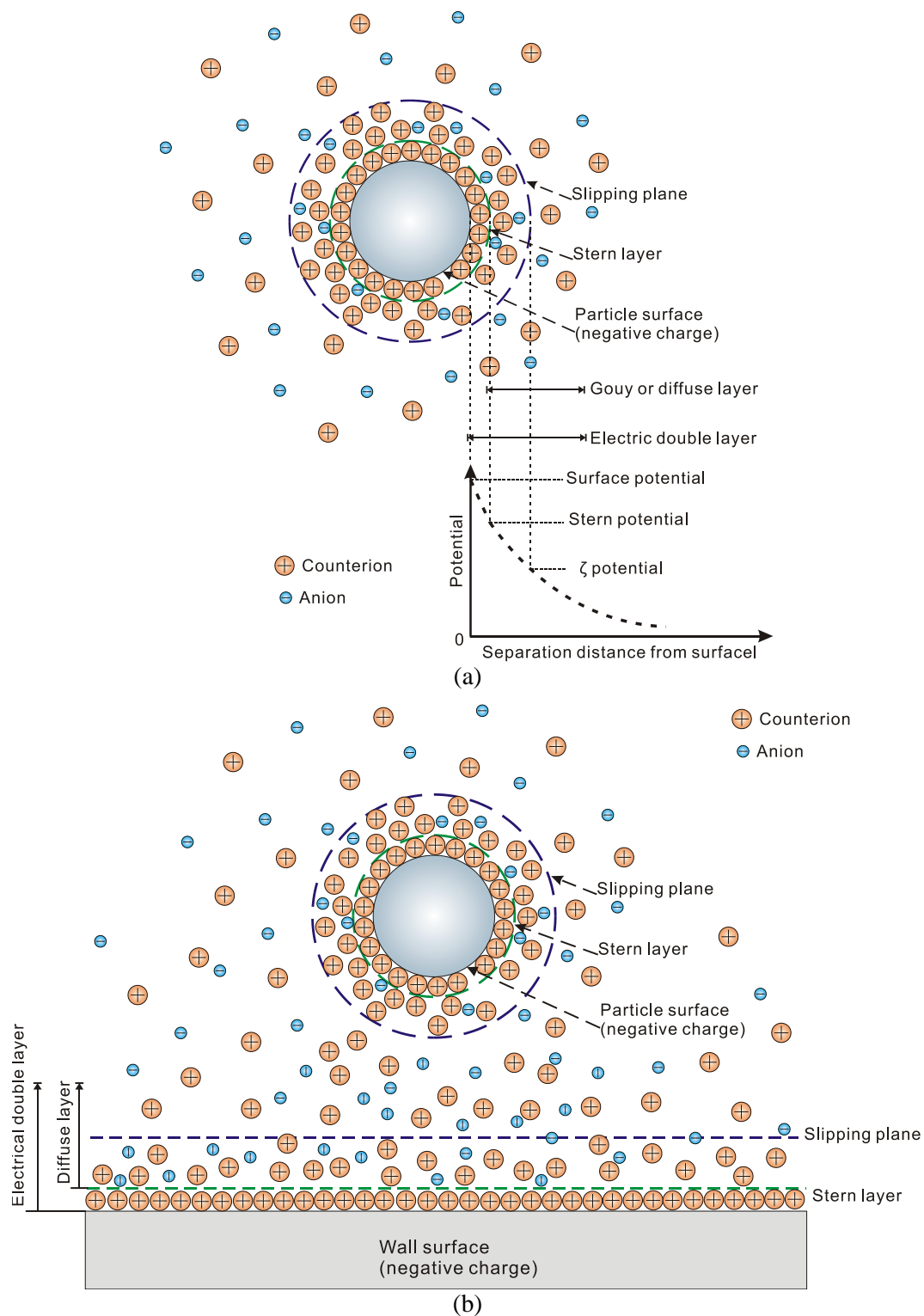


Figure 2.2 Schematic of a diffuse double layer of (a) a charged particle, (b) a charged particle in the vicinity of a charged solid/wall surface.

Because of the distribution of charges around the solid surface, potential decays gradually with increasing the separation distance from the solid surface to the bulk liquid phase. Various

potentials are proposed in the electric double layer model, such as surface potential on the solid surface, Stern potential at the Stern layer and zeta potential (ζ) at slipping plane. The electric potential and the average charge distribution in the diffuse layer of the electric double layer is normally calculated by the non-linear Poisson-Boltzmann equation (PBE) with assumption of the average surface charge over the whole solid surface and ions of identical property as (Anderson 1991)

$$\nabla^2 \psi = \frac{-1}{\varepsilon_0 \varepsilon} \sum_i n_i^0 z_i e \exp\left(\frac{-z_i e \psi}{k_B T}\right) \quad (2.5)$$

where ψ denotes the electric potential, i represents the component i , ε_0 is the permittivity of vacuum, ε is the static dielectric constant, n_i^0 is the number density of ions in bulk, z and e are the valence and the elementary electric charge, and k_B and T are Boltzman's constant and the absolute temperature.

When two charged particles approach each other or a particle approaches a solid surface in an electrolyte solution, diffuse layers of these two particles would overlap with reducing the separation distance between the two surfaces as shown in Figure 2.2-b. EDL force is repulsive for two surfaces with charges of same sign, while it is attractive for two particles with charges of opposite sign. Various factors affect the accuracy of calculating the EDL interaction. Two important assumptions are made for simplification of calculation, interaction with constant surface potential and constant surface charge density. Case of constant surface potential corresponds to that surface-chemical equilibrium is maintained when two particles are approaching with a very short time of encountering. It may not be realistic assumption for some practical cases (Frens and Overbeek 1972). Interaction with constant surface charge assumes that two particles have fixed surface charge density during approach. These considerations apply to the potential and charge at the particle surface, however, the interaction between electrical double layers is determined by the potential at the stern plane which may behave differently during the approach. Recently, Barisik et al. (2014) and Zhao et al. (2015) have implemented a complex charge regulation as boundary conditions to calculate the EDL interactions in nanoscale.

The EDL interaction energy can be calculated by two methods. One method is to directly solve the Poisson-Boltzmann equation for the system under consideration. Usually, simple analytical solutions cannot be obtained by this method. The other method is to construct the formula from known expressions for each of the surfaces involved without effects of the other surfaces. The approximations obtained in this way are often more important for practical uses which require simplicity and fairly accuracy (Elimelech et al. 1995).

Sphere-plate double layer interactions

Derjaguin (1934) proposed the integration method to calculate the sphere-sphere double layer interactions in a dilute suspension. It has been a commonly used method adopted by researchers since then. The EDL interaction energy between two spheres with overlapping electric double layers can be calculated as

$$V_{edl} = \frac{2\pi a_1 a_2}{a_1 + a_2} \int_h^\infty \psi_E dh \quad (2.6)$$

where h denotes the minimum separation distance between two sphere surfaces, a_1 and a_2 are the radii of two spheres. The EDL interaction force can be obtained by differentiating the interaction energy, V_{edl} , with the separation distance, h , as

$$F_{edl} = \frac{2\pi a_1 a_2}{a_1 + a_2} \psi_E(h) \quad (2.7)$$

It should be noted that the above expressions only are applicable for cases in which $\kappa a_p > 5$ and $h \ll a_p$ are valid. The sphere-plate interactions can be derived from sphere-sphere interactions by allowing one of the radii to approach infinity. A constant potential expression to calculate EDL interaction energy and force between a sphere and a plane is developed by Hogg et al. (1966) as

$$V_{edl} = \pi \epsilon_0 \epsilon a (\xi_p^2 + \xi_w^2) \left[\frac{2\xi_p^2 \xi_w^2}{\xi_p^2 + \xi_w^2} \ln \left[\frac{1 + \exp(-\kappa h)}{1 - \exp(-\kappa h)} \right] + \ln [1 - \exp(-2\kappa h)] \right] \quad (2.8)$$

The electrical double layer (EDL) interaction force can be obtained by differentiating electrical double layer interaction energy with separation between two surfaces.

$$F_{edl} = -\frac{\partial V_{edl}}{\partial h} = 2\pi\epsilon_0\epsilon_a\kappa(\zeta_p^2 + \zeta_w^2) \left[\frac{2\zeta_p^2\zeta_w^2}{\zeta_p^2 + \zeta_w^2} \frac{\exp(-\kappa h)}{1 - \exp(-2\kappa h)} - \frac{\exp(-2\kappa h)}{1 - \exp(-2\kappa h)} \right] \quad (2.9)$$

where ζ_p and ζ_w denote the zeta potentials of colloid particle and channel wall, respectively. ϵ_0 and ϵ_r represent the permittivity of vacuum and relative permittivity, respectively. The EDL thickness, also known as Debye length, κ^{-1} is defined as

$$\kappa^{-1} = \left(\frac{2e^2 z^2 n_\infty}{\epsilon k_B T} \right)^{-0.5} \quad (2.10)$$

where n_∞ denotes the bulk number density of ions, z is the valance of ions and e represents the electron charge. These expressions can be applied for cases of small potential when the conditions of $\kappa a_p \gg 1$ and $h \ll a_p$ are satisfied. Alternatively, the EDL interaction can be quantified by using either the complete numerical solution of the nonlinear Poisson-Boltzmann equation or the linear superposition method (Adamczyk and Warszyński 1996). Moreover, a complex statistical mechanical model accounting for ion-ion interactions can be applied for calculating the EDL interaction using the thermodynamic entropy and Helmholtz free energy approach with different boundary conditions, such as constant surface charge density and charge regulation (Kralj-Iglič and Iglič 1996, Briscoe and Attard 2002, Barisik et al. 2014).

The total interaction energy, V , in DLVO theory is obtained by the summation of the electrostatic and van der Waals contributions as illustrated in Figure 2.3. With the electronic double layer potential and van der Waals potential described under previous mentioned assumptions, the total interaction is calculated as

$$V = V_{vdw} + V_{edl} \quad (2.11)$$

Equation 2.11 gives both a theoretical frame work to predict and compare experimentally measured colloidal interactions, and knowledge of how surface interactions can be controlled.

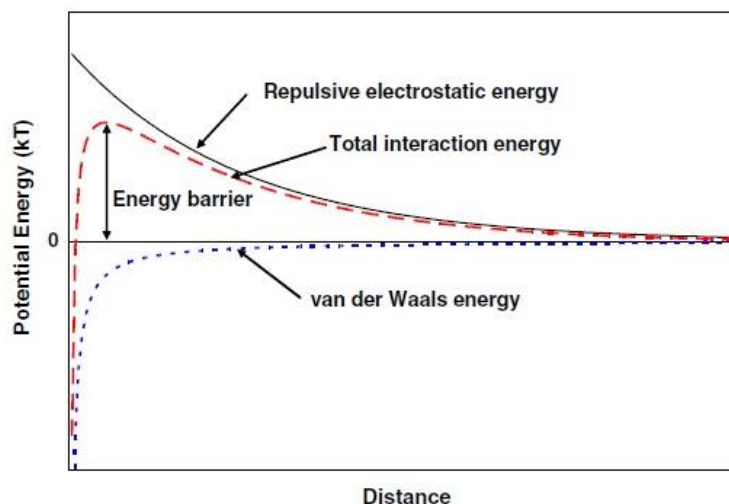


Figure 2.3 Example diagram of potential energy vs separation distance (Perry and Kandlikar 2008)

2.3.2 NON-DLVO FORCES

The classical DLVO theory has demonstrated the importance of van der Waals and electrical double layer interactions and successfully explained a large number of experimental observations. However, there are situations where combination of van der Waals force and electrical double layer force alone cannot achieve satisfactory agreement with experimental results (Verwey and Overbeek 1948, Elimelech 1994). For example, the separation distance between two surfaces is shorter than a few nanometres, and the theories of van der Waals and electric double layer interactions fail in such short distance which are based on continuum theories and described by bulk material properties (e.g. dielectric constant, density, refractive index). For these cases, some type of additional non-DLVO forces are required to be introduced into the DLVO theory, such as polymer bridging (Healy and La Mer 1964), Born repulsion (Ruckenstein and Prieve 1976), hydration forces (Pashley and Israelachvili 1984), hydrophobic interaction (Claesson and Christenson 1988), and steric interaction (Tipping 1988). In this section, a brief introduction for non-DLVO forces is provided and more details can be found in a comprehensive review by Liang et al. (2007).

Polymer bridging theory applies to polymer flocculation. It is postulated that polymer bridges are built between neighbouring solid particles in a suspension in order to form a loose porous 3D network of solid particles (i.e. floc). Elimelech et al. (1995) suggested that it is usually more convenient to resort the microscopically averaged Born repulsion when the precise details of the spatial variation of the short-range forces are not important. Solvation or hydration forces are the terms associated with the forces that develop as particles with adsorbed fluid layers interact. Grabbe and Horn (1993) reported that the hydration force was a dominant repulsive force in short range between silica surfaces immersed in an electrolyte solution (*NaCl*) and this force is independent on electrolyte concentration over the range in their experiments. The physical mechanisms of the hydration force are still an open question. Researchers have proposed that the hydration force originates from the anomalous polarisation of water near the interfaces or the entropic repulsion of thermally activated molecular groups from protrusions on the surfaces (Israelachvili and Wennerstrom 1997, Leckband and Israelachvili 2001, Ruckenstein and Manciu 2002). For hydrophobic surfaces at extremely short separation distance, an attractive force between two surfaces would be increased as the water molecules migrate from the narrow gap to the bulk liquid where the opportunities for hydrogen-bonding are unlimited and free energy is lower than in the gap. This attractive force is referred to the hydrophobic force which is one to two orders of magnitude stronger and works much greater range (up to 80 nm) than the van der Waals force (Israelachvili and Pashley 1984, Claesson and Christenson 1988, Rabinovich and Derjaguin 1988). Steric or osmotic forces are developed for colloidal particles carrying adsorbed polymers. When two polymer-covered particles approach to each other, the entropy of confining these chains caused a repulsive entropic force for overlapping polymer molecules, known as the steric force. Theories of steric forces are not well-established. The magnitude of the steric forces between two polymer coated surfaces is determined by many components, such as the quantity or coverage of polymer molecules on each solid surface and boing stress between the polymer molecules and solid surfaces (i.e. reversible process or not) (Napper 1969, Vrij 1976, de Gennes 1987, Milner et al. 1988).

2.4 TEMPERATURE CONTROL IN MICROFLUIDIC SYSTEMS

Temperature is a crucial parameter in many microfluidic applications, for example microscale milk pasteurisation unit (Tuckerman et al. 2011), polymerase chain reaction (PCR) (Yang et al. 2002, Mavraki et al. 2011), mixing (Kim et al. 2009) and temperature gradient focusing (Becker et al. 2009) or separation (Edwards et al. 2002). Moreover, Lab-on-a-chip device and system are proposed to be a compact platform with multiple functions integrated into a small chip, such as control of temperature. In this section, different techniques for temperature control in microfluidic systems will be summarised into two categories: bulk temperature control and temperature gradient control (Miralles et al. 2013).

2.4.1 BULK TEMPERATURE

This section summarises techniques which have been proposed to regulate bulk temperatures within microfluidic systems. The bulk solution temperatures in the microfluidic systems are uniformly distributed and changed by either external heating or internal heating methods. A number of techniques have been implemented for various applications.

To control the temperature of microfluidic systems, the external heating approaches normally take advantage of commercial heaters, such as Peltier elements, or preheating/cooling liquids prior to being injected into the microsystem. Velasco-Casquillas et al. (2011) designed an external temperature control system with two Peltier elements, in order to rapidly regulate the temperature of yeast channel located underneath the temperature control channel (as shown in Figure 2.4-a). This designed system can readily switch the yeast channel temperature between 5 °C and 45 °C within 10 seconds. Similarly, Khandurina et al. (2000) have implemented two Peltier elements to directly heat up a microfluidic polymerase chain reaction (PCR) chip as a sandwich assembly as seen in Figure 2.4-b. This compact configuration can perform 10 thermal cycles with a total process time of less than 20 minutes. With the similar configuration, Yang et al. (2002) fabricated a serpentine microchannel on a thin polycarbonate plate (thickness: 0.75 mm) as a PCR micro-

reactor as shown in Figure 2.5. Thermocouples were used to monitor the surface temperatures of the Peltier elements and intrachamber temperature. The authors have demonstrated 30 thermal cycles in 30 minutes with $7 - 8^{\circ}\text{C/s}$ for heating rates and $5 - 6^{\circ}\text{C/s}$ for cooling rates.

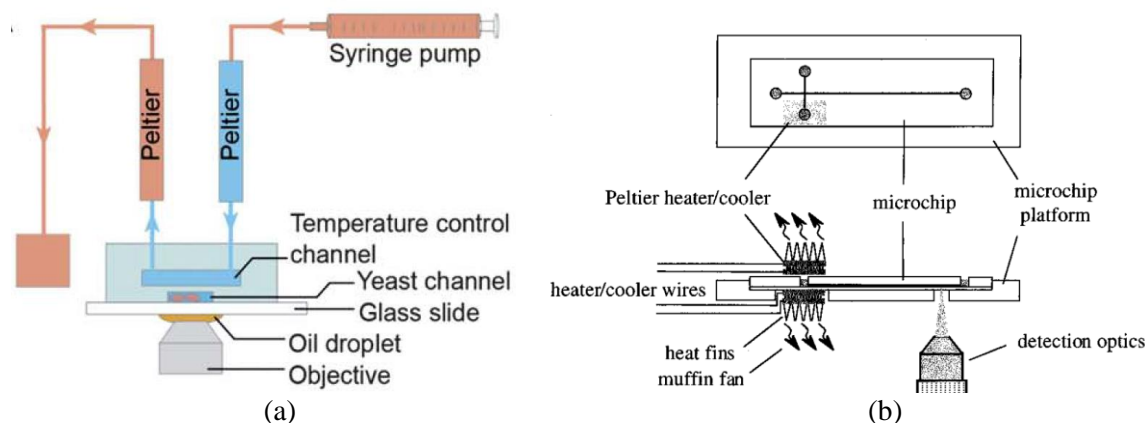


Figure 2.4 (a) A schematic of the temperature control device by an external Peltier element; the yeast channel is placed below the temperature control channel (Velve Casquillas et al. 2011). **(b)** Schematic of the dual Peltier assembly for rapid thermal cycling followed by electrophoretic analysis on-chip (Khandurina et al. 2000).

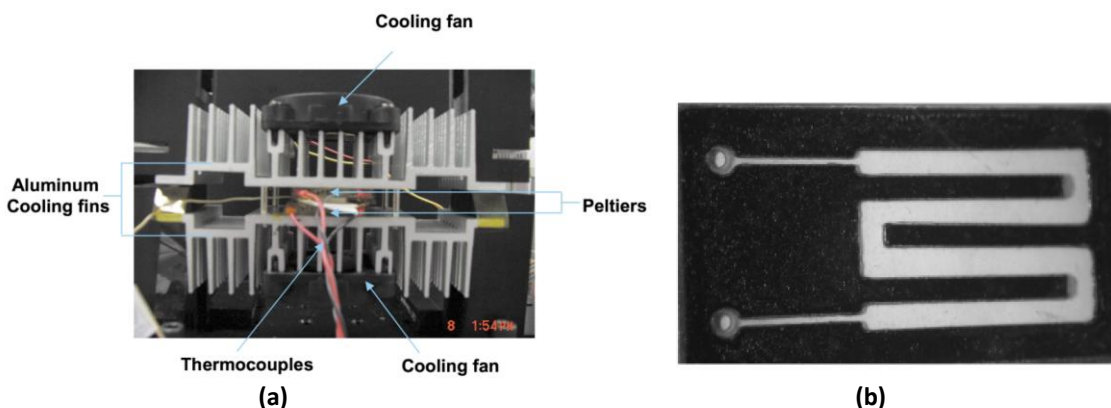


Figure 2.5 (a) Peltier thermocycler for the PCR micro reactor; **(b)** a photograph of the serpentine polycarbonate microchannel (Yang et al. 2002).

Maltezos et al. (2010) explored the limits of PCR speed by using liquid for thermal heat exchange rather than solid as previous researches. As shown in Figure 2.6, sample tubes are immersed in a liquid medium (gallium eutectic) and sandwiched between two high-power Peltier elements. Heat can be rapidly transferred between the DNA/RNA in the sample tubes and the Peltier elements via liquid interface. Heating rate of 106°C/s and cooling rate of 89°C/s have been achieved by their device.

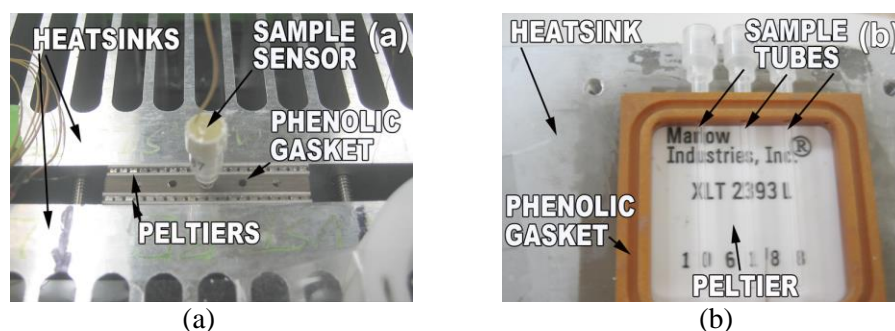


Figure 2.6 (a) Top view of the ultrafast polymerase chain reaction device. Visible is the heatsink-Peltier-phenolic-Peltier-heatsink sandwich that contained the gallium eutectic used for thermal transfer to the sample tube placed where the dummy sample sensor is visible in this photo. (b) Cross section of the heatsink-Peltier-phenolic-Peltier-heatsink sandwich where the sample tube and 2.3 ml gallium eutectic reservoir are visible (Maltezos et al. 2010).

On the other side, techniques have been developed to integrate heating or cooling elements directly into microfluidic systems. Integrated heating approaches are able to reduce the whole system size and improve its portability of the system.

Up to now, Joule heating has been the most popular technique as an integrated solution for the temperature control in microfluidic systems. Lao et al. (2000) integrated platinum heaters and sensors in a silicon-based microfluidic chamber for a well-controlled thermal environment (± 1 °C) for gas and liquid phase reactions as shown in Figure 2.7. The silicon chamber was thermally isolated by a thin silicon nitride membrane to save power consumption, and a digitally feedback system was developed for a precise and prompt temperature control (response time: 5s, heating rate: 20 °C/s, cooling rate: 10 °C/s).

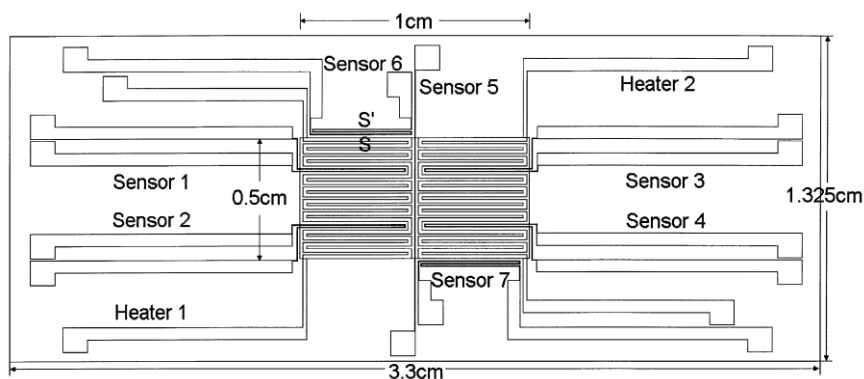


Figure 2.7 Top view of the microchip showing the patterned heaters and temperature sensors (Lao et al. 2000).

de Mello et al. (2004) made use of ionic liquids instead of metal, which was Joule heated by an AC current (frequency: 50 Hz, power: 1 W, Voltage: ≤ 3.75 kV). As shown in Figure 2.8, sample fluids flow in a serpentine microchannel while the ionic liquids ([BMIM][PF₆], [BMIM][Tf₂N]) run in parallel channels. The temperature of sample channel is changed via heat conduction from the co-running heating channels. Consequently, the sample temperature can be easily regulated from 50 °C to 90 °C with an accuracy of 0.2 °C by controlling the applied voltage of the ionic liquids in the heating channels.

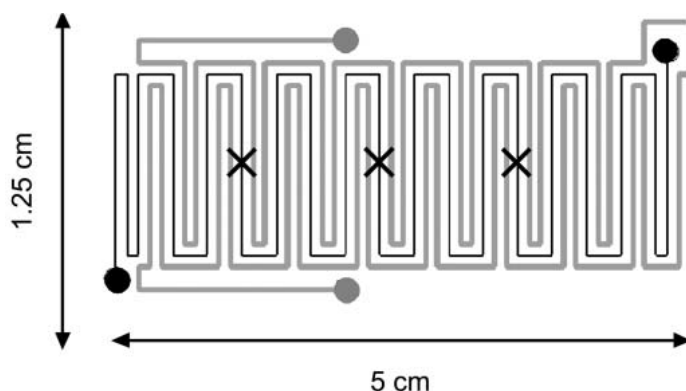


Figure 2.8 Schematic of microfluidic device incorporating co-running heating channels. The working (sample) channel is shown in black and the co-running heating channel in grey (de Mello et al. 2004).

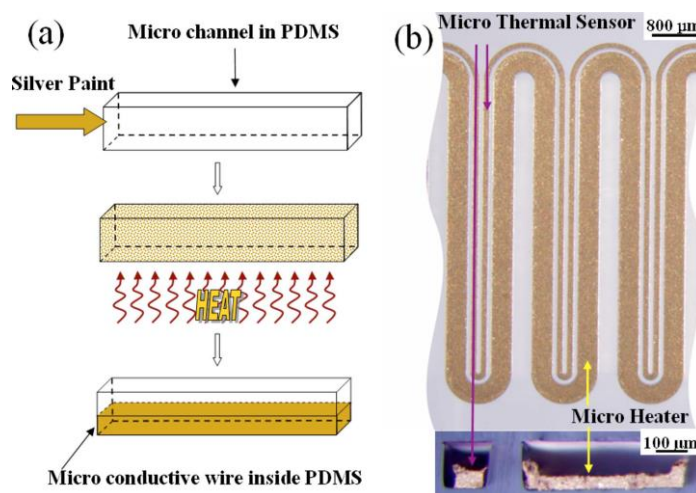


Figure 2.9 (a) Processing flow of conductive microwire inside PDMS using molding injection. (b) Optical images of the microheater and thermal sensor. The upper view is the longitudinal view and the lower, the cross-sectional view (Wu et al. 2009).

By using similar serpentine channel configurations as illustrated in Figure 2.9, Wu et al. (2009) injected silver paint into the PDMS channels as integrated microheaters, and used compressed air for the purpose of rapid cooling in parallel channels. The authors achieved a good

heating rate of 20 °C/s and an error of about ± 0.5 °C in steady state. They successfully amplified DNA in 25 thermal cycles with 1 minute per cycle.

Other than the commonly used physical approach (Joule heating), chemical techniques have also been integrated into microfluidic systems. To locally control temperature in a microchannel, Guijt et al. (2003) have taken advantage of heat generation and adsorption via endothermic and exothermic chemical reactions. As shown in Figure 2.10-a, two reagents from separate reactant channels (RC_1 and RC_2) merge into a temperature control channel (TCC) for chemical reaction, in which heating can be achieved with dissolution of 97 wt% H_2SO_4 (Reagent 1) in water (Reagent 2) and cooling with the evaporation process acetone (Reagent 1) in the air (Reagent 2). A wide temperature range from -3 °C to 76 °C with ramp rate of 1 °C/s has been demonstrated in the central channel (shown in Figure 2.10-b) by manipulating the flow rate ratio between two reagents.

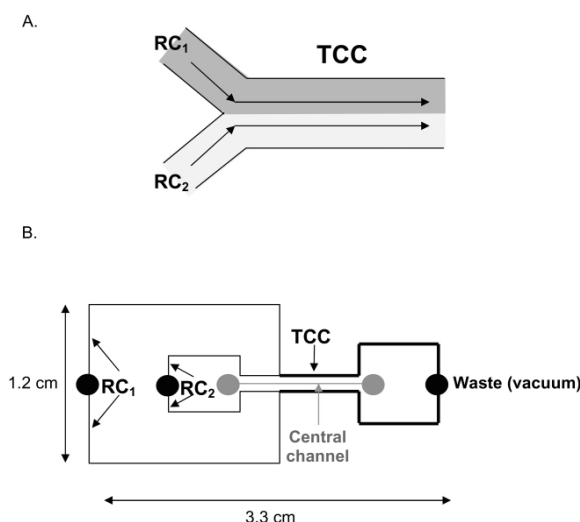


Figure 2.10 (A) Two reactant channels (RC) merging into a temperature control channel (TCC). (B) Layout of the device used for demonstration experiments (Guijt et al. 2003).

2.4.2 TEMPERATURE GRADIENT

For several applications such as Soret effect and droplet actuation, temperature gradients are demanded in microfluidic systems. Temperature gradients have been generated in either a controlled temperature profile or an arbitrary way by various techniques.

Mao et al. (2002) used the pre-heated liquids approach to generate a linear temperature gradient along the horizontal direction of the PDMS microchannel as shown in Figure 2.11-a. Hot and cold fluids were simultaneously channelled into two side channels and a stable temperature gradient was formed in the central channel as seen in Figure 2.11-b. Recently, Zhao et al. (2013) have implemented this approach in their research on thermophoresis with a stainless steel microchip. Because of the higher conductivity of stainless steel than PDMS, their device is able to generate a wider range of variations for both bulk temperature and temperature gradient (1.5×10^4 K/m) in the microchannel.

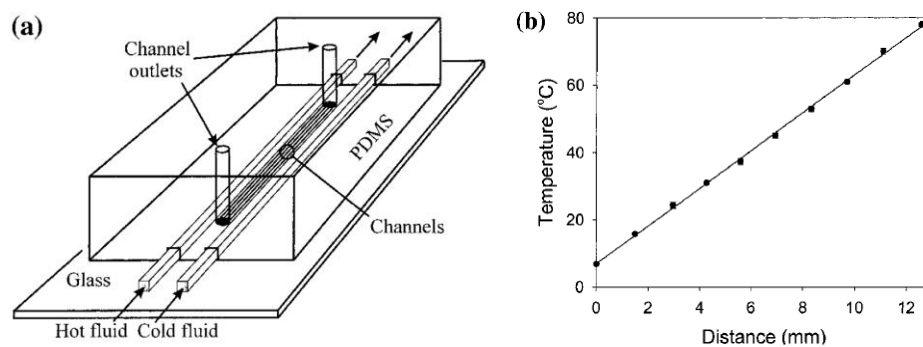


Figure 2.11 (a) Schematic diagram of a device with an on-chip linear temperature gradient. (b) A plot of temperature vs position of the temperature gradient device (Mao et al. 2002).

Vigolo et al. (2010) adopted a similar parallel channel configuration to generate temperature gradients in a microchannel by heating from both sides of the channel as shown in Figure 2.12. However, the authors filled the side channels with conductive silver-filled epoxy that can generate heat via Joule effect. By controlling the applied voltage onto the conductive epoxy, temperature in the microchannel can be changed continuously from 25 °C to 75 °C with an accuracy of ± 3 °C. Temperature was measured by a thermistor attached onto a thin glass cover slip. Because of the low power consumption, the conductive polymers can be powered by two ordinary AAA batteries. Thus, their design could be a portable and cost-effective solution for thermal control in microfluidic systems.

Besides, the parallel-channel configuration can be also utilised to regulate bulk temperatures in microchannels. A uniform temperature field can be generated by changing the directions of preheated liquid and DC electric current.

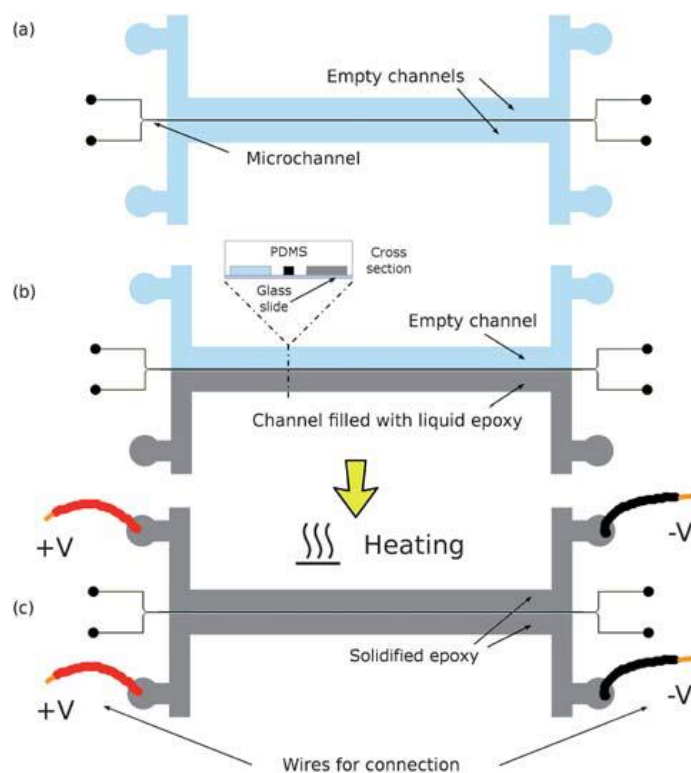


Figure 2.12 A schematic of the device: (a) the empty channel, (b) a channel is filled with a conductive epoxy, (c) the channel is heated until the epoxy solidifies after inserting wires for the electrical connection (Vigolo et al. 2010).

In addition to regulating bulk temperatures, Peltier elements can be utilized to establish a constant temperature gradient in microfluidic systems. Matsui et al. (2007) designed and fabricated a hybrid temperature gradient focusing (TGF) chip (materials: PDMS/glass) by integrating two Peltier elements to generate a temperature gradient along the horizontal direction of the microchannel as shown in Figure 2.13. A temperature gradient of $13.75^{\circ}\text{C}/\text{mm}$ can be generated across the microchannel (4 mm).

Jiao et al. (2008) reported a microfluidic droplet manipulation system with integration of four microheaters (materials: titanium and platinum) providing temperature gradients as shown in Figure 2.14-a. By controlling the amplitude and frequency of square wave signals, various heating processes of four heaters can be achieved, and different plenary temperature gradients can be generated on the square region (10 mm x 10 mm). The authors successfully utilized the periodic thermocapillary actuation caused by temperature gradients to manipulate the trajectory of a microdroplet. Yap et al. (2009) presented a thermal control technique by integration of a thin

film platinum heater for droplet manipulation in a bifurcated microfluidics system as shown in Figure 2.14-b. The viscosity and interfacial tension were varied accordingly with changing the thermal field inside the microchannel, and the tendency of droplets flowing into the branch with higher temperature was increased. Therefore, the motion of droplets and splitting of the droplet can be controlled by controlling the heating performance of the microheater. Using the temperature gradients generated by metal microheaters, Selva et al. (2011) demonstrated a controllable bubble motion by utilizing the thermomechanical actuation, which used the slight dilation of the channel material (PDMS) under temperature variation. The temperature-induced dilation changed the height of the microchannel so that the bubble was driven away from the constricted region. Miralles et al. (2015) from the same research group optimised their previous design by using localised heating resistor whose size was smaller than the droplet size.

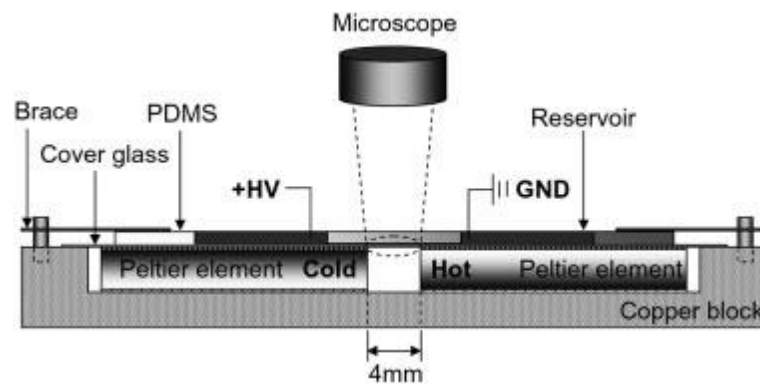


Figure 2.13 Schematic drawing of temperature gradient focusing apparatus (Matsui et al. 2007).

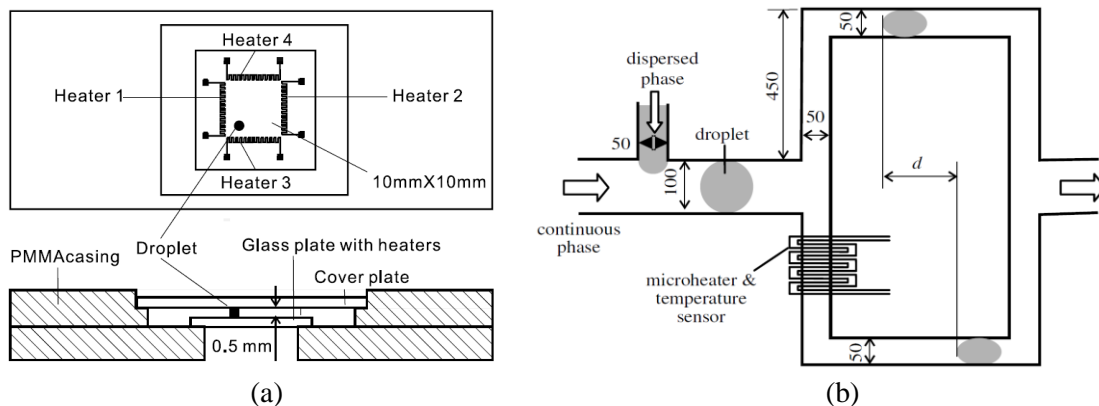


Figure 2.14 (a) Top and side view of the device with four gold heaters placed along a square (Jiao et al. 2007). (b) Schematic of the microchannel system with platinum microheater (Yap et al. 2009).

2.5 PARTICLE DEPOSITION IN MICROCHANNELS

Particle deposition in a channel has been intensively investigated in both theoretical and experimental approaches by researchers. In this section, major works on particle deposition in microchannels are reviewed.

2.5.1 EXPERIMENTAL STUDIES

Researchers have made great efforts on experimentally studying the particle deposition in the cylindrical or parallel-plate channels. Various parameters have been evaluated in terms of their effects on particle deposition, such as pH, electrolyte concentration.

2.5.1.1 EFFECT OF PH ON PARTICLE DEPOSITION

Zeta potentials of particles and microchannel surface are directly related to the pH value of working fluid. Interaction between electrical double layers of same like sign would generate repulsion force and minimize fouling behaviour if repulsion force is large enough. Newson et al. (1988) demonstrated the effect of pH on particle deposition by using haematite particles (diameter: 0.2 μm , concentration: 100 ppm) suspended in a water turbulent flow ($\text{Re} \sim 11000$). They tested with different tube materials: aluminium and 316 stainless steel. Perry and Kandlikar (2008) also achieved effective mitigation of particulate fouling by adjusting the pH value of solution. The reduced deposition rate was mainly attributed to the stronger repulsive EDL interaction as pH increased.

2.5.1.2 EFFECT OF ION CONCENTRATION ON PARTICLE DEPOSITION

Gu and Li (2002a, b) investigated the effect of electrolyte concentration for silicon oil microdrops depositing on cylindrical surfaces in both numerical and experimental manners. It was reported that increase of Sherwood number (dimensionless mass transport rate) was due to the strong neutralization effect of electrolyte concentration ($10^{-6} \text{ M} \sim 10^{-3} \text{ M}$) on the zeta potentials of

silicon oil drops and bare glass tube surfaces. Besides, they also conducted experiments with ionic surfactant: cationic surfactant, CTAB; anionic surfactant, SDS. It was found that Sherwood number increased significantly with increase of CTAB concentration (10^{-6} M \sim 10^{-4} M) but reduced monotonically with adding SDS into the aqueous solution. Kar et al. (2014) conducted experiments on the effect of salt gradients on particle deposition on microporous membranes. Their experimental results showed that the diffusiophoretic particle transport played an important role in colloidal particle deposition when the ions in solution have different diffusion coefficients. Furthermore, Guha et al. (2015) found the diffusiophoresis has significant influence on the colloidal fouling in a low salinity reverse osmosis system.

2.5.1.3 EFFECT OF PROPERTIES OF PARTICLE AND WALL ON PARTICLE DEPOSITION

Salim et al. (2009) presented a study of EOF properties of plasma-polymerized microchannel surfaces and the effects of protein (fibrinogen and lysozyme) adsorption on the EOF behaviour of the surface-modified microchannels. Critically, a non-fouling phenomenon is observed with tetraglyme coating, and enables stable EOF to be induced in the presence of protein.

Mustin and Stoeber (2010) experimentally investigate the particle deposition of polymer microsphere suspensions in microchannels and concluded that particle size distribution played an important role in the dynamics of channel blockage other than particle size alone. Recently, they (2016) conducted particle deposition experiments in a PDMS-based mini impingement jet flow cell and found that the charge heterogeneity and surface roughness of the PDMS surface could be the most plausible reason on account of the discrepancy between the experimental measurement and numerical results of the DLVO and the extended DLVO theories.

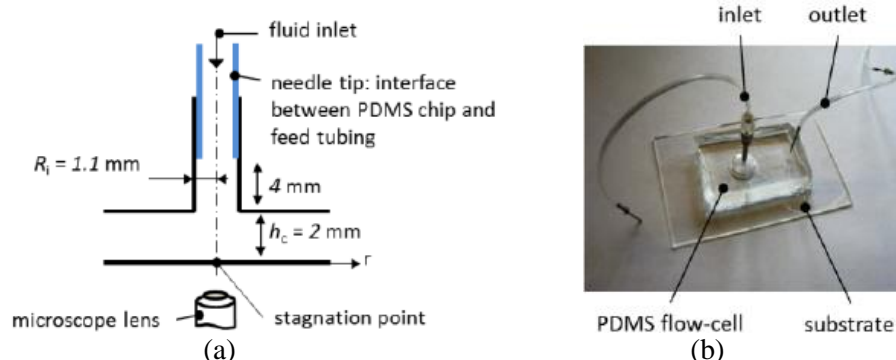


Figure 2.15 (a) cross section view of the deposition chamber, (b) flow cell on substrate without clamping (Mustin and Stoeber 2016).

2.5.1.4 EFFECT OF EXTERNAL FIELD ON PARTICLE DEPOSITION

In the literature, micron-size particle transport is usually treated as a mass transfer process determined by the magnitude of Brownian diffusivity. However, even in this colloidal particle size range (less than 1 μm), gravity or a constant body force towards the deposition surface may significantly affect the deposition process. Yiantsios and Karabelas (1998) found that gravity controlled the deposition rate and the particle transport boundary layer in a horizontal narrow channel under laminar flow over a fairly wide range of flow rate. They (2003) performed another experimental study on dilute micro-sized glass particle ($\sim 1.5 \mu\text{m}$) suspensions in a parallel-plate-laminar-flow channel, and hydrodynamic and physicochemical conditions are systematically varied. It was observed that gravity controls deposition at low wall shear stresses. Particle deposition rates are significantly reduced with the increased hydrodynamic wall shear stress due to the effect of hydrodynamic lift or drag forces inhibiting transport or attachment.

Stamm et al. (2011) experimentally examined the initial stage of cluster growth in a particle-laden flow in a microchannel and investigated the parametric effects of void fraction, flow shear strain rate and channel height to particle diameter ratio. Thereafter, Gudipaty et al. (2011) investigated the cluster formation in a microchannel, and found that the clusters formed on the bottom surface of the channel initially by adherence of individual flowing particle from a top

view using a microscope. However, they didn't address the physical reason of the initial particle adhesion to the bottom surface or observe the adherence process either.

Unni and Yang (2009) observed the particle deposition in electroosmotic flow using videomicroscope and found that the increase in surface coverage corresponding to higher salt concentrations was attributed to weakening of EDL repulsion resulting from adsorbed particle, which circumvents the effects due to reduced electrophoretic particle drag at all stages of deposition. At lower electric field strengths, hydrodynamic blocking became relatively weaker, and the surface blocking was mostly contributed to by electrical interactions.

2.5.2 THEORETICAL MODELLING/STUDIES

Spielman and Friedlander (1974) performed theoretical analysis on the role of the electrical double layer in particle deposition by convective diffusion. It was shown that the deposition of Brownian particles was equivalent to ordinary convective diffusion in the bulk with a first-order surface reaction at the collector and the surface reaction coefficient is derived with respect of the net interaction potential.

An analytical model was proposed by Adamczyk and Van De Ven (1981) for particle deposition kinetics onto walls of parallel-plate and cylindrical channels as shown in Figure 2.16. Mass transport equations were formulated in combination with surface forces, van der Waals force and electrical double layer force, as well as external forces such as gravity. The “perfect sink” boundary condition was discussed in detail along with various dimensionless parameters such as Pe , Gr , Ad and DI , accounting for convection, diffusion, and gravity, dispersion, and electrical double layer, respectively.

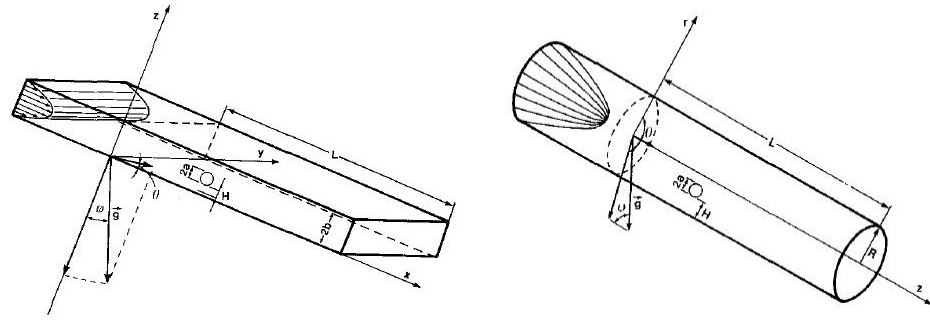


Figure 2.16 Schematics of parallel-plate and cylindrical channels (Adamczyk and Van De Ven 1981)

Song and Elimelech (1993, 1995) theoretically studied the particle deposition onto permeable surfaces in a parallel-plate channel which were practically useful for membrane filtration industry. The convection-diffusion was solved numerically with consideration lateral transport due to permeation drag, inertial lift and transport by surface forces and gravity force. The initial particle deposition rate was investigated systematically in terms of effects of particle size, permeation velocity, solution ionic strength, cross flow velocity.

Nazemifard et al. (2006b, a) conducted a trajectory analysis of particles near a micropatterned charged substrate under radial impinging jet flow conditions in order to investigate the effect of surface charge heterogeneity on particle trajectory and deposition efficiency. The surface charge heterogeneity was determined by concentric bands of specified properties, such as width and pitch, positive and negative surface charges. The particle trajectory analysis took account of the hydrodynamic interactions, gravity, van der Waals and electrostatic double layer interactions. As a result of the coupled effects of hydrodynamic and colloidal forces, the particle trajectories and deposition efficiencies are increasingly affected by surface charge heterogeneity as one moves radially away from the stagnation point. This analysis shows how the existing particle transport models could possibly be modified by incorporating surface interactions and chemical heterogeneity.

Marshall (2007) applied a soft-sphere discrete element method to study the particle aggregation and particle captured by wall in a microchannel. They found that it is more common to see a single particle with large size attached to the wall, but even for such cases the particle lift-

off from the wall was induced by collision and adhesion to a passing particle or particle aggregate, rather than directly by fluid forces.

As shown in Figure 2.17, Unni and Yang (2009) proposed electrokinetic particle transport model in a parallel-plate microchannel based on the stochastic Langevin equation, incorporating the electrical, hydrodynamic, DLVO colloidal interactions and random Brownian motion of colloidal particles. Particle trajectories were stochastically simulated using Brownian dynamics simulation and the surface coverage was evaluated for a range of physicochemical and electrical parameters.

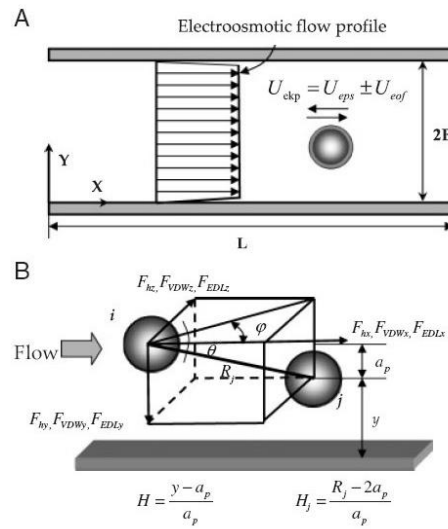


Figure 2.17 Schematic of the parallel-plate channel and force analysis (Unni and Yang 2009)

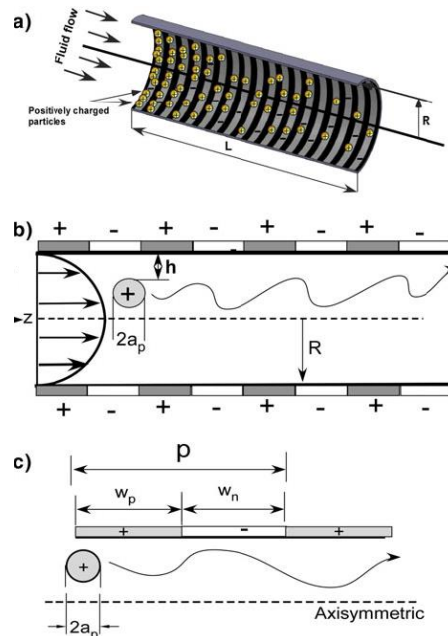


Figure 2.18 Schematic of the patchy heterogeneous cylindrical microchannels (Chatterjee et al. 2012)

Chatterjee et al. (2012) proposed an Eulerian model (convection–diffusion–migration equation) to evaluate particle transport in patchy heterogeneous cylindrical microchannels (as shown in Figure 2.18) for capturing the effect of surface chemical heterogeneity on deposition and particle transport in cylindrical microchannels with fully developed Poiseuille flow velocity profile. It was concluded that particles tend to travel further along the microchannel length for heterogeneous channels compared to homogeneously favourable channels.

2.6 FOULING MITIGATION TECHNIQUES

Because fouling imposes degradation of heat transfer and augmentation of pressure drop in a system and subsequently attenuates the performance of a heat exchanger, various approaches have been proposed for mitigation of fouling, especially in the industrial sector (Kazi 2012). These approaches can be classified into three categories: (1) solution, (2) heat transfer surface and (3) external field.

2.6.1 SOLUTION

For the solution side, a large number of studies have been performed on fouling mitigation via either mechanical methods or chemical methods. Muller-Steinhagen (1993) summarised the mechanical methods which have been developed in the industry sector:

- i. Increase flow velocity
- ii. Reverse flow direction
- iii. Pulsating flow
- iv. Promote turbulence in flow
- v. Add foreign chemicals in solution
- vi. Add seeds or fibre in solution

MÜLLer-Steinhagen and Middis (1989) observed that the deposits of aluminum oxide particles could be removed completely by increasing the flow rate for a short period of time. The

reduction was attributed to the enhanced wall shear stress with flow rate. Similar phenomena have been observed in experimental and theoretical studies (Song and Elimelech 1995, Yiantsios and Karabelas 1995). Reversing flow direction at a regular time interval could be another useful method to reduce fouling. Pulsatile flow can be a good option to increase the level of turbulence and enhance the heat transfer in heat exchanger (Karamercan and Gainer 1979, Ludlow et al. 1980, Gupta et al. 1982). Crystallization fouling can be mitigated by reducing the interface temperature with enhanced heat transfer. Particulate fouling can also benefit from the harmonic motion with oscillatory frequency and leads to mitigation (Moschandreu et al. 2010, Kim and Chun 2012).

Various chemical additive have been applied into working solutions for preventing fouling, such as EDTA sequestering agent, polyphosphates and polyphosphates and poly carboxylic acid (Krisher 1978, Troup and Richardson 1978). Crystal habit would be distorted after adding the chemical agents and formation of large crystals would be prevented. Subsequently, the distorted crystals remain suspended in solution and flow out of the heat exchanger with liquid. Besides, adding seeds (e.g. Calcium sulphate seeds) into working solution has been commercially implemented to reduce crystallisation fouling. Crystallisation prefers to occurring on these seeds other than the heat transfer surface. Kazi et al. (2013) reported that fouling mitigation was achieved by adding natural fibres (long-fibre softwood pulp fibres). For particulate fouling, dispersants are implemented to disintegrate the suspended particles into dispersed fragments which cannot easily settle onto the heat transfer surfaces. Corrosion fouling can be suppressed with addition of corrosion inhibitors, such as chromates and polyphosphates (Müller-Steinhagen et al. 2011).

2.6.2 HEAT TRANSFER SURFACE

For the heat transfer surface, major efforts have been put on surface modification by using superhydrophobic surface or chemical coating in recent years. Recently, Nosonovsky and

Bhushan (2009b) commented that superhydrophobic surface can be a good potential option to mitigate fouling, especially biofouling in underwater applications. In addition to reducing drag, superhydrophobic surfaces can defense the underwater system against adhesion and growth of marine organisms (Genzer and Efimenko 2006, Nosonovsky and Bhushan 2009a). By applying oxidation-reduction reaction, Lee et al. (2012) demonstrated that the morphology of copper can be changed to superhydrophobic with needle-shaped copper oxide nanowires. Their scalable method could be implemented in the industry of antibiofouling surfaces. Furthermore, Brzozowska et al. (2014) combined the techniques of microstructured surface patterning and chemical surface modification together to produce a functional surface toward supressing marine fouling. Recently, Liu et al. (2015) used computational modelling to design a gel-based composite coating which can provide thermoresponsive fouling mitigation mechanism.

Besides, conventional mechanical methods have also been applied on the heat transfer surfaces for fouling mitigation. Muller-Steinhagen (1993) reported that a brief overheating on the heat transfer surface can break deposits because of different induced thermal expansions for deposits and heat transfer surfaces. Deposits could be removed by introducing mechanical vibrations or acoustical vibrations to the heat transfer surfaces.

2.6.3 EXTERNAL FIELD

Treatments with external fields have been investigated for fouling mitigation, including magnetic field and electrical field. Parkinson and Price (1984) reported that fouling could be significantly reduced by the magnetic treatment of water, which can facilitate precipitating the salts. These salts suspended in the bulk liquid and were carried away by the flow. However, others found the effect of magnetic field is negligible (Hasson and Bramson 1985, Bernardin and Chan 1991), and even reported it could increase fouling (Muller-Steinhagen 1993). Electronic anti-fouling (EAF) technology has been demonstrated its potential for fouling mitigation in industry water coolers. RF (radio frequency) electrical field was applied for physical water

treatment and was reported as a useful approach to mitigate crystallisation fouling in cooling water (Tijing et al. 2010, Zhang et al. 2016). The voltage and frequency of the RF field affected the crystal structures.

2.7 SUMMARY

From the published works, it is shown that particle deposition on surface has been extensively studied both theoretically and experimentally. Various parameters have been evaluated such as pH of solution, particle size, and surface property. However, studies based on temperature effect on particle deposition are very scarce. Published research of micro/nano particles suspended in microchannel is mainly conducted in room temperature environment, seldom with high bulk temperature or temperature gradient which are crucial factors for heat exchangers in reality. Driven by the motivation to better understand the particle deposition under different thermal environments, the theoretical studies and experimental tests with microfluidic system are carried out in the present work.

Chapter 3

Modelling for Particle Deposition in Microchannels at Elevated Temperatures

This chapter presents a numerical model of particle deposition onto a solid surface at elevated temperatures. Based on the framework of the Derjaguin-Landau-Verwey-Overbeek (DLVO) theory, the mass transport equation is presented using the Eulerian approach, which takes consideration of diffusion, convection, gravity, hydrodynamic interactions, thermophoretic effect, as well as colloidal interactions (van der Waals force and electric double layer force). In particular, the focus is placed on effects of temperature and temperature gradient, which are usually ignored by previous studies but play important roles in numerous practical applications, such as microchannel heat exchangers.

Figure 3.1 shows the flow chart of the numerical model presented in this chapter. Firstly, the mass transport equation is simplified from two-dimensional to one-dimensional after a proper scaling analysis with assumptions in Section 3.1. Secondly, two classic boundary conditions are implemented to numerically solve the one-dimensional mass transport equation in Section 3.2. Thirdly, the temperature dependence of the forces acting on the particles is discussed in details in Section 3.4. Lastly, the particle concentration distribution and the Sherwood number are calculated by solving the one-dimensional mass transport equation with given boundary conditions and the specified forces at various temperatures in Section 3.3. The focus of this chapter is to establish a numerical model for the particle deposition in microchannels subject to a wide range of physicochemical parameters at elevated temperatures. The temperature dependence of various parameters involved in the particle deposition process is discussed in details.

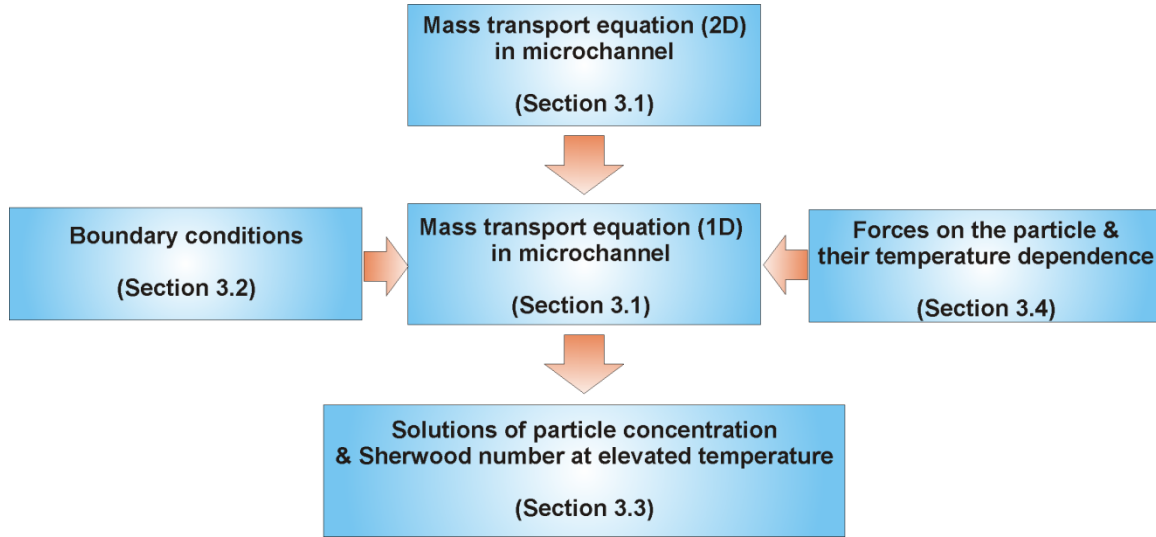


Figure 3.1 Flow chart of the modelling for the particle deposition in microchannels at elevated temperatures.

3.1 MASS TRANSPORT EQUATION

A schematic of microparticles suspended in a microchannel system at elevated temperature (T) is shown in Figure 3.2. Details of the microfluidic system used for experimental investigation of particle deposition will be introduced in Chapters 4 and 5. For a dilute spherical particle monodispersion, in which the interactions between particles are neglected, the deposition rate of particles from the solution onto the microchannel surface can be described by the 2-dimensional mass conservation equation with the assumption of the absence of mass source and sink in the process,

$$\frac{\partial n}{\partial t} + \nabla \cdot \mathbf{j} = \frac{\partial n}{\partial t} + \left(\frac{\partial}{\partial x} (j_x) + \frac{\partial}{\partial y} (j_y) \right) = 0, \quad (3.1)$$

where n is the local particle concentration in number per unit volume, t is time, and \mathbf{j} is the particle flux vector (number of particles per unit area per second).

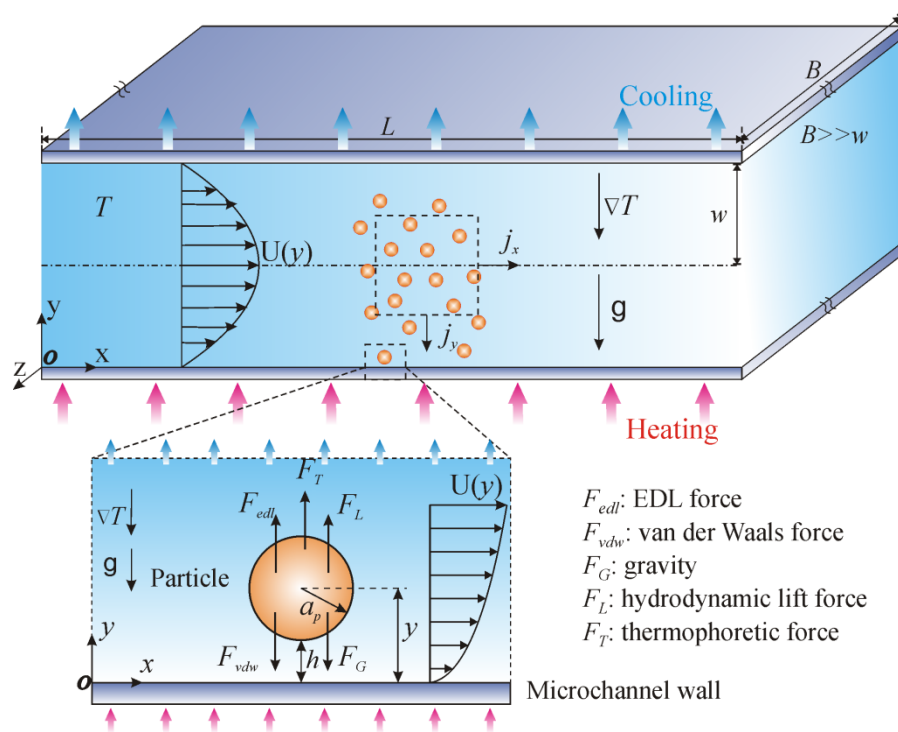


Figure 3.2 Schematic of microparticle transport in a microchannel. The forces on the particle are van der Waals force (F_{vdw}), gravity force (F_G), electric double layer force (F_{edl}), thermophoretic force (F_T), and hydrodynamic lift force (F_L). The radius of the particle is a_p , the minimum separation distance between the particle surface and the bottom surface of the microchannel is h , the flow velocity distribution is $U(y)$, and applied temperature gradient in the microchannel is ∇T . (The figure is not drawn to scale)

In the present study, the transient term in Eq. (3.1) can be dropped when the system reaches a steady state. The mass conservation equation Eq. (3.1) can be simplified to

$$\nabla \cdot \mathbf{j} = \frac{\partial j_x}{\partial x} + \frac{\partial j_y}{\partial y} = 0. \quad (3.2)$$

Moreover, the mass conservation equation can be further simplified to a two-dimensional Cartesian coordinate system because of large aspect ratio ($B \gg w$ shown in Figure 3.2) for microchannels. The flow through the microchannel can be approximated to be a flow between two infinite parallel plates. A fully developed flow field with parabolic velocity profile can be reasonably assumed in the microchannel, and the fluid velocity at the surface of the channel is zero. The particle flux \mathbf{j} in Eq. (3.2) can be decomposed into two portions along the x direction and y direction, $\mathbf{j} = j_x \bar{x} + j_y \bar{y}$. The particle flux along each direction (j_x and j_y) comprises three components: Brownian diffusion, fluid convection, and the migration under various colloidal and external forces. j_x and j_y are expressed as (Adamczyk and Van De Ven 1981, Yang et al. 1998)

$$j_x = -D_x \cdot \frac{\partial n}{\partial x} + U_x n + \frac{D_x F_x n}{k_B T} \quad (3.3)$$

$$j_y = -D_y \cdot \frac{\partial n}{\partial y} + U_y n + \frac{D_y F_y n}{k_B T} \quad (3.4)$$

where D is the diffusion coefficient, U_x and U_y are the particle velocity components along x and y direction, respectively, k_B is the Boltzmann constant, T is the absolute temperature, F_x and F_y are forces exerted on a particle along x and y directions, respectively. In this study, it is worth mentioning that all the forces acting on particles are along the vertical direction (y -axis in Figure 3.2), which consist of colloidal forces (van der Waals force \mathbf{F}_{vdw} , electric double layer force \mathbf{F}_{edl}) and external forces (gravity \mathbf{F}_G , hydrodynamic lift force \mathbf{F}_L and thermophoretic force \mathbf{F}_T). As such, the total force ($\mathbf{F} = \mathbf{F}_y$) can be treated as a scalar in the following sections. The total force (F) is calculated as

$$F = F_y = F_{edl} + F_{vdw} + F_G + F_L + F_T. \quad (3.5)$$

The interaction potential of each force is computed by integrating the force over the separation distance between the particle and the channel surface (h shown in Figure 3.2). The total interaction potential (V) can be obtained from superposition of individual potentials: the van der Waals potential (V_{vdw}), the EDL potential (V_{edl}) and interaction potentials contributed by gravity, lift force and thermophoresis force (V_G , V_L , V_T),

$$V = V_v + V_{edl} + V_G + V_L + V_T = \int F_{vdw} dh + \int F_{edl} dh + \int F_G dh + \int F_L dh + \int F_T dh. \quad (3.6)$$

Near the channel surface, the particle motion becomes retarded due to the additional hydrodynamic drag force exerting on the particle besides the Stokes drag force in unbounded fluid. In order to account for the deviations of particle velocity and diffusivity from the values in bulk flow, the particle velocity and diffusivity are corrected by applying the Universal Hydrodynamic Correction Coefficients (f_1, f_3, f_4) (Adamczyk et al. 1983),

$$f_1(H) = 1 - 0.399 \exp(-0.14869H) - 0.601 \exp(-1.2015H^{0.92667}) \quad (3.7)$$

$$f_3(H) = 1 - 0.3752 \exp(-3.906H) - 0.625 \exp(-3.105H^{0.15}) \quad (3.8)$$

$$f_4(H) = 1 - 1.23122 \exp(-0.2734H) + 0.8189 \exp(-0.175H^{1.2643}). \quad (3.9)$$

The corrected diffusivity (D_x, D_y) and particle velocity (U_x) are given below

$$D_x = f_4(H)D_\infty \quad (3.10)$$

$$D_y = f_1(H)D_\infty \quad (3.11)$$

$$U_x = U(y) = f_3(H) \frac{3}{2} \left[1 - \left(\frac{y-w}{w} \right)^2 \right] U_{avg} \quad (3.12)$$

$$D_\infty = k_B T / 6\pi\mu a_p, \quad (3.13)$$

where D_∞ is the Stokes-Einstein diffusivity, k_B is the Boltzmann constant, and T is the absolute temperature, μ is the dynamic viscosity of the fluid, a_p is the radius of the suspended particle, $H = h/a_p$ represents the dimensionless particle-wall separation distance, h is the minimum separation distance between the particle surface and the bottom surface of the microchannel shown in Figure 3.2, y is the coordinate of the centre of the particle in vertical direction, w is half of the channel height, U_{avg} is the average particle velocity (dividing volume flow rate by the area of cross-section of the channel).

The parameters in Eqs. (3.2-3.4) can be nondimensionalized with the expressions given below:

$$J_x = \frac{a_p j_x}{n_{\infty,p} D_\infty}, \quad J_y = \frac{a_p j_y}{n_{\infty,p} D_\infty}, \quad \bar{n} = \frac{n}{n_{\infty,p}}, \quad \bar{F} = \frac{a_p F}{k_B T_0}, \quad \bar{V} = \frac{V}{k_B T_0}, \quad H = \frac{h}{a_p} = \frac{y - a_p}{a_p}, \quad X = \frac{x}{w}, \quad R = \frac{a_p}{w},$$

$$Pe = \frac{U_{avg} a_p}{D_\infty},$$

where J_x and J_y are the dimensionless particle flux along x and y direction, respectively, \bar{n} is dimensionless particle number concentration, $n_{\infty,p}$ is the particle number concentration in bulk phase, T_0 is the reference solution temperature, and Pe is the Peclet number, indicating the ratio of the advective transport rate by the flow to the diffusive transport rate driven by concentration gradient.

After non-dimensionlising, Equations. (3.2-3.6) can be further written as

$$\frac{a_p}{w} \frac{\partial J_x}{\partial X} + \frac{\partial J_y}{\partial H} = 0 \quad (3.14)$$

$$J_x = -f_4(H) \frac{a_p}{w} \frac{\partial \bar{n}}{\partial X} + \frac{3}{2} f_3(H) Pe \left\{ 1 - [1 - R(1+H)]^2 \right\} \bar{n} \quad (3.15)$$

$$J_y = -f_1(H) \frac{\partial \bar{n}}{\partial H} + f_1(H) \bar{F} \bar{n} \quad (3.16)$$

$$F = F_y = F_{edl} + F_{vdw} + F_G + F_L + F_T \quad (3.17)$$

$$\bar{V} = \bar{V}_v + \bar{V}_{edl} + \bar{V}_G + \bar{V}_L + \bar{V}_T = \int \bar{F}_{vdw} dH + \int \bar{F}_{edl} dH + \int \bar{F}_G dH + \int \bar{F}_L dH + \int \bar{F}_T dH. \quad (3.18)$$

By substituting Eqs (3.15-16) into Eq. (3.14), we obtain

$$\begin{aligned} & -f_4(H) \left(\frac{a_p}{w} \right)^2 \frac{\partial^2 \bar{n}}{\partial X^2} + \frac{3a_p}{2w} f_3(H) Pe \left\{ 1 - [1 - R(1+H)]^2 \right\} \frac{\partial \bar{n}}{\partial X} + \\ & \frac{\partial}{\partial H} \left(-f_1(H) \frac{\partial \bar{n}}{\partial H} + f_1(H) \bar{F} \bar{n} \right) = 0 \end{aligned} \quad (3.19)$$

The variation of deposition rate for a dilute particle solution ($a_p \ll w$) along the x direction in the microchannel was found to be insignificant (Song and Elimelech 1995, Unni 2007). Consequently, the mass transport equation can be further simplified to a one-dimensional case and the final particle transport equation can be obtained as

$$\frac{\partial}{\partial H} \left(-f_1(H) \frac{\partial \bar{n}}{\partial H} + f_1(H) \bar{F} \bar{n} \right) = 0. \quad (3.20)$$

To solve the mass conservation equation, the local particle concentration and particle mass transfer flux can be obtained after knowing the particle velocity, particle diffusion coefficient and all forces acting on a particle. The forces acting on the particle in microchannel will be discussed in detail in Section 3.4.

3.2 BOUNDARY CONDITIONS

Since Eq. (3.20) is a second-order ordinary differential equation (ODE), two boundary conditions are applied to obtain a unique solution for the one-dimensional mass transport equation,

$$\bar{n} = 0 \text{ at } H = H_0 \quad (3.21)$$

$$\bar{n} = 1 \text{ at } H = H_\infty. \quad (3.22)$$

Equation (3.21) expresses the “Perfect sink” boundary condition which has been widely applied in particle deposition studies. H_0 indicates the minimum dimensionless particle-wall distance. This boundary condition assumes that all particles will be irreversibly deposited onto the channel surface once they reach the primary energy minimum (PEM) region. The “Perfect sink” boundary condition indicates that the attractive van der Waals force in the PEM region becomes much stronger than the repulsive electric double layer force so that the particles can be captured. The second boundary condition, as shown in Eq. (3.22), states a natural boundary condition that the particle concentration approaches the concentration in bulk phase when the particle-wall distance approaches an “infinite” distance.

3.3 DETERMINATION OF PARTICLE DEPOSITION RATE

In principle, the dimensionless concentration (\bar{n}) can be calculated out by solving Eqs. (3.20-22) if the required parameters (\bar{F} , H_∞ , H_0) are given. However, it is almost impossible to have any useful analytical solutions to Eq. (3.20) because of the mathematical complexity of the coefficient $f_1(H)$ and the total force (\bar{F}) exerted on the particle. In practice, numerical simulations are implemented to solve the mass transport equation in conjunction with the given boundary conditions. In the present study, a software Comsol Multiphysics (V4.2) is adopted to numerically solve the mass transport equation with an iterative equation solver. The forces acting on the particle are discussed in details in Section 3.4.

With the solved dimensionless concentration distribution (\bar{n}) along the dimensionless separation distance (H), the particle deposition flux to the channel surface can be obtained as

$$J_0 = -f_1(H_0) \left(\frac{d\bar{n}}{dH} \right)_{H=H_0}. \quad (3.23)$$

Here, J_0 is the particle number flux at $H=H_0$. The negative sign on the right hand side of Eq. (3.23) indicates the particle number flux is toward the solid surface. Besides, the dimensionless particle deposition rate onto the channel surface can be quantified by the Sherwood number

$$\text{Sh} = -\frac{j_0}{(D_\infty n_{\infty,p}/a_p)} = f_l(H_0) \left(\frac{d\bar{n}}{dH} \right)_{H=H_0}. \quad (3.24)$$

3.4 COLLOIDAL AND EXTERNAL FORCES

The forces acting on the particles in microchannel include colloidal forces and external forces, as shown in Figure 3.2. The colloidal forces consist of van der Waals force (\bar{F}_{vdw}) and electric double layer force (\bar{F}_{edl}). The external forces include gravity force (\bar{F}_G), hydrodynamic lift force (\bar{F}_L) and thermophoretic force (\bar{F}_T) induced by temperature gradient. \bar{F}_{vdw} and \bar{F}_G are attractive to facilitate the particle deposition while \bar{F}_{edl} , \bar{F}_L , and \bar{F}_T are repulsive to hinder the deposition process. In this study, the non-DLVO forces are excluded in the model for simplicity, such as hydrophobic interaction force and steric force. The total potential energy (\bar{V}) can be plotted versus the dimensionless separation distance (H), and will be used to evaluate the particle deposition process.

3.4.1 COLLOIDAL FORCES

When a microparticle approaches a solid surface in an aqueous media, the particle motion is influenced by two widely recognized types of colloidal forces, the electric double layer force and van der Waals force. These two forces are the basis of the well-known DLVO theory of colloidal stability. The temperature dependence of these forces will be studied in the following sections.

3.4.1.1 ELECTRIC DOUBLE LAYER (EDL) FORCE

In this study, the surface potentials of the particles and the microchannel are assumed as constants, and the approximate *HHF* (Hogg-Healy-Fuerstenau) expressions (Hogg et al. 1966) are adopted to calculate the dimensionless EDL force (\bar{F}_{edl}) and interaction potential (\bar{V}_{edl}) as

$$\bar{F}_{edl} = Dl\tau \left[\frac{\exp(-\tau H)}{1 + \exp(-\tau H)} - Da \frac{\exp(-2\tau H)}{1 - \exp(-2\tau H)} \right] \quad (3.25)$$

$$\bar{V}_{edl} = \frac{1}{2}Dl \left\{ \ln \left[\frac{\exp(-\tau H)}{1 + \exp(-\tau H)} \right] + (Da + 1) \ln [1 - \exp(-2\tau H)] \right\} \quad (3.26)$$

$$Dl = \frac{4\pi\epsilon_0\epsilon a_p\zeta_p\zeta_w}{kT_0} \quad (3.27)$$

$$Da = \frac{(\zeta_p - \zeta_w)^2}{2\zeta_p\zeta_w} \quad (3.28)$$

$$\tau = \kappa a_p \quad (3.29)$$

$$\kappa = \left(\frac{2z^2 e^2 n_\infty}{\epsilon_0 \epsilon kT} \right)^{1/2} \text{ for 1:1 electrolyte} \quad (3.30)$$

where Dl is the double layer parameter indicating the strength of the EDL interaction, Da is the double layer asymmetry parameter which reflects the influence of the difference between zeta potentials of the spherical particle and the solid surface, τ is the ratio of the particle radius (a_p) to the Debye length (κ^{-1}), e is the elementary charge (1.602×10^{-19} C), z denotes the valence of certain type of ion, ϵ_0 represents the permittivity of vacuum, ϵ is the dielectric constant (relative permittivity) of aqueous media (water), T is the absolute temperature of the solution (unit: K).

The *HHF* expressions (Eqs. (3.25-3.26)) have been widely implemented in the particle deposition researches because of their simple analytical forms (Yang et al. 1998, Bhattacharjee et al. 2000, Gu and Li 2002a, Martinez et al. 2008, Bendersky and Davis 2011). These expressions are applicable for the cases with zeta potential below 65 mV and τ beyond 5 in a symmetrical electrolyte as suggested by Hogg et al. (1966). With the help of the *HHF* expressions, the solution

temperature is able to be correlated to the interaction potential curve and the energy barrier as well as the static particle number concentration in the present study.

As shown in Eqs. (3.25-3.30), the EDL interaction between the charged spherical particle and microchannel surface are mainly affected by three components, (1) the magnitude of effective surface potential (ζ), (2) the thickness of the EDL (κ^{-1}), and (3) the geometric configuration of the surfaces. The geometric configurations of particle and channel surfaces are kept the same in the present study, and would not change with the solution temperature. The EDL interaction would not be affected by the geometric configurations in this study.

The magnitude of effective surface potential is generally represented by zeta potential (ζ). It has been reported that the magnitude of zeta potential changes with temperature based on the measurement data in experiments, although the exact physical mechanism is still unknown (Evenhuis et al. 2006, Suganthi and Rajan 2012, Falahati et al. 2014). It is found that the zeta potential is decreased linearly with the solution temperature due to the change of thermodynamic equilibrium of ion adsorption and desorption on the charged surfaces. In this study, the zeta potentials of the microparticles (polystyrene) and microchannel surfaces made of Polymethylmethacrylate (PMMA) and Polydimethylsiloxane (PDMS) at different temperatures are approximated below, based on the empirical correlation given by Evenhuis et al. (2006),

$$\frac{\zeta(T)}{\zeta(25^{\circ}\text{C})} = -0.003698T + 1.0924 \quad (3.31)$$

where $\zeta(25^{\circ}\text{C})$ denotes the zeta potential of charged surface at room temperature, $\zeta(T)$ represents the zeta potential at elevated temperature (T , unit: $^{\circ}\text{C}$). Figure 3.3 illustrates the zeta potentials approximated by Eq. (3.31) with varying temperatures for microparticle and microchannel surfaces in DI water.

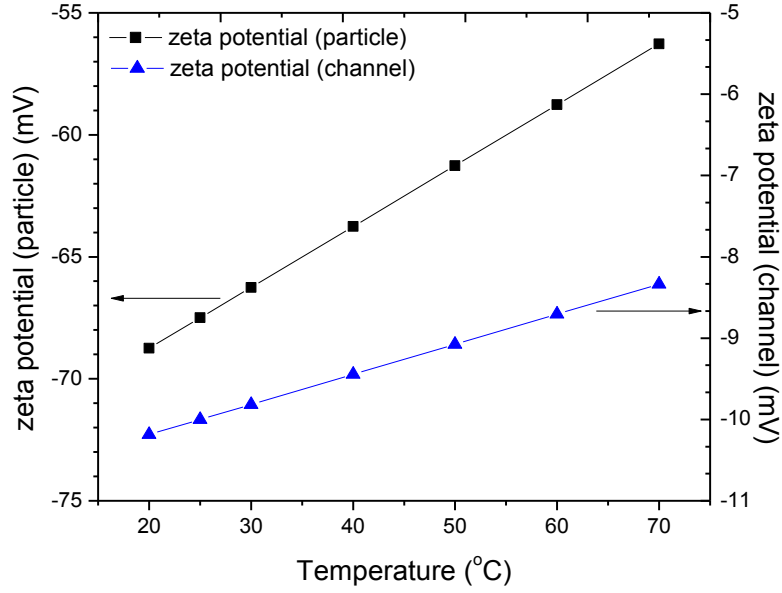


Figure 3.3 zeta potentials of particle and channel surfaces in DI water vs. temperature. Solid square (-■-) indicates the zeta potential of polystyrene particle, and solid triangle (-▲-) indicates the zeta potential of the microchannel surface. Data are calculated for the particles and the microchannel contacting with DI water according to Eq. (3.31).

In addition, zeta potential can be influenced by the electrolyte concentration when the solution temperature remains constant. After reviewing the zeta potential data of various polymeric microfluidic substrate materials, Kirby and Hasselbrink (2004) proposed an empirical correlation with the negative logarithm of the counterion concentration for the materials contacting with univalent electrolyte. In this work, the zeta potentials of microparticle and microchannel surfaces are approximated by a similar correlation as

$$\frac{\zeta(C)}{\zeta(C_0)} = 1 + 0.0566(-\log_{10} C - 2) \quad (3.32)$$

where $\zeta(C_0)$ represents the zeta potential of charged surface with the electrolyte concentration at 5×10^{-3} M, $\zeta(C)$ indicates the zeta potential with varied electrolyte concentration (C , unit: M). The coefficients in Eq. (3.32) were obtained by substituting the zeta potentials in different *NaCl* concentrations measured by Sureda et al. (2012). Figure 3.4 shows the zeta potentials approximated by Eq. (3.32) with different electrolyte concentrations for the microparticles (polystyrene) and microchannel surfaces (PMMA/PDMS), given a fixed solution temperature (50 °C).

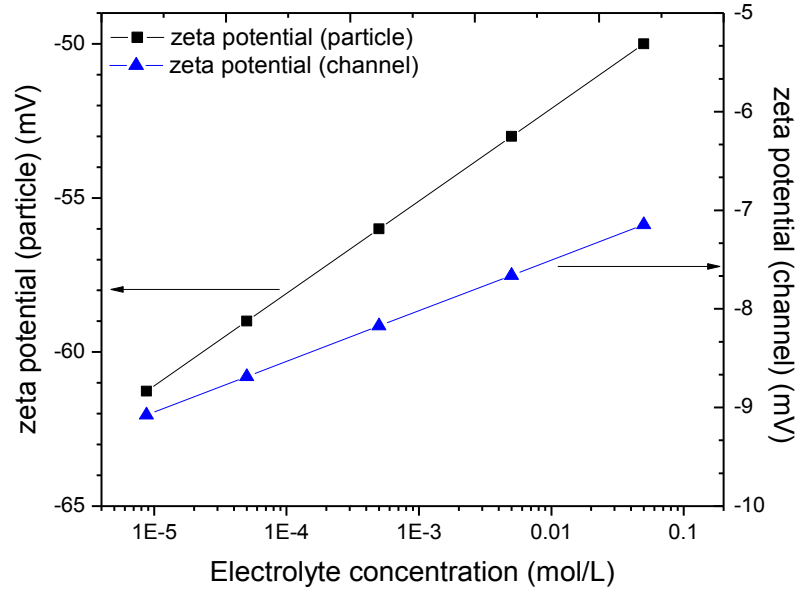


Figure 3.4 zeta potentials of particle and channel surfaces vs. electrolyte concentration. Solid square (-■-) indicates the zeta potential of polystyrene particle, and solid triangle (-▲-) indicates the zeta potential of the microchannel surface (PMMA and PDMS). Data are calculated for the particles and the microchannel contacting with DI water according to Eq. (3.32) while the solution temperature is fixed at 50 °C.

The thickness of electric double layer controls the range of effective interaction, and can be approximated by the Debye length (κ^{-1}). K is defined by Eq. (3.30). The thickness of EDL is determined by the properties of aqueous media (DI water in this study) including number concentration of ion (n_{∞}), dielectric constant (ϵ), valence of ion (z), and the solution temperature (T). The bulk ion concentrations (n_{∞}) can be estimated according to the electric conductivity of the microparticle suspension for the case of DI water and the electrolyte concentration for the case of *NaCl* solution. The number concentration of ion in DI water is affected by the solution temperature due to the strong temperature dependence of the thermodynamic equilibrium of water self-ionization. In this study, the number concentration of ion (n_{∞}) in DI water is extrapolated from the measured electric conductivity (σ) of the microparticle suspension at different temperatures (T) as (Masliyah and Bhattacharjee 2006)

$$\sigma = \frac{2e^2 z^2 D_{H^+} n_{\infty}}{k_B T} \text{ for symmetric electrolyte} \quad (3.33)$$

$$\sigma = \sigma_0 [1 + b(T - T_0)] \quad \sigma_0 = 0.00037 \text{ s/m, } b = 2.2 \quad (3.34)$$

where the conductivity of sample solution at room temperature (σ_0 , 25 °C) was measured by a conductivity meter (Thermo Russell RL380), D_{H^+} represents the diffusivity of hydrogen ion in the solution.

The dielectric constant (ε) is another factor to influence the thickness of EDL. When the solution temperature is changed other than room temperature, the dielectric constant (ε) of the solution (DI water) can be determined based on the correlations published by the International Association for the Properties of Water and Steam (IAPWS 1997b) as

$$\frac{\varepsilon - 1}{\varepsilon + 2} = \frac{N_A \rho}{3} \left[\frac{\alpha}{\varepsilon_0} + \frac{g \mu^2}{3kT \varepsilon_0} \frac{9\varepsilon}{(2\varepsilon + 1)(\varepsilon + 2)} \right] \quad (3.35)$$

$$g = 1 + \sum_{h=1}^{11} N_h (\rho / \rho_c)^{i_h} (T_c / T)^{j_h} + N_{12} (\rho / \rho_c) \left(\frac{T}{228K} - 1 \right)^{-1.2}. \quad (3.36)$$

Eqs. (3.35-3.36) are used for calculating the dielectric constant at different temperatures in the present study. The details of symbols in Eqs. (3.35–3.36) are stated in Appendix A. Figure 3.5 shows the calculation results of Eqs. (3.35-3.36), and illustrates that the dielectric constant of water (ε) is significantly decreased from 79.77 to 54.00 with increasing temperature from 10 °C to 90 °C.

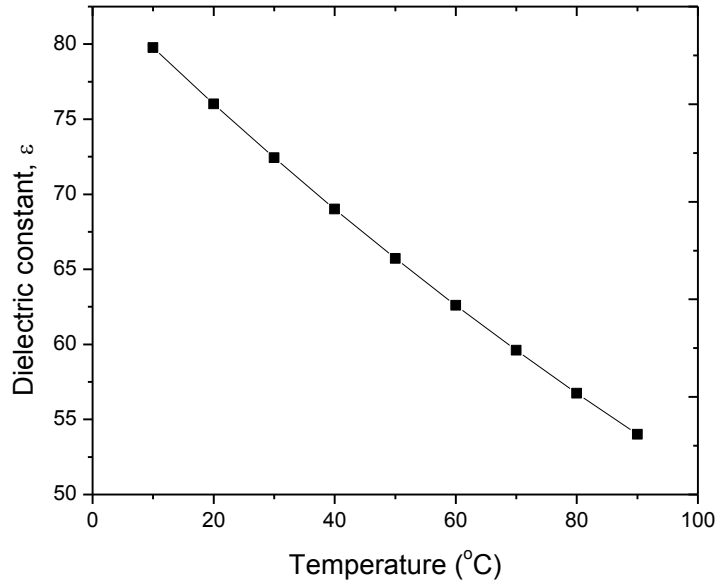


Figure 3.5 Dielectric constant of water versus temperature. Data are calculated for DI water according to Eqs. (3.35-3.36).

The valence of ion (z) is assumed to be constant at different temperatures for simplicity in the present study. Thus, the thickness of the electric double layer (κ^{-1}) at various temperatures (T) can be approximated with consideration of the temperature dependence of number concentration of ion (n_∞) and dielectric constant of water (ε). The EDL thicknesses (κ^{-1}) in water at different temperatures are calculated based on Eq. (3.30) with the corresponding n_∞ and ε , and are plotted versus temperatures in Figure 3.6. It can be observed that the EDL thickness (Debye length, κ^{-1}) in water is decreased from 165 nm to 71 nm with increasing the solution temperature from 10 °C to 90 °C. In other words, the electric double layer is significantly compressed with increasing the temperature.

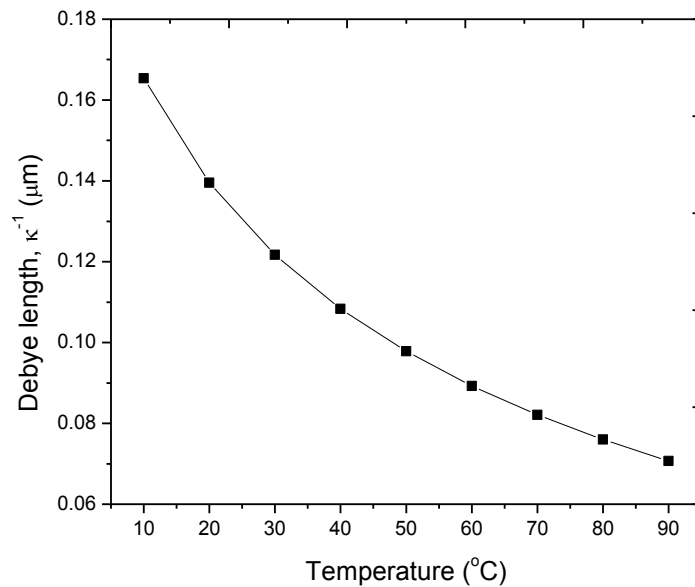


Figure 3.6 Debye length (κ^{-1}) defined Eq. (3.30) in water versus the solution temperature. The solid square (-■-) denotes the Debye length (the thickness of electric double layer). Data are calculated for DI water with consideration of the temperature dependence of the ion concentration, n_∞ shown in Eqs. (3.33-3.34), and the dielectric constant of water, ε shown in in Eqs. (3.35-3.36). The change of Debye length arises from the variation of bulk ion concentration in addition to dielectric constant of DI water.

Based on the discussions above, the thermal effect on the electric double layer interaction can be investigated with considering the temperature dependence of zeta potential and the EDL thickness. The influence of changes of electric double layer interaction on particle deposition will be presented in Chapters 4 and 5.

3.4.1.2 VAN DER WAALS FORCE

The van der Waals force plays an important role to facilitate the deposition of particles when they get close to the channel surface. Suzuki et al. (1969) derived the dimensionless retarded van der Waals force (\bar{F}_{vdw}) and interaction potential (\bar{V}_{vdw}) between the particle and channel surface as

$$\bar{F}_{vdw} = \frac{-A_{132}}{6k_B T_0} \frac{\bar{\lambda} (\bar{\lambda} + 22.232H)}{H^2 (\bar{\lambda} + 11.116H)^2} \quad (3.37)$$

$$\bar{V}_{vdw} = \frac{-A_{132}}{6k_B T_0} \frac{\bar{\lambda}}{H (\bar{\lambda} + 11.116H)} \quad (3.38)$$

where A_{132} is the Hamaker constant for interaction between substances 1 and 2 in medium 2, $\bar{\lambda} = \lambda/a_p$ depicts the retardation parameter, and λ refers to the London retardation wavelength (~ 100 nm), H is the dimensionless separation distance between the particle and the microchannel surface, and T_0 is the reference temperature (293.15 K).

The negative signs at the right hand side of Eqs. (3.37-3.38) indicate that van der Waals force and potential are attractive force and potential. The intensity of van der Waals force mainly depends on the Hamaker constant, A_{132} (1: channel surface, 2: particle, 3: water). By assuming the absorption frequencies of the three substances are the same, Tabor and Winterton (1969) derived a simplified expression for the Hamaker constant at different temperatures as

$$A_{132} \approx \frac{3}{4} k_B T \left(\frac{\varepsilon_1 - \varepsilon_3}{\varepsilon_1 + \varepsilon_3} \right) \left(\frac{\varepsilon_2 - \varepsilon_3}{\varepsilon_2 + \varepsilon_3} \right) + \frac{3h\nu_e}{8\sqrt{2}} \frac{(n_1^2 - n_3^2)(n_2^2 - n_3^2)}{(n_1^2 + n_3^2)^{0.5} (n_2^2 + n_3^2)^{0.5} \left[(n_1^2 + n_3^2)^{0.5} + (n_2^2 + n_3^2)^{0.5} \right]} \quad (3.39)$$

where k_B is the Boltzmann constant (1.381×10^{-23} J/K), T is the absolute temperature, h is Planck's constant (6.626×10^{-34} J·s), ν_e is the main electronic absorption frequency in the UV typically around 3×10^{15} s⁻¹, ε_i refers to the dielectric constant and n_i is the refractive index of three substance (substance 1: channel surface, 2: particle, 3: water). This expression, also known as Tabor-Winterton approximation (TWA), is adopted to compute the Hamaker constant for various temperatures in the present study.

The Hamaker constant (A_{132}) is a temperature-dependent parameter because of the variation of the dielectric constant (ϵ) and the refractive index (n) of materials with temperature. Thus, the thermal effect on the van der Waals forces can be considered by incorporating the temperature dependence of the Hamaker constant into the expressions shown by Eqs. (3.37-3.38). For solids, few data of temperature dependence is available for the dielectric constant and the refractive index. Besides, Chandra et al. (2008) reported that the variation of temperature from 25 °C to 350 °C did not significantly affect dielectric constant and refractive index of Ta_2O_5 . They showed that the variations with the elevated temperature of 300 °C were less than 0.1 for the refractive index and less than 3 for the dielectric constant. In this study, the refractive index and the dielectric constant of both microchannel (substance 1: PMMA/PDMS) and microparticle (substance 2: polystyrene) are assumed to be independent with temperature. The data from the literature are listed in Table 3.1 (Bert 2001), and will be used for modelling in this study.

Table 3.1 Property table of materials (Pressure: 0.101325 Mpa, Temperature: 25 °C)

Material property	Polystyrene particle	PMMA/PDMS wall
Static dielectric constant, ϵ	2.5	2.62
Refractive index, n	1.5917	1.4914

For the present study, only the dielectric constant and refractive index of aqueous media (3: water) are considered to be changed with temperature. The temperature dependence of the dielectric constant of water (ϵ_3) has been studied in the Section 3.4.1.1. The refractive index (n_3) of water at different temperatures (T) is calculated based on the correlations proposed by the International Association for the Properties of Water and Steam (IAPWS 1997a) shown in Eqs. (3.40-3.43). The details of symbols in Eqs. (3.40–3.43) are stated in Appendix A.

$$\frac{n_3^2 - 1}{n_3^2 + 2} \frac{1}{\bar{\rho}} = a_0 + a_1 \bar{\rho} + a_2 \bar{T} + a_3 \bar{\lambda}^2 \bar{T} + \frac{a_4}{\bar{\lambda}^2} + \frac{a_5}{\bar{\lambda}^2 - \bar{\lambda}_{UV}^2} + \frac{a_6}{\bar{\lambda}^2 - \bar{\lambda}_{IR}^2} + a_7 \bar{\rho}^2 \quad (3.40)$$

$$\bar{T} = T / 273.15K \quad (3.41)$$

$$\bar{\rho} = \rho / 1000 \text{ kg} \cdot \text{m}^{-3} \quad (3.42)$$

$$\bar{\lambda} = \lambda / 0.589 \mu\text{m} \quad (3.43)$$

The refractive index of water (n_3) is calculated for different solution temperatures (10 °C – 90 °C), and is plotted versus temperature in Figure 3.7. It can be seen that the refractive index of water (n_3) slightly decreased from 1.334 to 1.321 when the solution temperature increased from 10 °C to 90 °C. Meanwhile, the static dielectric constant (ϵ_3) reduced significantly from 79.77 to 54.00 as shown in Figure 3.5.

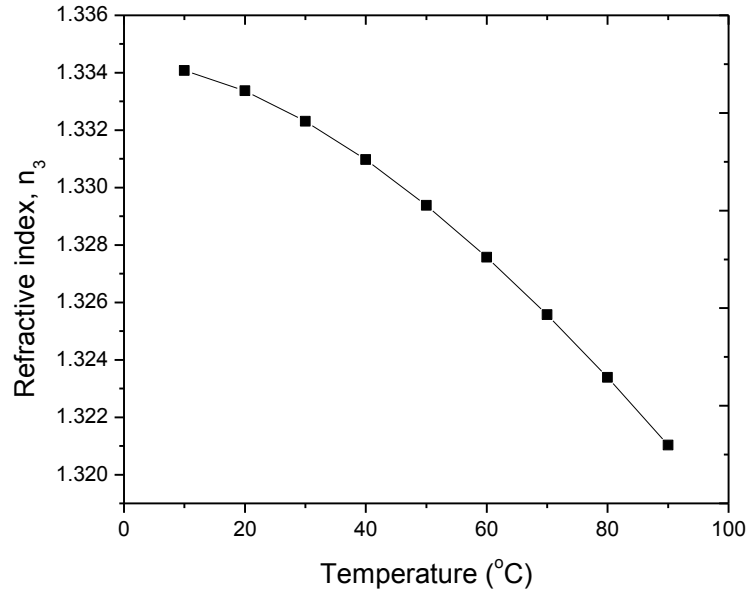


Figure 3.7 Refractive index of water n_3 (-■-) versus the solution temperature. Data are calculated for DI water according to Eqs. (3.40-3.43) with varying temperature from 10 °C to 90 °C.

By substituting the corresponding refractive index and dielectric constant at different temperatures into Eq. (3.39), we can plot the Hamaker constant for various temperatures in Figure 3.8. As seen in Figure 3.8, the Hamaker constant is increased by 15.4% from 9.1×10^{-21} J up to 10.5×10^{-21} J with the temperature elevated from 10 °C to 90 °C, for polystyrene particles interacting with PMMA/PDMS wall via water, which indicates that the van der Waals interaction between particle and channel surface would be enhanced with temperature.

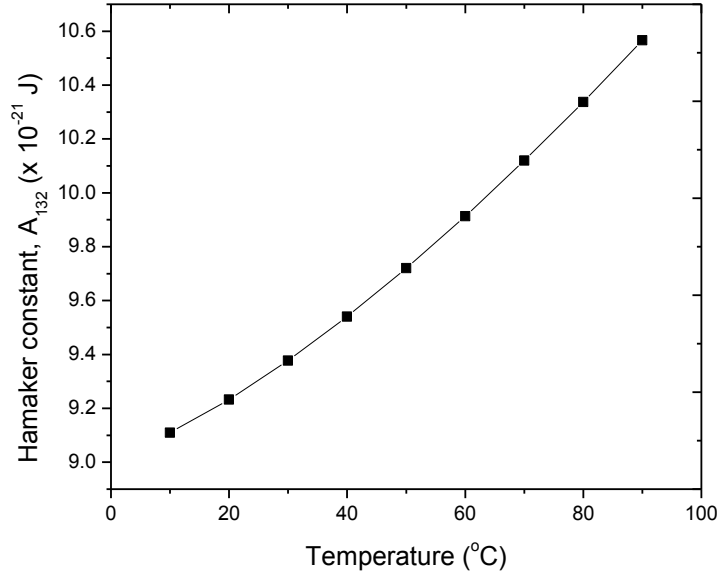


Figure 3.8 Hamaker constant (A_{132} defined in Eq. (3.39)) versus temperature. Data are calculated for the Hamaker constant of the polystyrene particle interacting with PMMA/PDMS surface via DI water. The solution temperature varies from 10 °C to 90 °C. The temperature dependence of Hamaker constant arises from the variation of the static dielectric constant and refractive index of water.

Consequently, the van der Waals force (F_{vdw}) and the van der Waals potential energy (V_{vdw}) can be determined for various temperatures with corresponding Hamaker constants by utilizing the Eqs. (3.37-3.39). The thermal effect, through van der Waals force and interaction potential, on particle deposition in microfluidic channels will be presented in Chapters 4 and 5.

3.4.2 EXTERNAL FORCES

As shown in Figure 3.2, major external forces acting on the microparticles flowing in the microchannel consists of gravity force (F_G), hydrodynamic lift force (F_L) and thermophoretic force (F_T) in the present study. The temperature dependence of these forces will be discussed in this section.

3.4.2.1 GRAVITY FORCE

Gravity force is an attractive external force in the present study and drives particles towards the channel surface from a large distance away. The dimensionless net gravity force and potential are expressed as

$$\bar{F}_G = -\frac{4\pi a_p^4 g}{3k_B T_0}(\rho_p - \rho_l) \quad (3.44)$$

$$\bar{V}_G = -\frac{4\pi a_p^4 g}{3k_B T_0}(\rho_p - \rho_l)H \quad (3.45)$$

where a_p is the radius of polystyrene particle, ρ_p and ρ_l are the densities of particles and DI water, respectively, g is the gravity acceleration, and H is the dimensionless separation distance. The negative signs at the right hand sides of Eqs. (3.44-3.45) mean that the gravity force and potential are attractive to facilitate particle deposition. To calculate the dimensionless gravity in this work, the density of solid particle is assumed as constant while the density of DI water is considered with temperature dependence as listed in Table 3.2 (Maidment 1993, Wagner and Pruess 2002).

Table 3.2 Property table of water at various temperatures (Pressure: 0.101325 Mpa)

Temperature (°C)	Dynamic viscosity, μ (Pa s) $\times 10^{-3}$	Density, ρ_l (kg/m ³)
10	1.307	999.728
20	1.002	998.234
30	0.798	995.678
40	0.653	992.247
50	0.547	988.063
60	0.467	983.211
70	0.404	977.749
80	0.355	971.722
90	0.315	965.163

3.4.2.2 HYDRODYNAMIC LIFT FORCE

When a microparticle flow through a microchannel, the motion of the microparticle near the channel surface can be affected by hydrodynamic lift forces, which include the lift force due to inertia shear (Saffman 1965) and also the Magnus force due to particle rotation. To simplify the model in the present study, particles are assumed flowing in the microchannel without rotation. The lifting effect is solely due to the inertia shear in the fluid. So far, there is no general agreement of the exact expression for the hydrodynamic lift force of particles suspension. Various empirical correlations have been proposed based on experimental and numerical results (Saffman 1965, Leighton and Acrivos 1985, Hall 1988, Mollinger and Nieuwstadt 1996), and it has been

suggested that the hydrodynamic lift force (\bar{F}_L) can be calculated with scaling of dimensionless particle radius (a^+). In this study, the dimensionless hydrodynamic lift force exerted on the microparticle is given by

$$\bar{F}_L = \frac{S_1 a_p}{k_B T_0} (2a^+)^{S_2} \rho_l \nu^2 \quad (3.46)$$

$$a^+ = \frac{a_p u^*}{\nu} \quad (3.47)$$

$$u^* = \left(\frac{\tau_0}{\rho_l} \right)^{0.5} \quad (3.48)$$

$$\tau_0 = \mu \left(\frac{\partial u}{\partial y} \right)_{y=0} = -\frac{3\mu}{w} U_{avg} \quad (3.49)$$

where u^* is the shear velocity, ν is the kinematic viscosity of the fluid (DI water), μ is the dynamic viscosity of the fluid (DI water), τ_0 is the shear stress at the channel surface, ρ_l indicates the density of fluid (DI water), w represents the half of the height of the channel, U_{avg} is the average fluid velocity (dividing volume flow rate by the area of cross-section of the channel). The coefficients, S_1 and S_2 , are selected from published works by Hall (1988) and Saffman (1965). The positive signs on the right hand side of Eqs. (3.46) indicate the lift force and its potential are repulsive to prevent particle deposition.

The lift potential (\bar{V}_L) can be obtained by integrating the lift force with the separation distance (H) at different temperatures as

$$\bar{V}_L = \frac{S_1 a_p}{k_B T_0} (2a^+)^{S_2} \rho_l \nu^2 H. \quad (3.50)$$

The viscosity (μ) and density (ρ_l) of DI water at different temperatures are obtained from the published data sheet as shown in Table 3.2 (Maidment 1993, Wagner and Pruß 2002). As a result, the hydrodynamic lift force at different temperatures can be computed with the corresponding fluid properties at elevated temperatures. The effect of the hydrodynamic lift force on particle deposition at elevated temperatures will be presented in Chapters 4 and 5.

3.4.2.3 THERMOPHORETIC FORCE

Under a temperature gradient, colloidal particles in a liquid solution could migrate to the cold or to the hot depending on the solute and solvent properties, also known as thermophoresis or Soret effect. The complex physical mechanism of thermophoresis in liquid is still a challenging subject. The dispersed particle under a temperature gradient will be given a steady drift velocity in addition to the Brownian motion. This velocity can be obtained by using thermal diffusion coefficient (D_T) and temperature gradient (∇T) as (Piazza 2008)

$$V_T = -D_T \nabla T \quad (3.51)$$

where D_T is the thermal diffusion coefficient, ∇T denotes the applied temperature gradient.

Meanwhile, the drift velocity shown in Eq. (3.51)) can also be expressed as

$$V_T = -\omega F_T \quad (3.52)$$

where F_T is the thermophoretic force which drives the particle moving along the direction of the temperature gradient, ω depicts the mobility of the particle which is determined by the Stokes-Einstein friction factor (f) as

$$\omega = \frac{1}{f} = \frac{D}{k_B T} . \quad (3.53)$$

By substituting Eqs. (3.52-3.53) into Eq. (3.51), we can obtain the dimensionless thermophoretic force as

$$\bar{F}_T = k_B T S_T \frac{dT}{dy} \frac{a_p}{k T_0} = \frac{dT}{dy} \frac{T}{T_0} S_T a_p \quad (3.54)$$

where T_0 indicates the reference temperature (293.15 K), dT/dy is the temperature gradient formed in the microchannel as shown in Figure 3.2, S_T depicts the Soret coefficient ($S_T = D_T/D$) which is taken as 1 K^{-1} based on the available literatures (Eslahian et al. 2014). The positive sign at right hand side of Eq. (3.54) indicates a repulsive potential to impede particle deposition. By integrating the thermophoretic force with separation distance (H), we obtain the dimensionless thermophoretic interaction potential at different temperatures as

$$\bar{V}_T = \frac{dT}{dy} \frac{T}{T_0} S_T a_p H \quad (3.55)$$

With given temperature gradient in experiments, the effect of the thermophoretic force on particle deposition at elevated temperatures will be discussed in Chapters 4 and 5.

3.5 SUMMARY

In this chapter, a one-dimensional mass transport model on the basis of the modified DLVO theory is built with consideration of thermal effect on the colloidal forces ($\bar{F}_{vdw}, \bar{F}_{edl}$) and external forces ($\bar{F}_G, \bar{F}_L, \bar{F}_T$) at elevated temperatures. It is found that the material properties are changed with temperature over a wide range, leading to the changes of these forces. For electric double layer forces, its change is mainly attributed to the variations of the zeta potential and the thickness of electric double layer with changing the temperature. The zeta potential is decreased by 18%, and the thickness of the electric double layer is compressed by 41% with increasing the solution temperature from 20 °C to 70 °C as shown in Figures 3.3 and 3.6, respectively. The intensity of van der Waals force depends on the Hamaker constant. The Hamaker constant is increased by 9.6% with increasing temperature from 20 °C to 70 °C as illustrated in Figure 3.8. Moreover, the external forces are also affected by the temperature because the material properties are changed with temperature. Therefore, the thermal effect cannot be ignored in the study of particle deposition in microchannels at elevated temperatures. The thermal effect on the particle deposition in microchannels will be investigated by numerically solving the proposed model with the given experimental conditions in Chapters 4 and 5.

Chapter 4

Effect of Bulk Temperature on Particle Deposition in Microchannels

In this chapter, a microfluidics system, including a microchip and a fluid supply system, is designed and established. The microfluidic system enables a direct observation of the process of particle deposition for a stationary particle suspension in microchannels with different bulk temperatures. Systematic studies are conducted by both experiments and theoretical modelling. The effects of bulk temperature on particle deposition in microchannels are investigated. The model derived on the basis of the modified Derjaguin-Landau-Verwey-Overbeek (DLVO) theory in Chapter 3 is implemented to analyse the effect of the bulk temperature on particle deposition. The calculated results from the derived model are compared with experimental results.

4.1 EXPERIMENT

There are two measurement methodologies for particle deposition studies: indirect or direct methods. The indirect methods evaluate deposition of colloidal particles by measuring relevant parameters of deposited colloidal particles, e.g. change of colloidal concentration between inlet and outlet, mass of bulk suspension measured over time and intensity of light scattered by the deposited particles. The major limitation of the indirect method is that it cannot quantify the attachment and detachment of particles or spatial and temporal distributions on the surface. The direct methods can easily overcome the limitations associated with the indirect methods with the help of videomicroscope and image processing techniques, such as phase contrast light scope and fluorescent microscope. In this research, the direct method is adopted by using an inverted fluorescent microscope.

4.1.1 EXPERIMENTAL SETUP

The experimental set-up is schematically illustrated in Figure 4.1. It consists of three parts: the microchip, the data acquisition system and the fluid supply system. The microchip is made of two Polymethyl methacrylate (PMMA) plates. The details of the microchip will be introduced in Section 4.1.1.2. The microchip is secured to the chuck of an inverted fluorescent microscope (Nikon Eclipse TE2000-U, Japan) equipped with a CCD camera (Retiga Exi Fast 1394, Qimaging). The CCD camera and thermocouples compose the data acquisition system. Digital videos and images of the particle deposition onto the channel bottom surface are captured by the CCD camera throughout experiments with the captured area of interest fixed at the axial centre point of the deposition channel. Three K-type thermocouples are used to measure the temperature in the deposition channel. The fluid supply system consists of two syringe pumps for channelling hot water. Hot water is continuously supplied to the heating channel in a counter-flow manner with a constant flow rate by two syringe pumps (Yan et al. 2015).

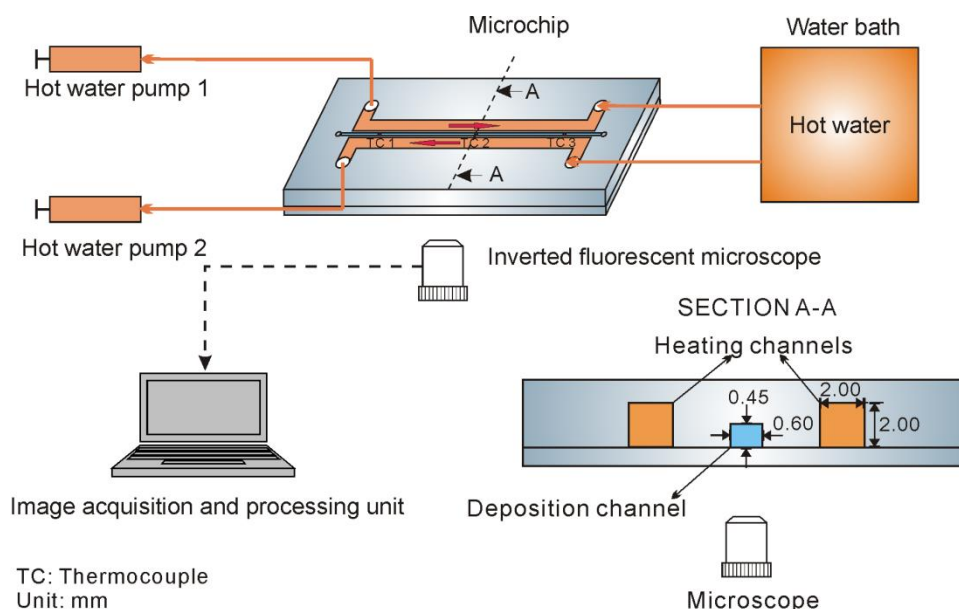


Figure 4.1 Schematic of the microfluidic system for the direct observation of the particle deposition kinetics in microchannels. Inset: Cross-section view of the microchip. Three thermocouples are used to measure the solution temperature in the deposition channel (unit: mm). (Figure is not drawn to scale)

4.1.1.1 MATERIALS

In this study, commercially available polystyrene microparticles (R900, Duke Inc., USA) are used. The particles have a density of 1.05 g/cm^3 and a diameter of $0.93 \mu\text{m}$ (a_p) with a size variation of up to $0.03 \mu\text{m}$. The polystyrene particles are hard-dyed (internally-dyed) with red fluorescence throughout the polymer matrix with the utilisation of FirefliTM process from Thermo-Fisher Scientific Inc. This provides highly stable properties insensitive to temperature change. Particle samples are prepared by first diluting a particle dispersion with a concentration (n_∞) of $5.6 \times 10^6/\text{ml}$ into de-ionized (DI) water and then putting into sodium chloride solutions (Sigma-Aldrich, ACS reagent, $\geq 99.0\%$) with three different electrolyte concentrations, $5 \times 10^{-3}\text{M}$, $5 \times 10^{-4}\text{M}$, and $5 \times 10^{-5}\text{M}$. The samples are homogenized by using an ultrasonic bath (Elmasonic E30H, Elma Ultrasonics) for half an hour before loading into the deposition channel for testing. The ambient temperature of the laboratory is kept at $25.0 \pm 1.0 \text{ }^\circ\text{C}$ for all the experiments.

4.1.1.2 MICROCHIP

Figure 4.2 shows a microfluidic device employed for studying the thermal effect on particle deposition. The microchip is designed based on the idea of counter-flow heat exchanger, and consists of two types of channels: heating channels (2.00 mm in width and 2.00 mm in height) and deposition channels (0.60 mm in width and 0.45 mm in height). The pattern of microchannels is grooved on a Polymethyl methacrylate (PMMA) plate (with dimensions of 24.00 mm in width, 50.00 mm in length, 3.00 mm in thickness) by using a laser cutting machine (Universal Laser 100, USA). The interval between neighbouring channels is 1.00 mm. Thereafter, the grooved PMMA plate is fused with a plane PMMA plate to form an enclosure via the thermal-bonding approach. To generate relatively uniform thermal environment in the deposition channel, a counter flow of two hot water streams is continuously sucked by two syringe pumps (Longer pump LSP02-1B) from a thermostatic water bath (Julaba, Germany) to the heating channels. The

flow rate of hot water is fixed to provide a stable thermal environment during tests. The temperature field in the deposition channel can shortly reach steady state by conduction of heat from two lateral heating channels. With this microchannel design, a controllable thermal environment can be achieved by readily adjusting the water temperature in the thermostatic water bath. Moreover, this design allows to directly observe the dynamic process of particle deposition with aid of a microscope as shown in Figure 4.2. The temperature field in the deposition channel is measured with three thermocouples (TC1, TC2, TC3) which are positioned along the channel as illustrated in Figure 4.2.

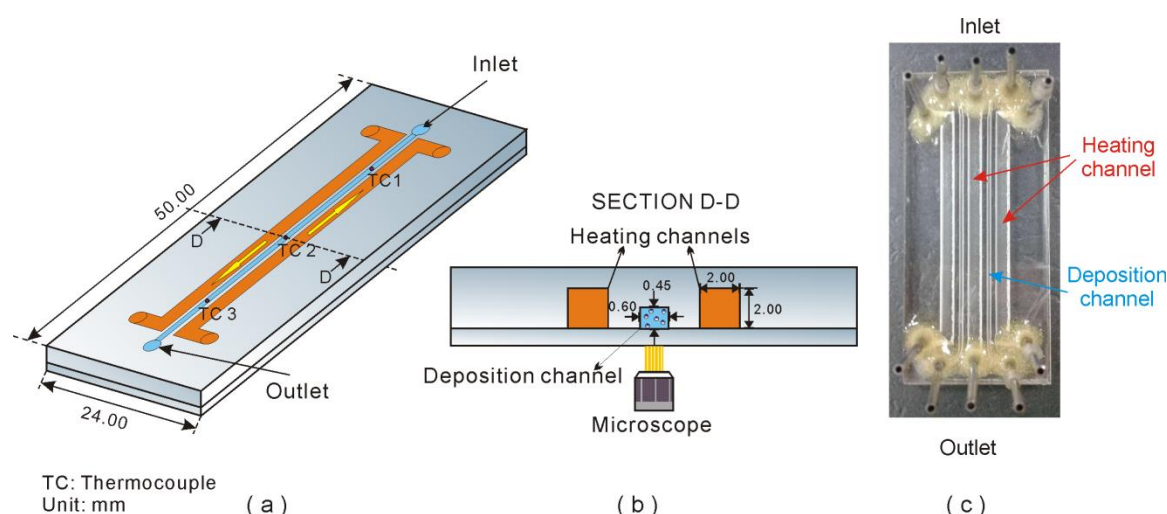


Figure 4.2 Schematic of the microchannels (a) Isometric view, (b) Cross-section view, (c) Image of the microchip used in the experiments. The microchannels are formed by thermally bonding one PMMA plate with designed patterns and one plain PMMA plate together. Inset shows the dimensions of microchannels. Three thermocouples (TC1, TC2, TC3) are used to measure the solution temperature in the deposition channel (unit: mm) (Figure is not drawn to scale).

4.1.1.3 CHARACTERISATION OF THERMAL FIELD IN MICROCHANNEL

In order to obtain the thermal field for particle deposition in the channel, three K-type thermocouples were used for characterisation. The thermocouples were calibrated carefully before the commencement of the experiments.

Three micro-thermocouples (TTC-40-K1, 0.08 mm in diameter) were calibrated together with a HP 34970A Data Acquisition Unit. A thermal calibrator with an adjustable pre-set temperature was used as a heat source. All thermocouples were inserted inside a cylindrical chamber in the thermal-calibrator, where they were heated up to a temperature which was manually set as the

standard temperature. The other ends of thermocouples were connected to the different channels of the HP 34970A Data Acquisition Unit. The analogue data of voltages for the different temperatures provided by the thermal calibrator were collected by the data acquisition card. The HP 34970A was well configured with an integrated thermocouple calibration function including cold junction compensation. Hence, the input analogue data of voltages can be converted to the values of temperatures. The calibration curve of the measured temperature against corresponding output standard temperature and the fitting equation are plotted in Figure 4.3.

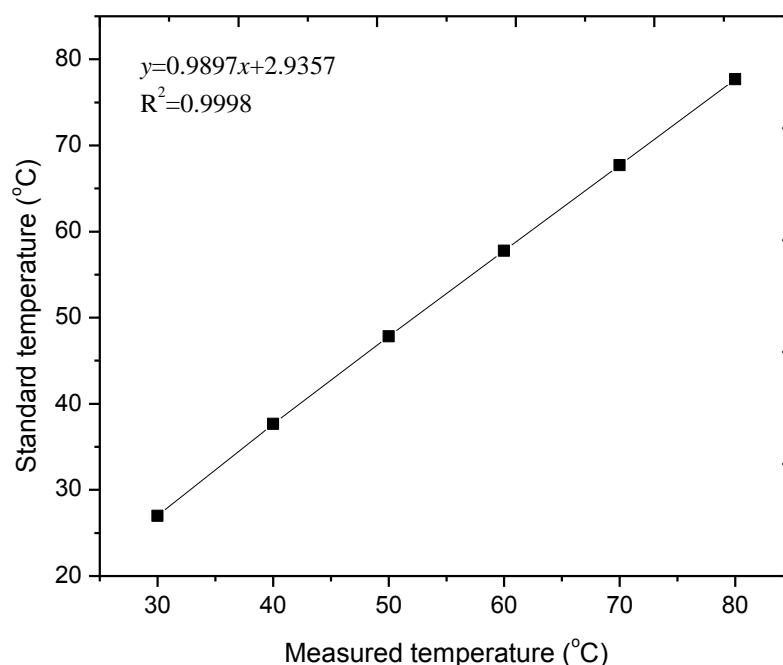


Figure 4.3 The relationship between the measured temperature by the thermocouples and the standard temperature of the calibrator. Linear fitting curve of the data points provides a calibrated function for converting the temperatures measured by thermocouple to the real temperatures.

As shown in Figure 4.2, three thermocouples (TC1, TC2, TC3) which had been carefully calibrated were utilized to measure the thermal profile of the deposition channel in axial direction. Various thermal environments can be achieved by adjusting the temperature of water bath (40.0 °C – 80.0 °C) with constant flow rate of hot water in heating channels (6 ml/min). Table 4.1 illustrates that fairly uniform thermal field in axial direction has been achieved in the deposition channel by channelling the counter flow of hot water. The maximum standard deviation for three thermocouples was only 0.2 °C when the temperature of water bath was set at 80 °C.

Table 4.1 Temperatures measured in microchannel with constant flow rate of hot water (6 ml/min)

Water bath temperature (°C)	Temperature in the deposition channel (°C)		
	TC1	TC2	TC3
40.0	36.5	36.6	36.4
50.0	44.2	44.3	44.1
60.0	51.7	51.8	51.5
70.0	58.8	58.8	58.5
80.0	66.3	66.1	65.9

To evaluate the possible effect of temperature gradient induced thermophoresis on particle deposition in the present study, a two-dimensional numerical simulation of temperature distributions in the deposition channel was performed by using COMSOL Multiphysics (V4.2). In the simulation, the wall temperature of two heating channels was set to be the maximum measured temperature at 66.1 °C corresponding to the water bath temperature at 80 °C, and a convection boundary with a heat transfer coefficient of 10 W/m² K was applied on the outer surfaces of the deposition channel (Incropera and Dewitt 2002). The temperature profile along the centerline of the deposition channel is shown in Figure 4.4. It is found that the average temperature gradient is only 353.7 K/m along the vertical direction of the deposition channel, based on which the thermophoretic force (\bar{F}_T in Eq. (3.54)) can be estimated to be four orders less than the gravity force (\bar{F}_G in Eq. (3.44)) and colloidal forces (electric double layer force \bar{F}_{edl} in Eq. (3.25) and van der Waals force \bar{F}_{vdw} in Eq. (3.37)) in the vicinity of the channel surface. It indicates that the thermophoresis effect is negligible. Thus, the themophoretic force is neglected in the modelling for the study on bulk temperature in this research.

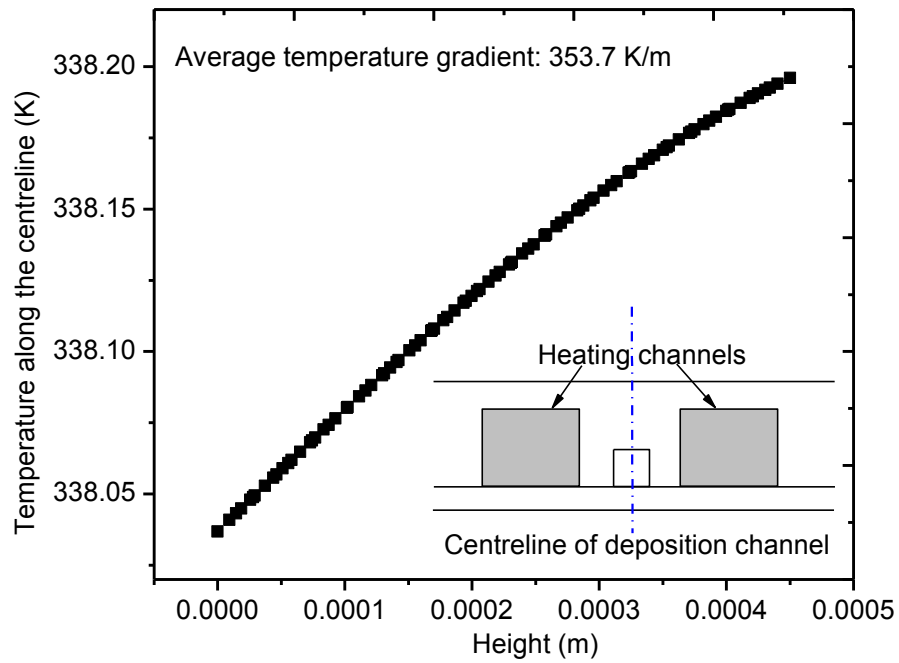


Figure 4.4 Temperature profile along the 81xperiment of the deposition channel. Data are obtained by a two-dimensional simulation with boundary conditions. Inset: wall temperatures of heating channels of 339.25 K and heat convection between the chip and the ambient air of $h = 10 \text{ W/m}^2 \text{ K}$.

4.1.2 EXPERIMENTAL PROCEDURES

For the experimental studies on the bulk temperature with microfluidic system, the general procedures are listed below:

- 1) The microchannel chip was cleaned in with DI water ultrasonic cleaner for about 2 hours.
- 2) A fine particle suspension of polystyrene beads (100 μl , 930 nm in diameter, 1% solids) was prepared in DI water (50 ml). The sample fluid was homogenized by using ultrasonic bath for about half an hour before loading.
- 3) The temperature of water bath and flow rate of hot water were set to the designed values via the control panels of water bath and syringe pump, respectively. The laser for activating fluorescent particles was turned on to warm up for about 10 minutes.
- 4) For experiments on effects of bulk temperature and electrolyte concentration in a stationary sample fluid, one deposition channel was filled with sample fluids, and the

two opening of the deposition channel were sealed firmly to avoid pressure disturbance from environment. To supply the counter flow of hot water, two heating channels were connected to the water bath and syringe pumps by using silicone tube. Two syringe pumps were implemented to suck the hot water from the water bath to the two heating channels.

- 5) The captured area of interest ($597 \times 436 \mu\text{m}^2$) was fixed at the centre point of the deposition channel in the longitude direction. The CCD camera was switched on and its exposure time was set as 1s.
- 6) Sequences of image were taken with a time interval of five minutes. At the first 15 minutes, images were taken without supplying hot water in order to provide a reference result at room temperature. Thereafter, hot water was continuously supplied to the heating channel with the constant flow rate.
- 7) After 90 minutes, the experiment was stopped, and all the images were stored in computer for analysis. A software “Image Pro Plus” was employed to process the images of particle deposition by counting the number of deposited particles within the area of interest. Figure 4.5 shows typical particle images captured at different times when the temperature of hot water was maintained at 80 °C. Since the focus plane is on the bottom surface of the deposition channel, only particles within the near-wall region can be seen clearly as black dots while particles far away from the bottom surface would be out of focus. It is worth noting that the experiment approach mentioned above enables a more sensitive measurement for deposition rates compared to the approach of measuring deposition mass on surface, especially for unfavourable deposition conditions.

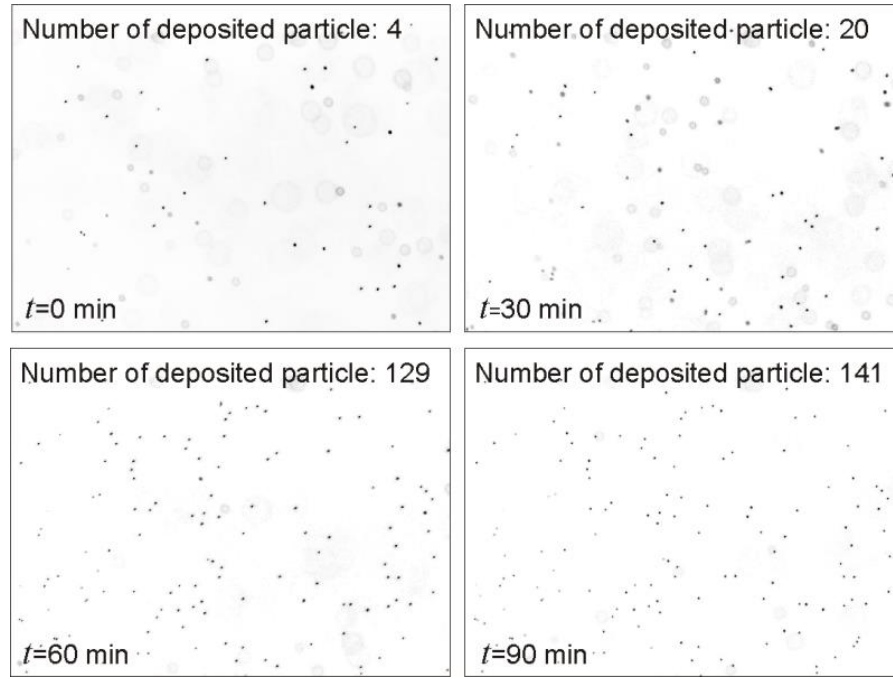


Figure 4.5 Videomicroscopic images of 0.93 μm polystyrene particles captured using 15X objective lens under the heating condition of 339.25 K solution temperature at 0min, 30min, 60min and 90min. Particles are shown as black dots.

To investigate the thermal effect, the temperature of water bath was adjusted from 50 °C to 80 °C. Sample fluids were diluted again in DI water with volume ratio of 1 to 1. To investigate the electrolyte effect, the temperature of water bath was maintained at 60 °C. Sample fluids were mixed with *NaCl* solution (1×10^{-2} M, 1×10^{-3} M, 1×10^{-4} M) with volume ratio of 1 to 1.

After completing the deposition measurements for a given system setting, the measured particle deposition flux J_{exp} onto the bottom surface of the deposition channel can be determined from the counted number of deposited particles onto the deposition area in the period of test time (Δt), as shown in Eq. (4.1). N is the number of deposited particles, and S is the area of observation region.

$$J_{\text{exp}} = \frac{N(t + \Delta t) - N(t)}{S \Delta t} \quad (4.1)$$

The static dimensionless deposition rate of experiment, Sherwood number (Sh_{exp}), can be calculated as

$$\text{Sh}_{\text{exp}} = \frac{J_{\text{exp}}}{D_{\infty} n_{\infty,p} / a_p} \quad (4.2)$$

where $n_{\infty,p}$ is the particle concentration of the bulk fluid, a_p represents the average particle radius of the sample, and D_{∞} denotes the diffusion coefficient in bulk fluid which can be determined by the Stokes-Einstein equation

$$D_{\infty} = \frac{k_B T_0}{a_p} \left(\frac{1}{6\pi\mu} \right) \quad (4.3)$$

where k_B is the Boltzmann constant and μ is the viscosity of water at the reference temperature $T_0 = 293.15$ K.

4.1.3 UNCERTAINTY ANALYSIS IN MEASUREMENTS

In this study, the experimental Sherwood number (Sh_{exp}) is defined by Eq. (4.2). Replacing the measured particle deposition flux J_{exp} by Eq. (4.1), the Sherwood number can be rewritten as

$$\text{Sh}_{\text{exp}} = \frac{N(t + \Delta t) - N(t)}{S \Delta t} \frac{a_p}{D_{\infty} n_{\infty,p}} = \frac{\Delta N}{S \Delta t} \frac{a_p}{D_{\infty} n_{\infty,p}}. \quad (4.4)$$

Because $\frac{a_p}{D_{\infty} n_{\infty,p}}$ only depends on physical properties of the sample solution, it can be treated

as constant through the experiments. The relative uncertainty of the experimental Sherwood number can be calculated by using error transfer equation

$$\frac{\delta \text{Sh}_{\text{exp}}}{\text{Sh}_{\text{exp}}} = \sqrt{\left(\frac{\partial \text{Sh}}{\partial \Delta N} \frac{\delta \Delta N}{\Delta N} \right)^2 + \left(\frac{\partial \text{Sh}}{\partial S} \frac{\delta S}{S} \right)^2 + \left(\frac{\partial \text{Sh}}{\partial \Delta t} \frac{\delta \Delta t}{\Delta t} \right)^2} \quad (4.5)$$

where the first term at the right hand side of Eq. (4.5) is the uncertainty of the measured number of deposited particles (ΔN), the second term refers to the uncertainty of the area of observed region (S), and the last term indicates the uncertainty of the measured test duration (Δt). The accuracy of measuring the area of observed region and duration of experiment are about $1 \mu\text{m}^2$ and 1 s, respectively. The measurement uncertainties of the area of the observed region and

experiment duration are about 0.000384% and 0.019%. The uncertainty of the number of deposited particles is estimated based on the standard deviation of the counted number of deposited particles for all of the repeated tests, which gives an uncertainty within 20%. Overall, the relative uncertainty for the experimental Sherwood number measured in the present study can be approximated by using is Eq. (4.5), giving a value of 20%. In addition, the accuracy of the temperature measurement is about ± 0.5 °C in this study according to the manual of the micro-thermocouples (TTC-40-K1, 0.08 mm in diameter).

4.2 THEORETICAL MODELLING

In Chapter 3, the one-dimensional mass transport equation with consideration of thermal effect is derived on the basis of the modified DLVO theory for the particle deposition in microchannels at elevated temperatures. This model will be employed in this chapter to analyse the effect of bulk temperature on the particle deposition in microchannels. For particles suspended in a stationary solution at elevated temperatures, the forces exerted on the particles consist of electric double layer force (shown in Eq. 3.25), van der Waals force (shown in Eq. 3.37) and gravity (shown in Eq. 3.44).

The dimensionless particle number concentration (\bar{n}) is computed by solving the one-dimensional mass transport equation shown in Eq. (3.20) with the two widely used boundary conditions shown in Eqs. (3.21-3.22). In this study, a software Comsol Multiphysics (V.4.2) is adopted to numerically solve the mass transport equation with an iterative equation solver. Computational test were conducted to estimate the influence of H_0 on the numerical results. It was found that the numerical results are not affected significantly by the specific value of the integration limits as long as $H_0 \leq 0.005$ and $H_\infty \geq 20$. Thus, the lower and upper integration limits are taken as $H_0 = 0.001$ and $H_\infty = 100$, respectively.

The numerical solution of the dimensionless particle deposition rate onto the channel surface ($H = H_0$) is calculated as

$$\text{Sh}_{num} = \frac{j_0}{(D_\infty n_\infty / a_p)} = -f_1(H_0) \left(\frac{d\bar{n}}{dH} \right)_{H=H_0} \quad (4.6)$$

where \bar{n} is the particle number concentration distribution obtained numerically and $f_1(H)$ is the universal hydrodynamic correction coefficient.

Table 4.2 shows the parameters for calculating the dimensionless concentration (\bar{n}) and Sherwood number (Sh_{num}) for different experimental conditions. The values of dimensionless parameters (Ad , Dl , Da , τ) are computed based on the material properties (ρ , μ) and the empirical correlations from the available literatures (Maidment 1993, Knox and McCormack 1994, IAPWS 1997a, b). Details can be found in Section 3.4.

Table 4.2 Values of the parameters used for modelling at different temperatures

T (K)	Ad	Dl	Da	τ	ρ_{water} (kg/m ³)	μ (x 10 ⁻³ Pa s)
297.25	0.383	50.929	2.449	3.616	997.075	0.864
317.35	0.396	40.049	2.449	4.487	990.576	0.610
324.65	0.401	36.437	2.449	4.821	987.376	0.540
331.75	0.407	33.177	2.449	5.145	983.928	0.483
339.25	0.413	29.987	2.449	5.486	979.948	0.431

Finally, the numerical results of the dimensionless concentration (\bar{n}) and Sherwood number (Sh) will be used to compare with the experimental results, and gain more insights of the parametric effects of the experimental variables on the particle deposition in microchannels in the following sections.

The total interaction potential (\bar{V} shown in Eq. (3.18)) will be plotted versus the dimensionless separation distance ($H = h/a_p$), also known as the interaction potential curve of particle deposition. This interaction potential curve will be implemented to analyse the experimental results in the following sections.

4.3 RESULTS AND DISCUSSION

In this section, the parametric effects on particle deposition for a stationary solution are discussed both experimentally and numerically, including the bulk solution temperature and the electrolyte concentration. For each case study, only one parameter is adjusted in the experiment while other parameters are kept as constants.

4.3.1 EFFECT OF SOLUTION TEMPERATURE

Bulk solution temperature

The effect of solution temperature on particle deposition is studied by regulating the temperature of a stationary sample fluid in the deposition channel from 297.25 K to 339.25 K. Figure 4.6 shows the number of deposited particles per unit area increases gradually with the time. During the first 15 minutes, the number of deposited particles does not increase significantly because of no heating applied within this period. Once hot water is supplied to the heating channels, the number of deposited particles per unit area increases rapidly (compared to the room temperature case, 297.25K). After 90 minutes, the number of deposited particles per unit area at the highest solution temperature (339.25 K) is about four times of that at room temperature (297.25 K), and double that at the solution temperature at 317.35 K.

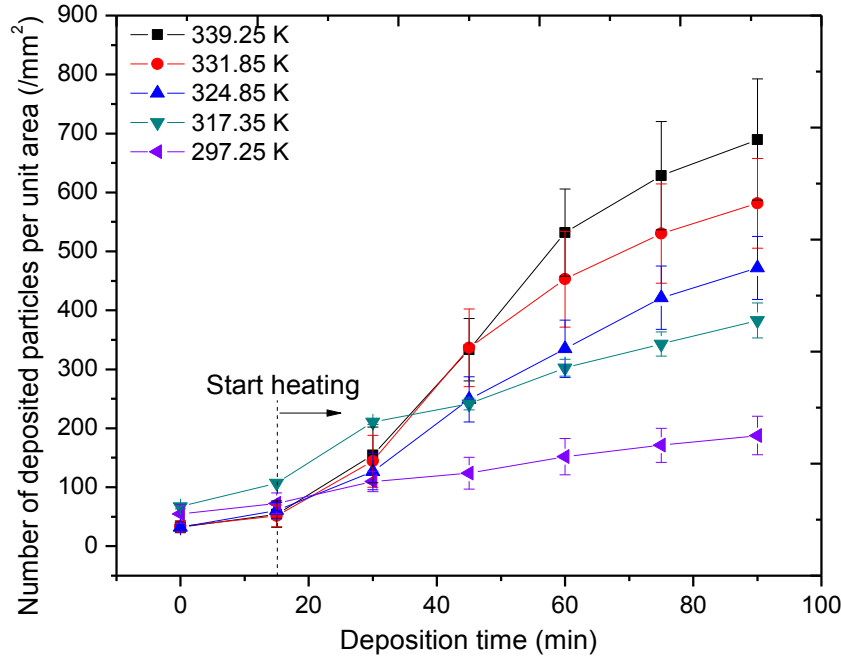


Figure 4.6 Number of deposited particles per unit area versus deposition time for five different solution temperatures at 297.25 K, 317.35 K, 324.85 K, 331.85 K and 339.25 K. Data are for fluorescent polystyrene particles dispersed in DI water (stationary fluid). The solution temperature is determined by an average reading of three thermocouples. Hot water is supplied through the heating channels at 15 min after starting each experiment.

The Sherwood numbers from the experiment (Sh_{exp}) and modelling (Sh_{num}) are plotted in Figure 4.7. It is seen that Sherwood number (Sh_{exp}) is monotonically increased with increasing the bulk temperature of sample solution. The Sherwood number is increased about 265%, from 0.0063 to 0.0230, when the solution temperature is elevated from room temperature (297.25 K) to 339.25 K. Since the zeta potentials of the polystyrene particle and PMMA channel surface are both negative, the observed increase of Sh_{exp} suggests that the attraction energy (van der Waals force and gravity) could increase but the repulsive energy (electric double layer force) could decrease by elevating the temperature of sample solution. Gravity could affect the particle transport process at long separation distances, and colloidal forces determine the deposition at the attachment step in the vicinity of wall. The increase of gravity with temperature could facilitate the transport of particles from bulk phase to the surface. In the near-wall region, more particles can deposit onto the channel surface because the attractive van der Waals force is increased and the repulsive electric double layer interaction is reduced with increasing the homogenous solution

temperature. Hence, the particle deposition is enhanced with increasing the solution temperature as observed in experiments.

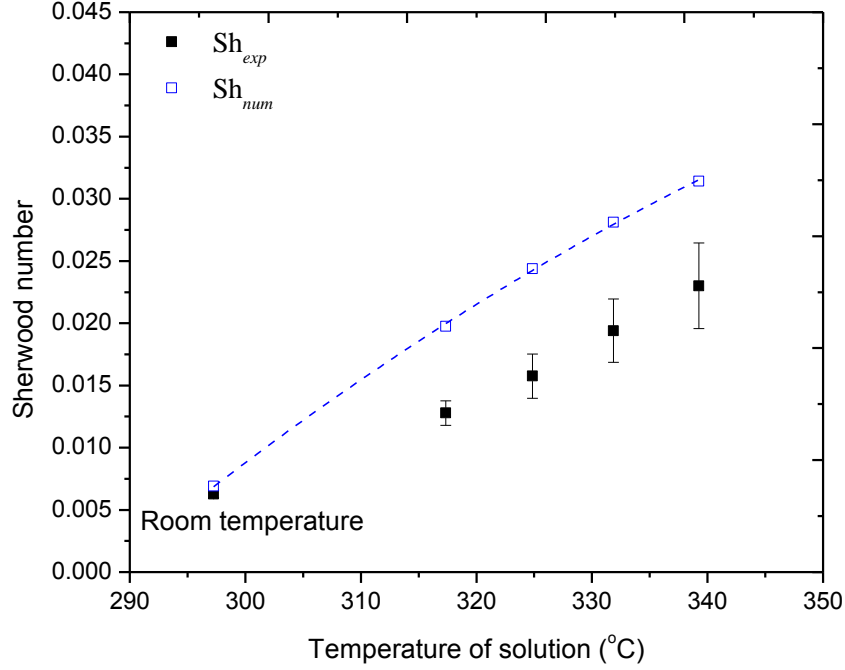


Figure 4.7 Dimensionless static deposition rate (Sherwood number) as a function of the temperature of solution at five different temperatures, 297.25 K, 317.35 K, 324.85 K, 331.85 K and 339.25 K. Solid squares (■) indicate the measured Sherwood number Sh_{exp} shown in Eq. (4.2) from experiments, and empty squares (□) show the calculated Sherwood number Sh_{num} by Eq. (4.6) from modelling. The dotted line shows the least-square fitting line. Data are for fluorescent polystyrene particles dispersed in DI water (stationary fluid).

The numerically calculated Sherwood number (Sh_{num}) based on the derived model are also presented in Figure 4.7. The values of numerical results are comparable in the same magnitude with those of experimental results. It is suggested the particle deposition in microchannel at elevated temperature is able to be described by the mass transport equation based on the modified DLVO theory. Besides, it is noted from Figure 4.7 that the numerical results of Sherwood number are relatively larger than the measured Sherwood numbers in experiments. The difference between the numerical results of Sh_{num} and the measured data Sh_{exp} is increasing with the solution temperature. This difference might be caused by some additional non-DLVO forces which are not included in the present modelling, for example hydrophobic interaction force between the hydrophobic surfaces of polystyrene particle and PMMA channel in aqueous medium. Another possible reason could be due to errors induced by the empirical correlations used in the model,

which may not precisely describe the variations of material properties with the solution temperature in this study, such as the temperature dependence of zeta potentials for the polystyrene particle and microchannel wall (shown in Eq. (3.31)). The physical mechanism of the temperature dependence of zeta potential has not been fully understood. As a result, errors may be caused for calculating the colloidal force by using these empirical correlations. The predicted results of Sherwood number could differ from the experimental results.

Interaction potential curve

In order to gain insight into the particle deposition process at elevated temperatures, the particle-wall interaction potential for different solution temperatures is calculated based on Eqs. (3.18). The particle-wall interaction potential \bar{V} is plotted versus the dimensionless separation distance H in Figure 4.8. Positive interaction potential indicates a repulsive condition whereas negative interaction potential represents the attraction one. Figure 4.8-a shows that the repulsive energy barrier is considerably reduced with increasing the solution temperature. It can be seen clearly that the energy barrier at 339.25 K is reduced about 43% compared with the case at 297.25 K in Figure 4.8-b. In other words, elevated solution temperatures provide a favourable condition for the particle deposition, because more particles can easily overcome the energy barrier and lead to deposition at the primary energy minimum (PEM). Consequently, the deposition rate of particles should be enhanced with increasing the solution temperature consequently as shown in Figure 4.7.

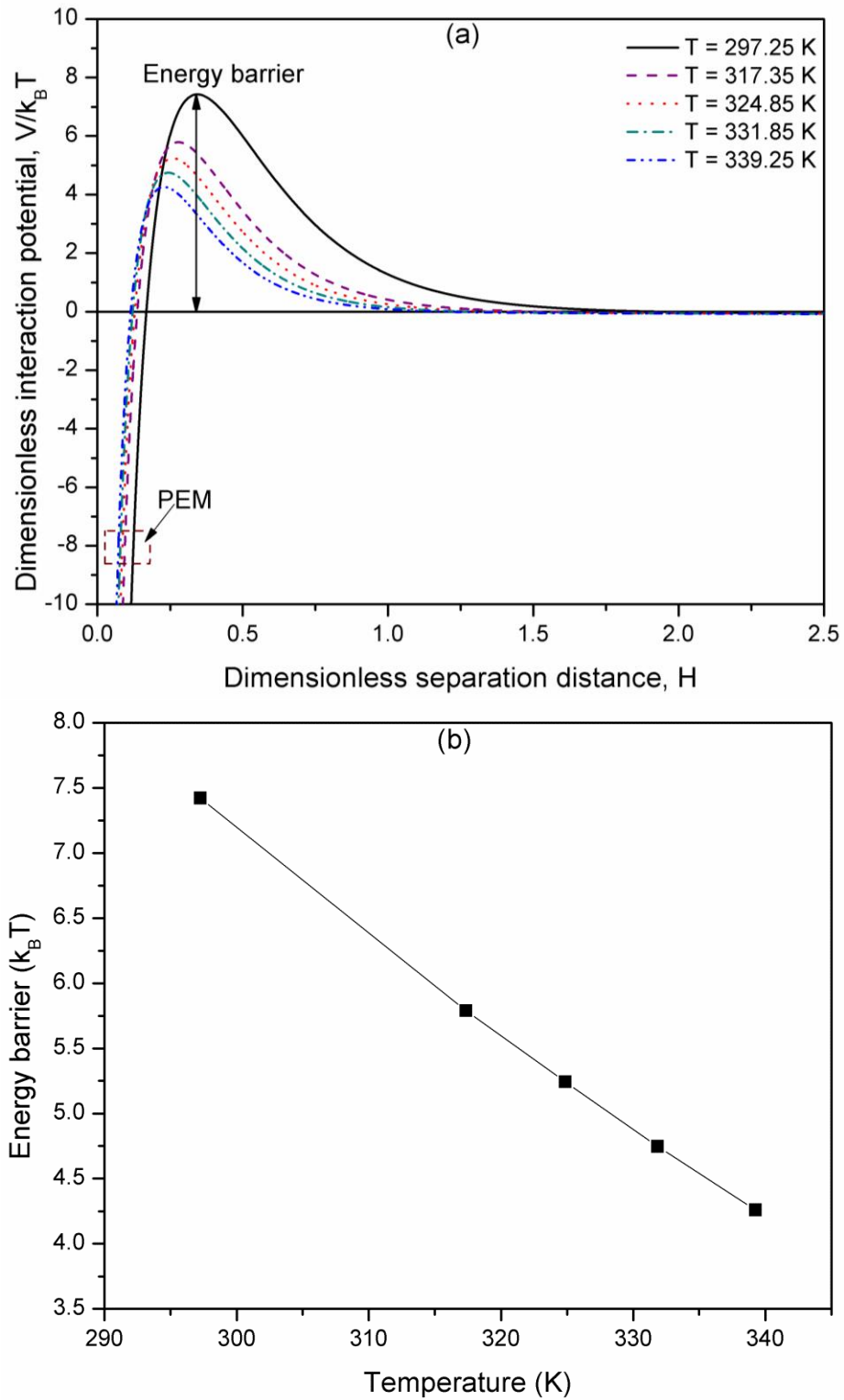


Figure 4.8 (a) Dimensionless particle-microchannel interaction potential \bar{V} versus the dimensionless separation distance H for different bulk solution temperatures. (b) The energy barrier as a function of the solution temperature in a stationary fluid. Data are calculated based on Eq. (3.18) for fluorescent polystyrene particles dispersed in stationary DI water. The dotted square PEM indicates the primary energy minimum (PEM) region.

Particle concentration distribution

The distribution of dimensionless particle concentration (\bar{n}) is obtained by solving Eqs. (3.20-3.22) and is plotted versus H in Figure 4.9. Figure 4.9-a shows that the dimensionless particle concentration is continuously increased from zero in the vicinity of the solid surface ($H = H_0$) to a maximum value, and then gradually reduces to unity in the bulk phase ($H = H_\infty$) as specified by the boundary conditions. Particularly, a depletion zone can be observed where H is smaller than 0.3, in which the particle concentration remains zero as shown in Figure 4.9-b. Within the depletion zone, the attractive potential (van der Waals force) is much larger than the repulsive potential (electric double layer force). Particles are irreversibly attached onto the microchannel surface. In other words, the particles would be trapped into the primary energy minimum (PEM) region. As the separation distance is increased to $H > 0.3$, the repulsive EDL force is increased to overtake the attractive vdW force. As a result, the dimensionless concentrations are increased rapidly in the range of $0.3 < H < 2$. Moreover, it is noted that a maximum value of accumulated particle concentration exists for each solution temperature. It is because particles tend to accumulate in the vicinity of channel surface before they can overcome the repulsive energy barrier. The value of maximum accumulated particle concentration is reduced with increasing the solution temperature. It can be understood by using the interaction potential curves shown in Figure 4.8. Because the repulsive energy barrier for low temperature is higher than that for high temperature, particles have lower chance to overcome the energy barrier at low temperatures compared to the high temperature cases. Therefore, the concentration of accumulated particle before the energy barrier for low temperature is larger than that for high temperature.

It can be concluded that the particle deposition is strongly affected by the bulk temperature of sample fluid which determines the magnitude of repulsive energy barrier as well as the particle concentration distribution. The repulsive energy barrier is remarkably decreased with increasing the solution temperature in DI water as shown in Figure 4.8-b. More particles would deposit onto the solid surface with higher solution temperature.

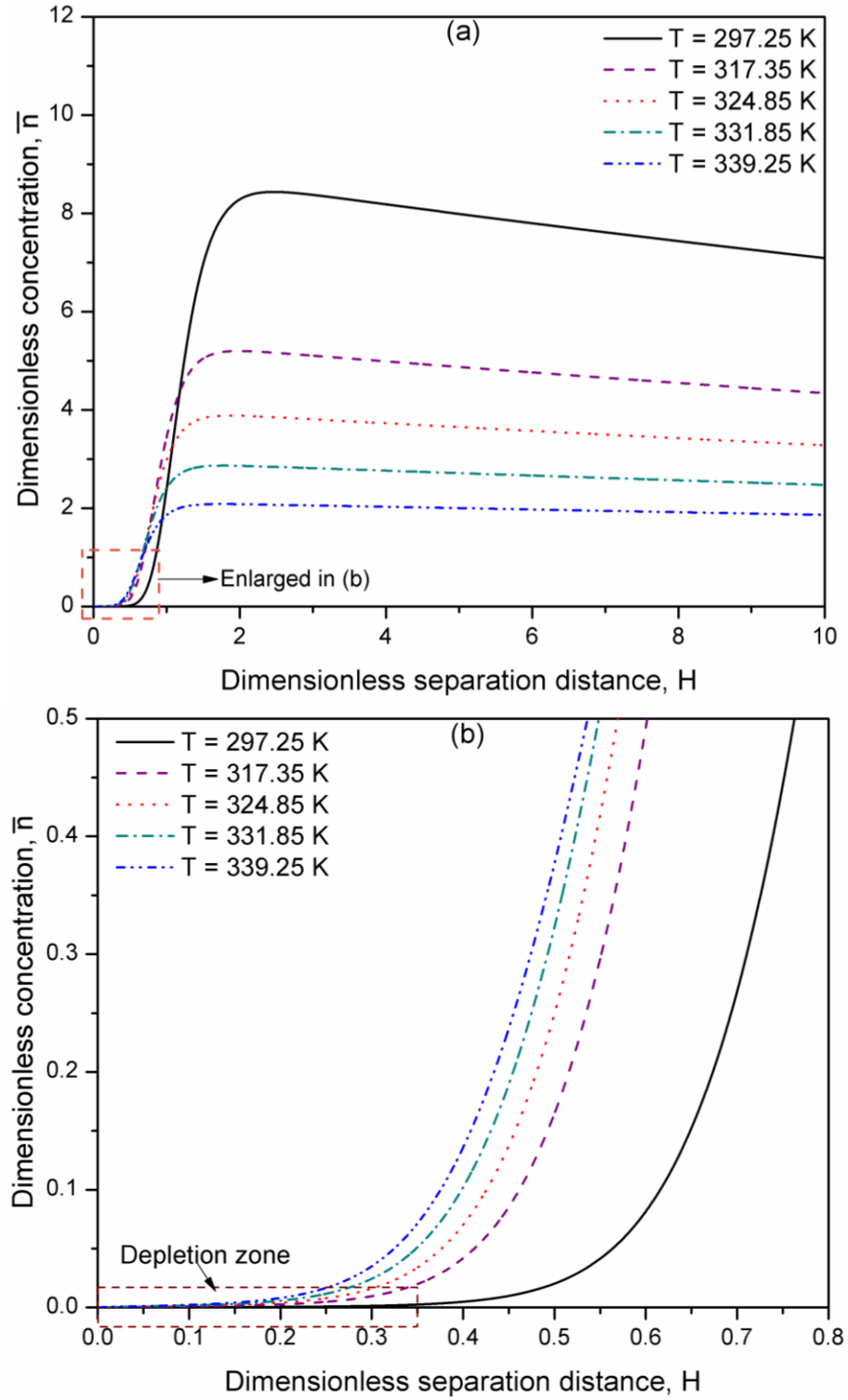


Figure 4.9 (a) Computational dimensionless particle concentration \bar{n} versus the dimensionless separation distance H for different bulk solution temperatures. (b) The dimensionless particle concentration in the vicinity of the microchannel surface ($H = 0 \sim 0.8$). The depletion zone is shrunk with increasing temperature. Data are calculated based on Eq. (3.20) for fluorescent polystyrene particles dispersed in stationary DI water.

4.3.2 EFFECT OF ELECTROLYTE CONCENTRATION AT ELEVATED TEMPERATURES

Electrolyte concentration

In this study, *NaCl* solutions of various molar concentrations were utilized to adjust the electrolyte concentration (or ionic strength) of the stationary sample fluid (DI water, 0.00005 M, 0.0005 M and 0.005 M), with a fixed temperature of sample solution at 324.85 K. The variations of the number of deposited particles per unit area with deposition time are plotted in Figure 4.10 for four samples with different electrolyte concentrations. It can be observed that the number of deposited particles per unit area are gradually increased with the deposition time. More particles are observed to deposit onto the channel surface with a higher electrolyte concentration than that with the low electrolyte concentration after hot water is supplied to the heating channel in 15 minutes.

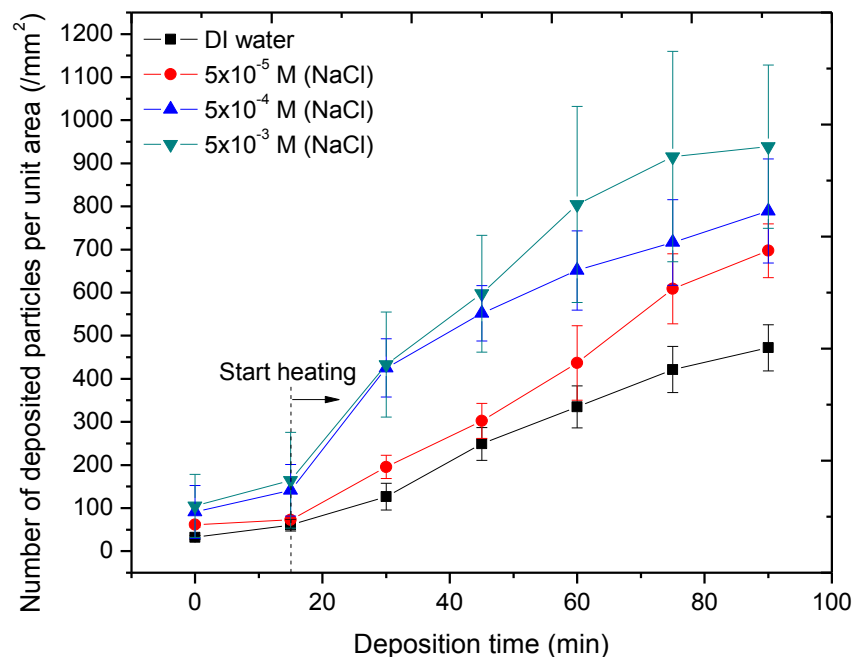


Figure 4.10 Number of deposited particles per unit area versus deposition time at different electrolyte concentrations with fixed solution temperature (324.85 K). Data are for fluorescent polystyrene particles dispersed in DI water and NaCl solutions (Stationary fluid). Hot water is supplied through the heating channels at 15 min after starting each experiment.

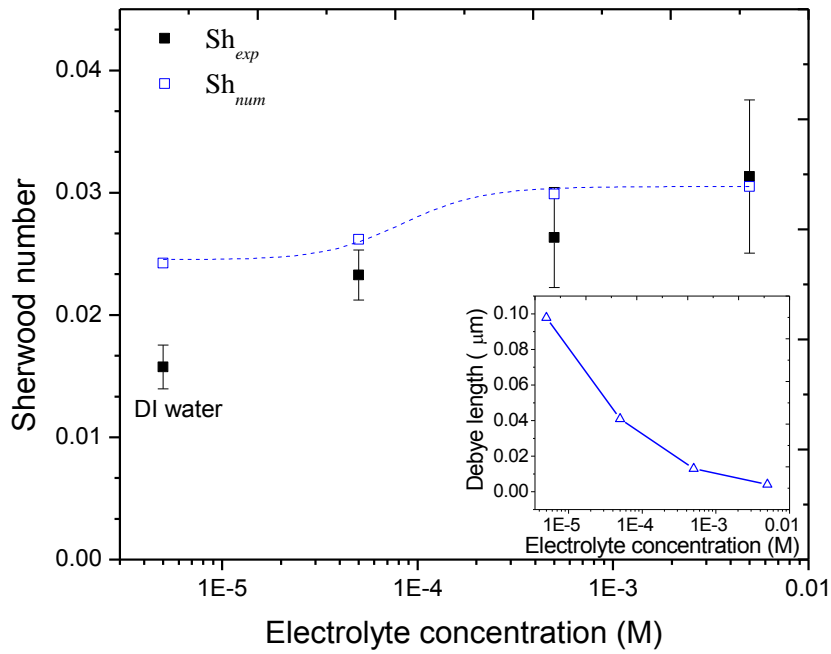


Figure 4.11 Dimensionless static deposition rate (Sherwood number) versus the electrolyte concentration for DI water, 5×10^{-5} M, 5×10^{-4} M and 5×10^{-3} M. Solid squares (■) indicate the measured Sherwood number Sh_{exp} shown in Eq. (4.2) from experiments, and empty squares (□) show the calculated Sherwood number Sh_{num} shown in Eq. (4.6) from modelling. The dotted line shows the least-square fitting line. Inset shows the thickness of electric double layer (Debye length) as a function of the electrolyte concentration. Data are for fluorescent polystyrene particles dispersed in DI water and *NaCl* solutions (stationary fluid). The solution temperature is kept at 324.85 K.

Figure 4.11 summarises the experimental results (Sh_{exp}) and numerical results (Sh_{num}) for the dimensionless static deposition rate versus concentration of the electrolyte concentration of the sample fluid. Both experimentally measured and numerically calculated results show that the Sherwood number is increased appreciably with increasing the electrolyte concentration. The Sherwood number (Sh_{exp}) for 5×10^{-3} M is doubled from 0.015 for DI water to 0.031 in experiment. Such enhancement of particle deposition could be due to the strong neutralization effect of the electrolyte on the zeta potentials of the particle and channel surface. The net surface charge density of particle could be reduced because of absorbing the counterion (Na^+) onto the particle surface. As such, the magnitudes of the zeta potentials are reduced with the electrolyte concentration. Besides, the Debye length (EDL thickness) is reduced from 97 nm to 4 nm with increasing the electrolyte concentration to 5×10^{-3} M as seen in the inset of Figure 4.11. The compressed EDL thickness further attenuates the EDL interaction, and contributes to the enhanced particle deposition. The repulsive EDL interaction between the particle and channel

wall becomes weaker with increasing electrolyte concentration when the thermal environment is remain unchanged. Thus, the particles have higher chances to overcome the energy barrier and deposit onto the channel surface.

Besides, the numerical results (Sh_{num}) generally agree with the experimental results (Sh_{exp}) in the same magnitude for all the electrolyte concentrations, though the numerical results of Sherwood number at low electrolyte concentration are larger than the measured Sh values in experiments. The difference between Sh_{num} and Sh_{exp} might be caused by the empirical correlations adopted from literatures. These correlations may not accurately predict the variations of material properties with the electrolyte concentration in this study, such as the dependence of zeta potentials on electrolyte concentration (Eq. (3.32)). As a result, the possible errors of calculating colloidal forces could affect the predicted results of Sherwood number. Another possible reason could be due to some additional non-DLVO forces which are not included in the present modelling, such as hydrophobic interaction force. Moreover, it is noted that the calculated Sherwood number remains nearly unchanged with the electrolyte concentration beyond 5×10^{-4} M while the measured Sherwood number is still increased with the electrolyte concentration. This could be understood as follows. With relatively high electrolyte concentrations ($C \geq 5 \times 10^{-4}$ M) the zeta potentials of particle and channel surfaces and EDL thickness are reduced so appreciably that the repulsive EDL interaction is much weaker than the attractive vdW interaction. As a result, the repulsive energy barrier becomes negligible. The effect of EDL interaction becomes not as crucial as that at the low electrolyte concentration. Thus, the particle deposition rate does not change significantly with additional electrolyte because the dominant vdW interaction would not change noticeably by further increasing the electrolyte concentration. On the other hand, the increase of Sh_{exp} in experiments ($C \geq 5 \times 10^{-4}$ M) could be caused by the hydrophobic interaction between the hydrophobic surfaces of polystyrene particle and PMMA channel in aqueous medium. The hydrophobic interaction force may play an important role in the particle deposition when the electric double layer is tremendously compressed at higher electrolyte concentration, as shown in the inset of Figure 4.11. The repulsive electric double layer interaction is considerably

attenuated so that the additional attractive interaction from hydrophobic effect might enhance the particle deposition at the high electrolyte concentration.

Interaction potential curve

Based on the proposed model, the corresponding interaction potential (\bar{V}) is computed from Eq. (3.18), and is plotted versus the dimensionless separation distance H for various electrolyte concentrations in Figure 4.12. It can be clearly observed in Figure 4.12-b that the energy barrier for particle deposition decreased with increasing the electrolyte concentration. Figure 4.12-a shows that the energy barrier for particle deposition almost vanished when the electrolyte concentration is increased beyond 5×10^{-3} M. In this case, particles can easily overcome the energy barrier to deposit on the wall, leading to the highest particle deposition rate shown in Figure 4.11. As illustrated in Figure 4.12-a, the shape of the interaction potential curves is changed with the electrolyte concentration. For the DI water and low concentration case (5×10^{-5} M), there is only a repulsive energy barrier with primary energy minimum (PEM). For the medium electrolyte concentration case (5×10^{-4} M), the interaction potential curve is changed to be with both a moderate energy barrier and a shallow secondary energy minimum (SEM). For the high electrolyte concentration case (5×10^{-3} M), no noticeable energy barrier can be observed. The interaction potential is continuously decreased when the separation distance is reduced. Besides, the position of energy barrier is shifted toward a shorter distance from the channel surface by increasing the electrolyte concentration.

It can be concluded that the particle deposition at elevated temperature is strongly affected by the electrolyte concentration of sample fluid which determines the magnitude of repulsive energy barrier as well as the particle concentration distribution. The repulsive energy barrier is remarkably decreased with increasing the electrolyte concentration for a fixed elevated temperature as shown in Figure 4.12-b. More particles would deposit onto the solid surface with higher electrolyte concentration.

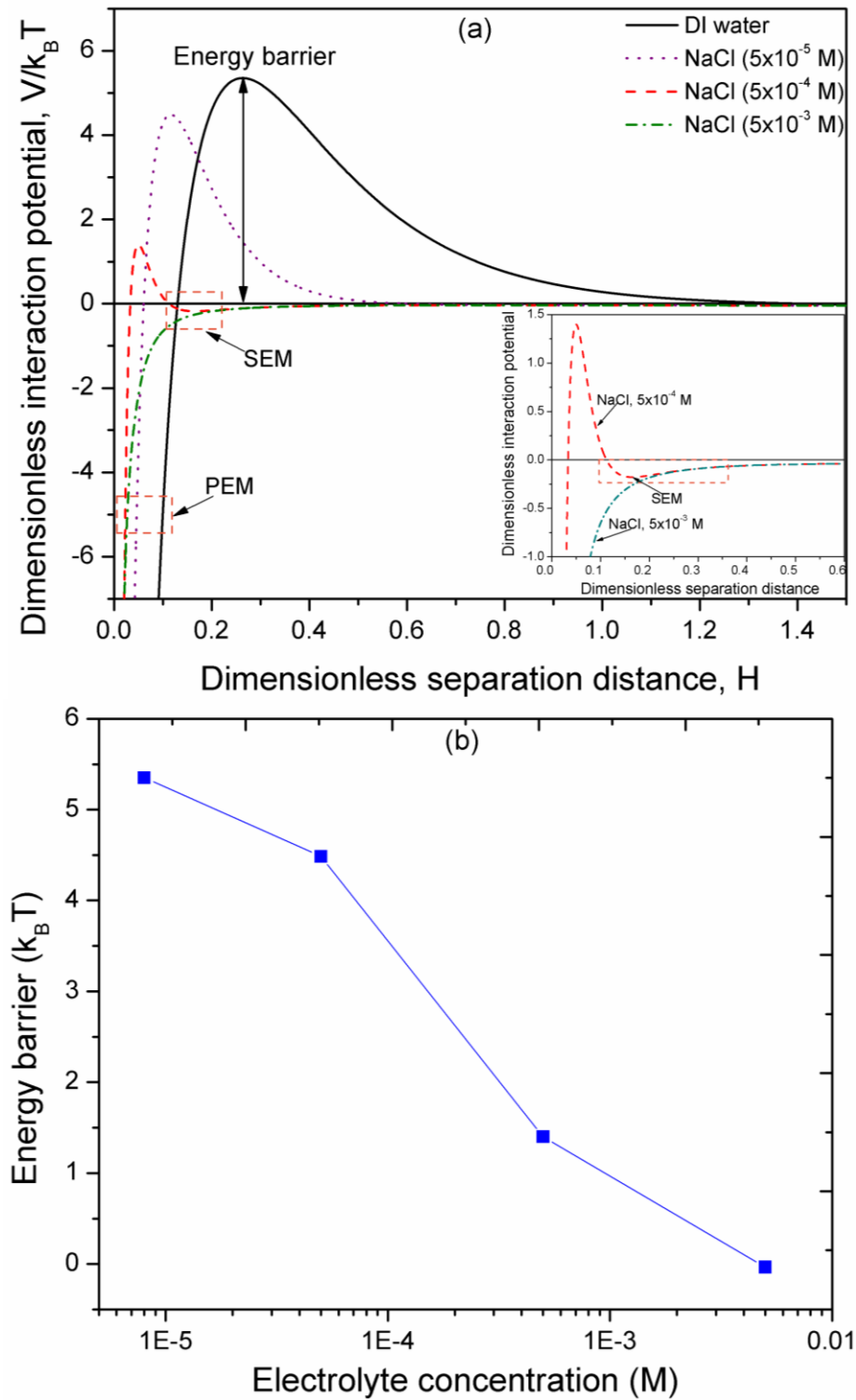


Figure 4.12 (a) Dimensionless particle-microchannel interaction potential \bar{V} versus the dimensionless separation distance H for DI water and *NaCl* solutions (5×10^{-5} M, 5×10^{-4} M and 5×10^{-3} M). (b) The energy barrier as a function of the electrolyte concentration in a stationary fluid. Data are calculated based on Eq. (3.18) for fluorescent polystyrene particles dispersed in DI water and *NaCl* solution (stationary fluid). The solution temperature is kept at 324.85 K. The dotted square SEM indicates the secondary energy minimum region, and the dotted square PEM indicates the primary energy minimum region.

4.4 SUMMARY

In this chapter, a microfluidic system is designed as an effective platform to study the particle deposition process in microchannels at elevated temperatures. This system provides well-controlled thermal environment and allows a direct observation for the dynamic process of particle deposition. To the best knowledge of the author, it is the first time to study the thermal effect (bulk temperature) on the particle deposition in microchannels. Parametric study has been conducted for important parameters, such as the solution temperature and the electrolyte concentration. Experimental results show that the particle deposition rate in microchannels is strongly dependent on the bulk solution temperature. For stationary solutions, the particle deposition rates are increased with increasing solution temperature. By keeping the bulk temperature of stationary solution as constant, results show that Sherwood number is monotonically increased by increasing the electrolyte concentration of particle solution.

The calculated particle deposition rates of the proposed model show a similar trend and is comparable with the experimental measurements, suggesting that the particle deposition process at elevated temperatures can be described by the model derived based on the modified DLVO theory. Based on the analysis of the numerical results, it is suggested that the bulk temperature determines the energy barrier impeding the particle attachment in the near-wall region, with a given electrolyte concentration and hydrodynamic conditions. The repulsive energy barrier is remarkably decreased with increasing the bulk solution temperature of sample fluids. The enhancement of particle deposition with increasing electrolyte concentration is due to the decreased energy barrier, which results from the compressed EDL thickness and reduced magnitude of EDL interaction at fixed solution temperatures.

Chapter 5

Effect of Temperature Gradient on Particle Deposition in Microchannels

In this chapter, a microfluidic system with a temperature-gradient microchip is designed and established to study the effect of temperature gradient on the dynamic process of particle deposition. A hydrodynamic flow is applied for the sample solution to establish a steady temperature gradient in the microchannel. To interpret the experimental results, the model derived based on the modified Derjaguin-Landau-Verwey-Overbeek (DLVO) theory in Chapter 3 is employed. Comparisons are conducted between the numerical results from the modelling and experimental results from measurements.

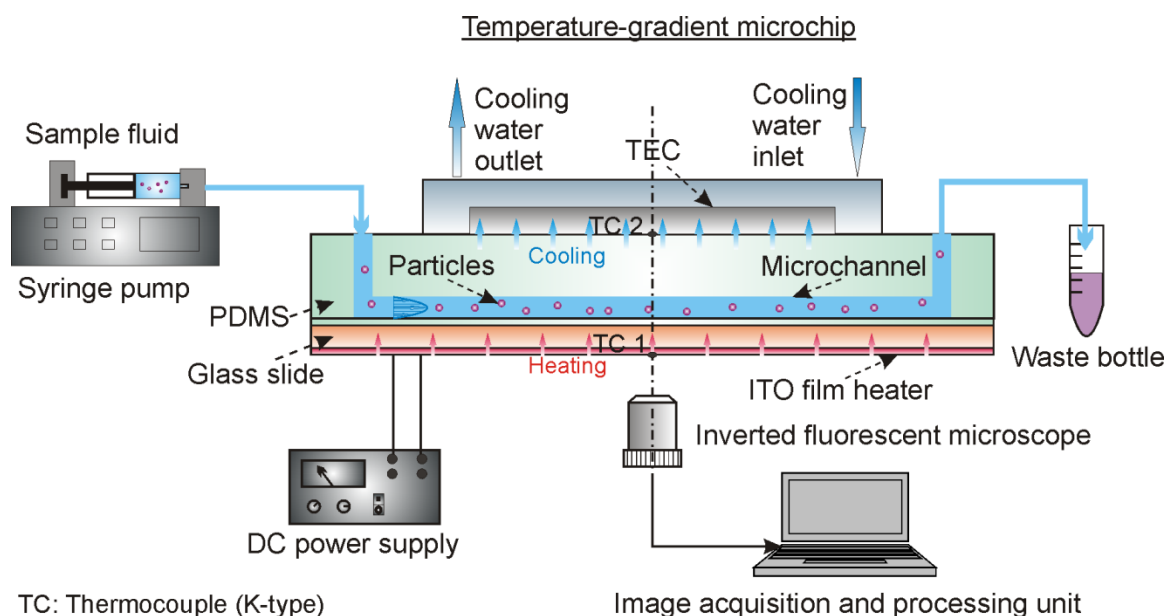
5.1 EXPERIMENT

Temperature gradient is another important parameter for the particulate deposition in microchannels besides the bulk temperature studied in Chapter 4. In this section, a microfluidic system is designed and fabricated in order to provide a wide range of controllable temperature gradients in the microchannel. The details of the experiment setup, temperature characterisation and experimental procedures are presented.

5.1.1 EXPERIMENTAL SETUP

Figure 5.1 illustrates the schematic of the experimental set-up used for the effect of temperature gradient on particle deposition. The microfluidic system consists of three parts: a temperature-gradient microchip, fluid supply parts and a data acquisition system. A syringe pump (KDS 200, USA) is implemented to supply sample solutions into the microchannel with a

constant flow rate. The temperature-gradient microchip is mounted on the stage of an inverted fluorescent microscope (Nikon TE-2000E). The objective lens (10 X) is targeted on the region where two thermocouples are installed to measure surface temperature of the microchip. A continuous DPSS laser (532 nm, 50 mW) is used to excite the fluorescent polystyrene particles in microchannels. The fluorescent emission signals of particles are recorded by a CCD monicolor camera with a time interval of 5 minutes consecutively for one hour. All the images are stored in an image acquisition and processing unit for counting the number of deposited particles after each test. A DC power supply is used to control the voltages and currents for the ITO film heater and TEC unit, respectively, in order to maintain the required temperature gradient in the microchip during the experiment.



TC: Thermocouple (K-type)

Figure 5.1 Schematic of the microfluidic system used for the direct observation of the particle deposition kinetics along the direction of applied temperature gradient. Two thermocouples (TC 1, TC 2) are used to measure the temperatures on the top surface of the PDMS block and bottom surface of the ITO coated glass slide (Figure is not drawn to scale).

5.1.1.1 MATERIALS

In this study, red fluorescent dyed polystyrene microparticles (R900, Duke Inc., USA) are used as sample to study the particle deposition under different temperature gradients. The particles have a density of 1.05 g/cm^3 and a diameter of $0.93 \text{ }\mu\text{m}$ (a_p) with a size variation of up to $0.03 \text{ }\mu\text{m}$. Particle samples are prepared by first diluting a particle

dispersion with a concentration (n_{∞}) of $5.6 \times 10^6/\text{ml}$ into de-ionized (DI) water, and then mixing with sodium chloride solutions (NaCl , Sigma-Aldrich, ACS reagent, $\geq 99.0\%$) for three different electrolyte concentrations, $5 \times 10^{-2} \text{ M}$, $5 \times 10^{-4} \text{ M}$, and DI water. The samples are homogenized by using an ultrasonic bath (Elmasonic E30H, Elma Ultrasonics) for half an hour before loading into a syringe for testing. The ambient temperature of the laboratory is recorded at $25.0 \pm 1.0 \text{ }^{\circ}\text{C}$ for all the experiments.

5.1.1.2 TEMPERATURE-GRADIENT MICROCHIP

The temperature-gradient microchip consists of three parts, as shown in Figure 5.2: a microchannel, a thin glass slide coated with indium tin oxide (ITO) film as a heater, and a thermoelectric cooler (TEC) unit. A temperature gradient can be established along the vertical direction (along y -axis in Figure 5.2) inside the microchannel, by cooling the top surface of the microchip with the TEC unit and heating the bottom surface with the ITO film heater.

The microchannel is fabricated with polydimethylsiloxane (PDMS) using standard soft lithography techniques. The PDMS channel is $50 \text{ }\mu\text{m}$ in height, $500 \text{ }\mu\text{m}$ in width and $42000 \text{ }\mu\text{m}$ in length. The PDMS monomer and the curing agent are fully mixed in a mass ratio of 10:1, and are pumped vacuum for 45 minutes in order to evacuate air bubbles remaining in the mixture. Thereafter, the mixture is poured onto the master mould made by SU8 on a silicon wafer. The wafer together with PDMS is placed in an oven for curing about 1 hour at 80°C . A thin layer of polymerized PDMS (1 mm in thickness) is peeled off from the mould. Two cylindrical openings with diameter of 0.75 mm are punched at both ends of the microchannel as the inlet and outlet for sample fluids.

For the ITO glass slide, a thin indium tin oxide film (200 nm in thickness) is deposited on one side of a glass slide (0.71 mm in thickness) as a heater for the microchip. Indium tin oxide is a solid mixture including $90\% \text{ In}_2\text{O}_3$ and $10\% \text{ SnO}_2$ by mass. There are three significant advantages to use ITO glass as heater for the present study. (1) Due to the electrical resistance of the ITO film (10 ohms/sq), it can easily generate heat by Joule heating when connecting into an electrical

circuit with a DC power supply. Heat dissipation rate can be well controlled by regulating the voltage and current applied on the ITO film. (2) The excellent optical transparency of ITO film allows a direct observation on the dynamic process of particle deposition onto the bottom surface of the microchannel along the direction of temperature gradient. For this study, a bottom view can be readily obtained with the help of an inverted Nikon microscope equipped with CCD camera. (3) Various geometric patterns and dimensions of ITO heaters can be precisely achieved by implementing the classic photolithography techniques according to different requirements. Details of protocol used in this study can be found in Appendix B. As illustrated in Figure 5.2, the ITO film on one side of the glass slide is etched to a rectangular heater with the same shape (42000 μm in length, 500 μm in width) as the PDMS microchannel, and the rest of ITO film is etched off. On the other side of the glass slide, a thin PDMS film was coated on the bare glass surface.

The PDMS block with microchannel structure is irreversibly bonded with the PDMS side of the treated ITO glass slide to form a closed microchannel, by using oxygen plasma of 35 Watt radio frequency (RF) power under vacuum condition. At last, the bonded microchip is put in the oven for 1 hour at 80 $^{\circ}\text{C}$ to reinforce the bonding strength between the PDMS block and the treated ITO glass slide.

The thermoelectric cooler (TEC) unit is mounted on top of the bonded microchip to provide a stable cold end on the top of the microchannel. The TEC unit is cooled by a water cooling system by circulating cool water from a water bath (15 $^{\circ}\text{C}$). By regulating the DC power supply, the temperatures of TEC unit and the ITO film heater can be readily adjusted. The temperature gradient can be well controlled in the microchannel along the same direction as the particle deposition. To monitor the thermal environment of the microchannel, two K-type thermocouples TC 1 and TC 2 (TTC-40-K1, 0.08 mm in diameter) are installed on the bottom surface of ITO film heater and on the top surface of the PDMS block. Thermal conductive silicon paste (OT201, Omega, USA) is applied in the gap between the TEC unit and the PDMS microchip to enhance the heat conduction.

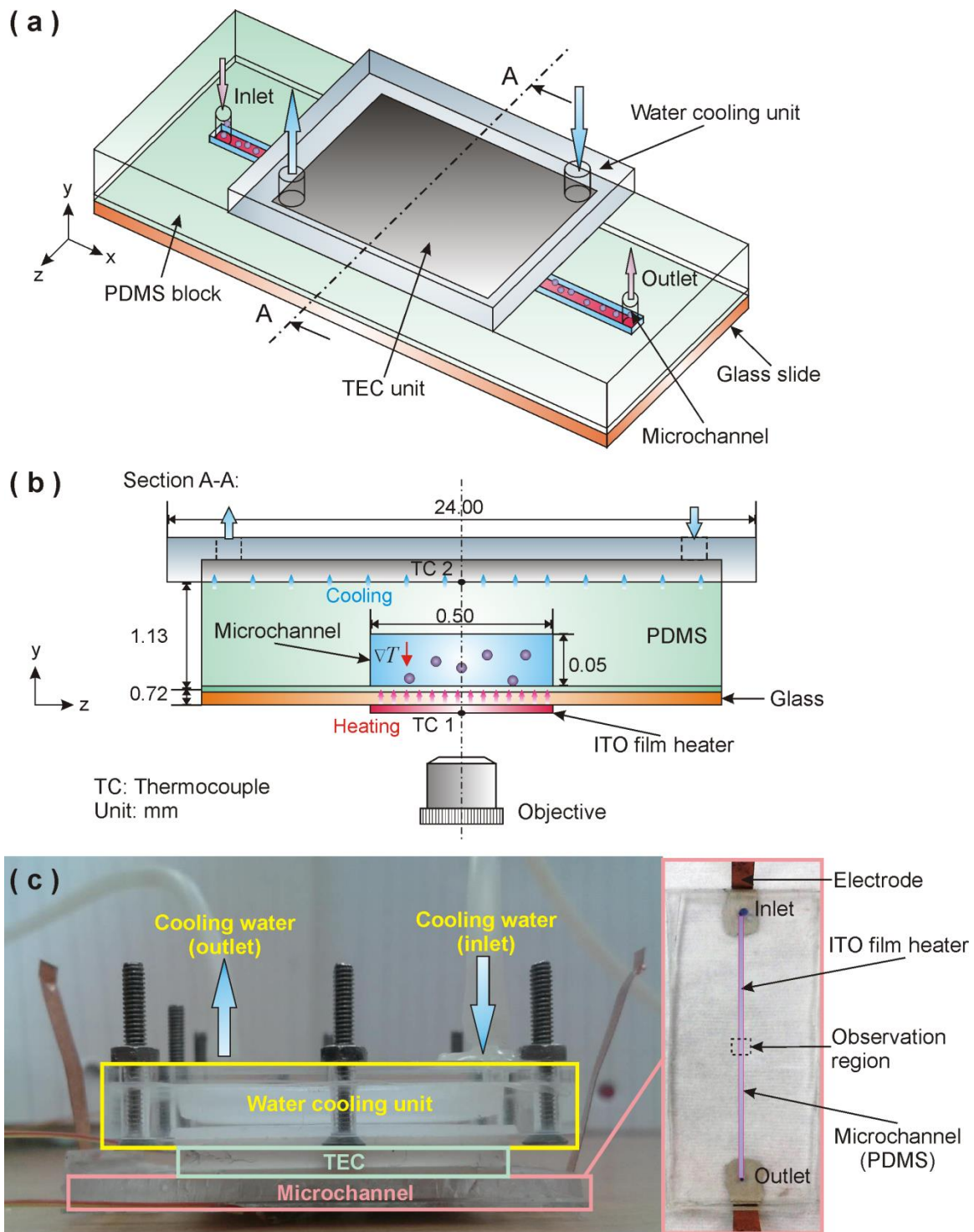


Figure 5.2 Schematic of the temperature-gradient microchip, consisting of the PDMS microchannel, the glass slide coated with ITO film and the TEC unit. Various temperature gradients can be achieved by cooling the top surface of the microchip with the TEC unit and heating the bottom surface with the ITO film heater. (a) Isometric view, (b) Cross section view, (c) A picture of the integrated temperature-gradient microchip and top view of the PDMS microchannel bonded with the ITO coated glass slide. (Figure is for not drawn to scale)

5.1.1.3 CHARACTERISATION OF THERMAL FIELD IN MICROCHANNEL

In order to obtain the temperature gradient for study on the particle deposition in the channel, two thermocouples are used for characterisation of the temperatures on the top surface of the PDMS block (T_{TEC} , °C) and the bottom surface of the ITO film heater (T_{ITO} , °C), as shown in Figure 5.2-b. The thermocouples are calibrated carefully before the commencement of the experiments. Details of the calibration can be found in Section 4.1.1.3.

Various thermal conditions can be achieved by adjusting the powers of the ITO film heater (P_{ITO}) and TEC unit (P_{TEC}) with a constant flow rate of sample flow rate (0.1 mL/h). The temperature field is considered to have reached steady state when the variation of thermocouple reading is no more than 0.5 °C over three minutes. The measured temperatures, T_{TEC} and T_{ITO} , are plotted versus the power inputs for the TEC and ITO heater in Figure 5.3. It illustrates that wide range of temperature difference ΔT (0 °C ~ 40 °C) are achieved in the vertical direction along which the particle deposition occurs. The maximum standard deviation for the readings of the two thermocouples is only 0.5 °C for one hour. A steady temperature gradient can be maintained in the microchannel throughout experiments.

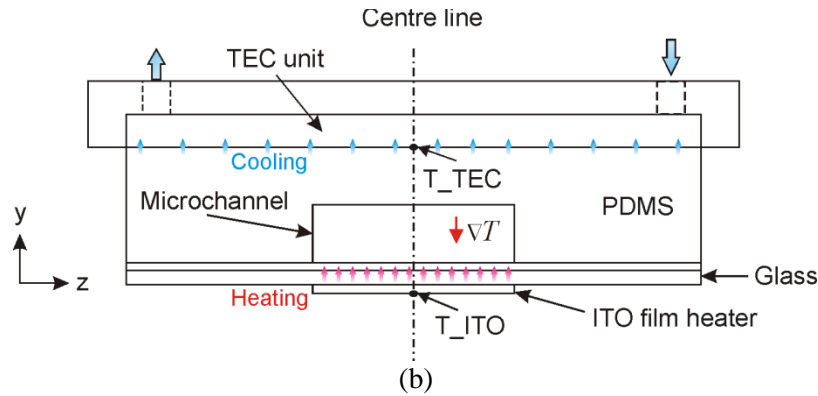
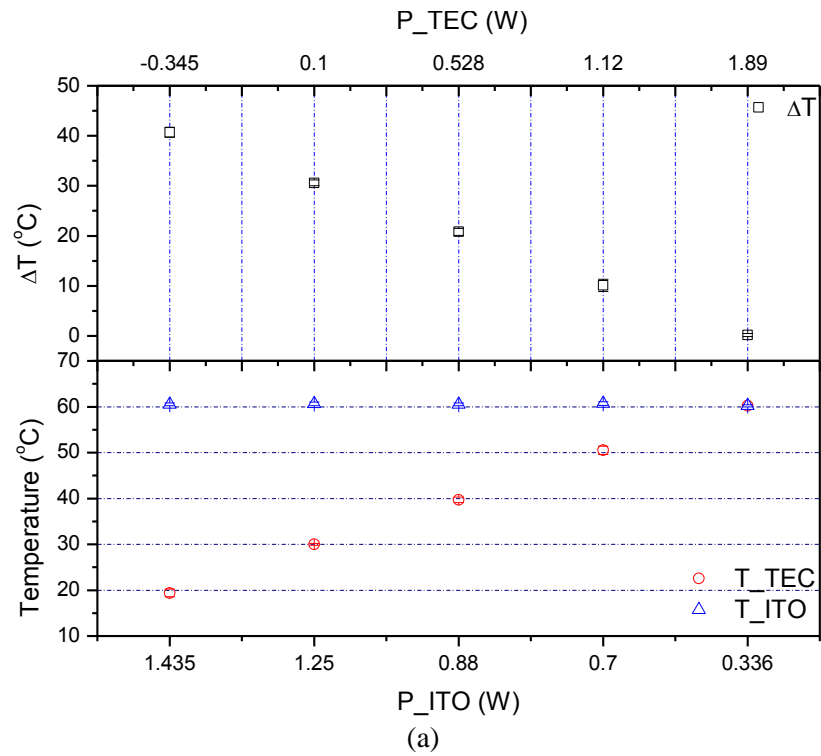


Figure 5.3 (a) Temperatures (T_{ITO} , T_{TEC}) and temperature differences (ΔT) measured by two thermocouples at various power inputs to TEC cooling unit (P_{TEC}) and ITO film heater (P_{ITO}). (b) Schematic of the temperature measurement in the experiment. The empty triangles indicate the temperature (T_{ITO}) measured on the bottom surface of the ITO film heater in Figure 5.2. The empty circles indicate the temperature (T_{TEC}) measured on the top surface of the PDMS block in Figure 5.2. The empty squares indicate the temperature difference ($\Delta T = T_{ITO} - T_{TEC}$) between the top surface of the PDMS block and the bottom surface of the ITO film heater.

To estimate the temperature gradient inside the microchannel along the vertical direction, a three-dimensional numerical simulation of the steady temperature distribution in the microchannel is performed by using the commercial FEM software package COMSOL Multiphysics (V4.2). The numerical model consists of a water flow in the microchannel, the PDMS block and the glass slide. Four major sets of inputs are given as boundary conditions for the simulation: the temperature of the sample solution at the

microchannel inlet is set as room temperature (25 °C) with a fixed flow rate of 0.1 mL/h, the surface temperature of the top surface of the PDMS block covered by the TEC unit is set as a constant value measured by the thermocouple (T_{TEC}), a surface heat source is imposed on the region covered by the ITO film according to the applied power (P_{ITO}) in experiments, and a convection boundary condition is applied on the outer surfaces of the microchip for heat loss. The heat transfer coefficients are assumed at $30 \text{ W/m}^2\cdot\text{K}$ for the bottom surface of the glass slide, $5 \text{ W/m}^2\cdot\text{K}$ over the exposed area of the top of the PDMS block and the sides of the glass slide and the PDMS block after considering the working conditions in the lab. (Incropera and DeWitt 2002). With the given boundary conditions, the temperature distribution of the temperature-gradient microchip can be numerically solved, and the simulation results of the temperature gradient the microchannel centreline are shown in Figure 5.4-b. It is found that the average temperature gradient in the observation region varies from 78.9 K/m to 6846.9 K/m along the vertical direction of the microchannel centreline. Meanwhile, the average bulk temperature in the microchannel is changed from 332.73 K to 316.84 K.

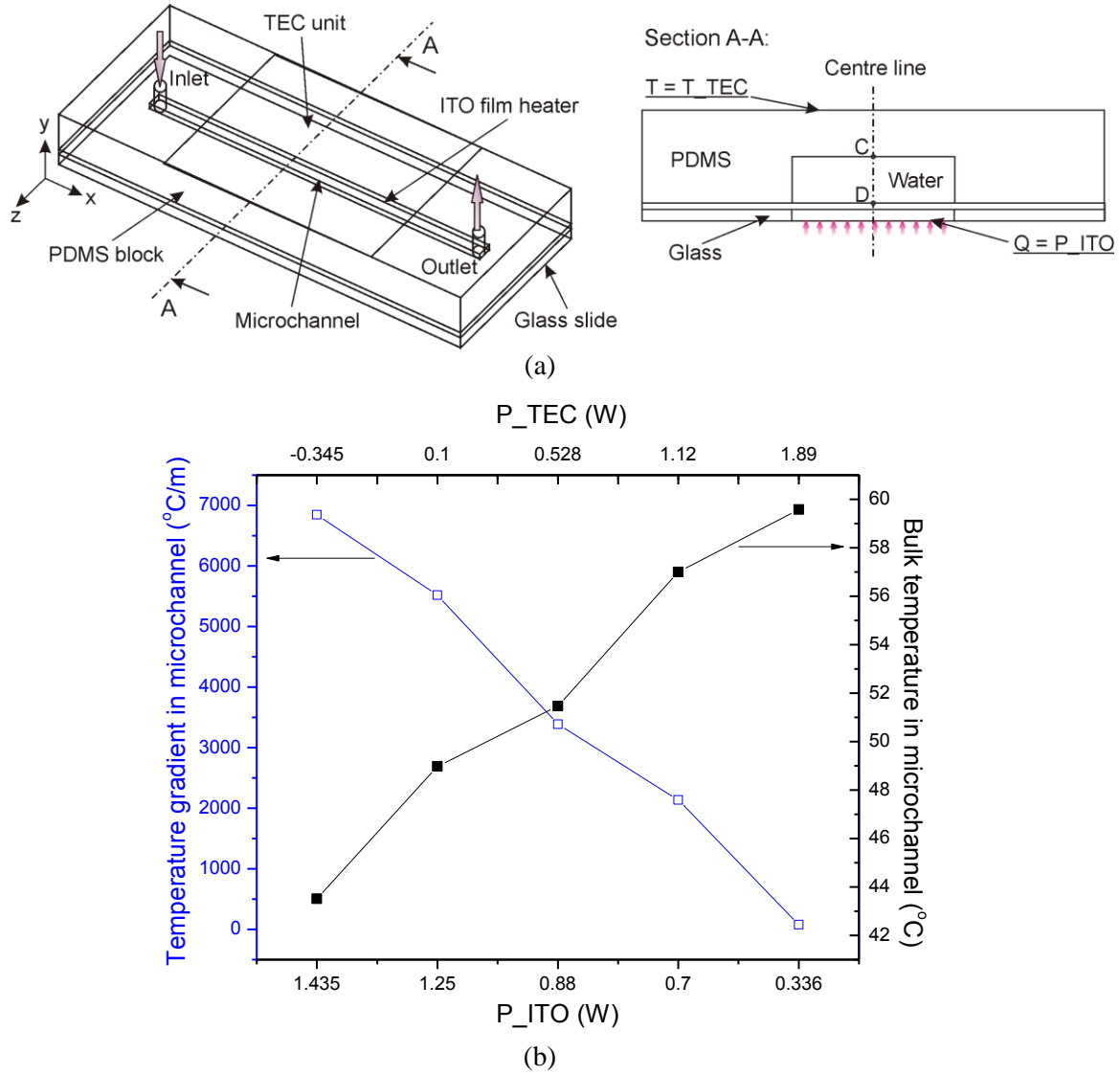


Figure 5.4 (a) The numerical model consisting of the microchannel and the PDMS block and the glass slide. (b) Temperature gradient ($-\square-$) along the centreline (CD shown in Section A-A) of the microchannel and bulk temperature ($-\blacksquare-$) in the observation region versus the power inputs to the TEC cooling unit (P_{TEC}) and ITO film heater (P_{ITO}). The bulk temperature is estimated as the average temperature along the centreline, $(T_C + T_D)/2$. Data are obtained by a three-dimensional simulation with boundary conditions: The surface temperature covered by TEC unit is set as constant ($T = T_{TEC}$), Constant surface heat source is applied onto the ITO film heater ($Q = P_{ITO}$), and convective heat transfer ($h = 30 \text{ W}/\text{m}^2 \text{ K}$ for bottom surface and $5 \text{ W}/\text{m}^2 \text{ K}$ for side and top surfaces of the PDMS block) is set between the chip and the ambient air to account for heat loss, a hydrodynamic flow with constant flow rate ($0.1 \text{ mL}/\text{h}$) and inlet temperature (25°C) is applied inside the microchannel.

5.1.2 EXPERIMENTAL PROCEDURES

For the experiments on particle deposition with temperature gradients, the general procedures are listed below:

- 1) The microchannel chip was cleaned in with DI water ultrasonic cleaner for about 2

hours.

- 2) A fine particle suspension of polystyrene beads (100 μ l, 930 nm in diameter, 1% solids) was dispersed with DI water (50 ml). The sample fluid was homogenized by using ultrasonic bath for about half an hour. Thereafter, the sample fluid was loaded into a glass syringe (5ml, Hamilton, USA).
- 3) The power of ITO film heater and TEC unit were set to the required values via the control panels of DC power supply according to values in Figure 5.3. The laser was turned on to warm up for about 10 minutes.
- 4) The syringe pump and microchip were connected by silicone tube. After the temperatures on the top and bottom surfaces of the microchip reached steady state (about 30 minutes), the syringe pump was turned on and started to supply the sample fluid with constant flow rate of 0.1 mL/h for one hour.
- 8) The captured area of interest (896 x 500 μ m²) was fixed at the centre point of the deposition channel in the longitude direction, where two thermocouples were used to measure the surface temperature. The CCD camera was switched on and its exposure time was set as 1s. Sequences of image were taken with a time interval of five minutes. Figure 5.5 shows typical particle images captured at different times when the temperature gradient was maintained at 6846.9 K/m. Since the focus plane is on the bottom surface of the deposition channel, only particles within the near-wall region can be seen clearly as black dots while particles far away from the bottom surface would be out of focus.

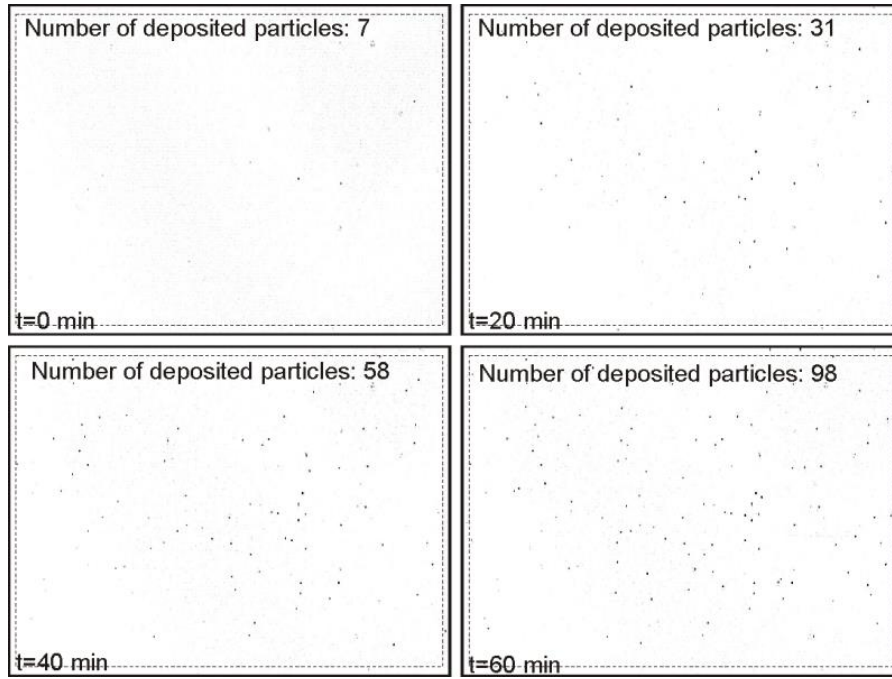


Figure 5.5 Videomicroscopic images of 0.93 μm polystyrene particles captured using 10X objective lens under temperature gradient maintained at 6846.9 K/m (0.1 mL/h, NaCl : 5×10^{-4} M) at 0min, 20min, 40min and 60min. Particles are shown as black dots.

5) After 60 minutes, the experiment was finished, and all the images were stored in computer for analysis. A software “Image Pro Plus” was employed to process the images of particle deposition by counting the number of deposited particles within the area of interest.

To investigate the effect of temperature gradient, the same procedure was repeated under different temperature gradients shown in Figure 5.4. To investigate the electrolyte effect, sample fluids were mixed with NaCl solution (1×10^{-1} M, 1×10^{-3} M) with volume ratio of 1 to 1. Thereafter, same procedure was followed as introduced above.

After completing the deposition measurements for a given system setting, the static dimensionless deposition rate, Sherwood number, can be computed as

$$\text{Sh}_{\text{exp}} = \frac{J_{\text{exp}}}{D_{\infty} n_{\infty, p} / a_p} \quad (5.1)$$

where J_{exp} is the measured particle deposition flux onto the bottom surface of the deposition channel, $n_{\infty, p}$ is the particle concentration of the bulk fluid, a_p represents the average particle

radius of the sample. D_∞ denotes the diffusion coefficient in bulk fluid which can be determined by the Stokes-Einstein equation. More details can be found in Section 4.1.2.

5.1.3 UNCERTAINTY ANALYSIS IN MEASUREMENTS

In this study, the uncertainty of the Sherwood number in experiments arise from three sources: the number of deposited particles, the measured observation area and the duration of the test. The uncertainty of the number of deposited particles is estimated based on the standard deviation of the counted deposited particle numbers for all of the repeated tests, which gives an uncertainty within 26% (shown as the error bar in the figures in Section 5.3). The accuracy of measuring the area of observed region and duration of experiment are about $1 \mu\text{m}^2$ and 1 s, respectively. The measurement uncertainties of the area of the observed region and experiment duration are about 0.000384% and 0.019%. Overall, the relative uncertainty for the experimental Sherwood number measured in the present study is approximated within 26%. In addition, the accuracy of the temperature measurement is about 0.2°C in this study base on results of temperature uniformity test by using micro-thermocouples. The current and voltage were measured by the multiple-meter with estimated errors of 0.01A and 0.1V, respectively according to the manual of the multiple-meter. The accuracy of the flow rate is determined by the syringe pump (KDS 210, USA), giving a value of 1%.

5.2 THEORETICAL MODELLING

In Chapter 3, a one-dimensional mass transport equation with consideration of thermal effect has been derived on the basis of the modified DLVO theory for the particle deposition in microchannels at elevated temperatures. This model is employed in this chapter to analyse the effect of temperature gradient on the particle deposition in microchannels with consideration of the thermophoretic force for different experimental conditions.

For particles suspended in a hydrodynamic flow under temperature gradient, the forces exerted on the particles consist of electric double layer force (shown in Eq. 3.25), van der Waals force (shown in Eq. 3.37), gravity (shown in Eq. 3.44), hydrodynamic lift force (shown in Eq. 3.46) and the thermophoretic force induced by temperature gradient. In this study, the dimensionless thermophoretic force is approximated as

$$\bar{F}_T = k_B T S_T \frac{dT}{dy} \frac{a_p}{kT_0} = \frac{dT}{dy} \frac{T}{T_0} S_T a_p \quad (5.2)$$

where T_0 indicates the reference temperature (293.15 K), dT/dy is the temperature gradient formed in the microchannel as shown in Figure 5.2-(b), S_T depicts the Soret coefficient ($S_T = D_T/D$) which is approximated as 1 based on the available literatures (Eslahian et al. 2014). The positive sign at right hand side of Eq. (5.2) indicates a repulsive potential to impede particle deposition. By integrating the thermophoretic force with separation distance (H), we obtain the dimensionless thermophoretic interaction potential at different temperatures as

$$\bar{V}_T = \frac{dT}{dy} \frac{T}{T_0} S_T a_p H. \quad (5.3)$$

The dimensionless particle number concentration (\bar{n}) is obtained by solving the one-dimensional mass transport equation shown in Eq. (3.20) with the two boundary conditions shown in Eqs. (3.21-3.22). In this study, a software Comsol Multiphysics (V.4.2) is adopted to numerically solve the mass transport equation with an iterative equation solver. Computational test are conducted to estimate the influence of H_0 on the numerical results. It is found that the numerical results are not affected significantly by the specific value of the integration limits so long as $H_0 \leq 0.005$ and $H_\infty \geq 20$. Thus, the lower and upper integration limits are taken as $H_0 = 0.001$ and $H_\infty = 25$, respectively, which are consistent with those applied in the literature (Sanders et al. 1995, Gu and Li 2002a).

With the solved dimensionless particle number concentration distribution (\bar{n}), the dimensionless particle deposition rate onto the channel surface ($H = H_0$) is calculated as

$$\text{Sh}_{num} = \frac{j_0}{(D_\infty n_\infty / a_p)} = -f_1(H_0) \left(\frac{d\bar{n}}{dH} \right)_{H=H_0} \quad (5.4)$$

where $f_1(H)$ is the universal hydrodynamic correction coefficient.

Table 5.1 shows the parameters for calculating the dimensionless concentration (\bar{n}) and Sherwood number (Sh_{num}) for different experimental conditions. The values of dimensionless parameters (Ad , DI , Da , τ) are computed based on the material properties (ρ , μ) and the empirical correlations from the available literatures (Maidment 1993, Knox and McCormack 1994, IAPWS 1997a, b). Details can be found in Section 3.4.

Table 5.1 Values of the parameters used for modelling at different temperatures

T (K)	Ad	DI	Da	τ	ρ_{water} (kg/m ³)	μ (x 10 ⁻³ Pa s)
316.84	0.396	40.312	2.449	4.463	990.787	0.615
322.26	0.399	37.591	2.449	4.712	998.463	0.562
324.65	0.401	36.437	2.449	4.821	987.376	0.540
330.20	0.405	33.867	2.449	5.074	984.707	0.494
332.73	0.408	32.561	2.449	5.209	983.211	0.467

Finally, the Sherwood number (Sh) will be used to compare with the experimental results, and gain more insights of the parametric effects of the experimental variables on the particle deposition in microchannels in the following sections.

The total interaction potential (\bar{V} shown in Eq. (3.18)) will be plotted versus the dimensionless separation distance ($H=h/a_p$), also known as the interaction potential curve of particle deposition. This interaction potential curve will be implemented to analyse the experimental results in the following sections.

5.3 RESULTS AND DISCUSSION

In this section, the effects of the temperature gradient and the electrolyte concentration on the particle deposition in microchannel are discussed both experimentally and theoretically. For each case, a comparison is conducted between the numerical results and experimental results.

5.3.1 EFFECT OF TEMPERATURE GRADIENT ON PARTICLE DEPOSITION

Temperature gradient

In the experiments, the temperature gradient inside the microchannel was varied from 78.9 K/m to 6946.9 K/m by controlling the power supplied to the TEC unit (P_TEC) and ITO film heater (P_ITO) while the flow rate of sample was maintained at 0.1 mL/h. Before the sample fluid was supplied to the microchannel, a stable temperature gradient had been formed in the vertical direction in the observation region of the microchannel. The particle deposition at different temperature gradients are plotted versus time in Figure 5.6. As shown in Figure 5.6, the number of deposited particles per unit area is increased gradually with time for all the temperature gradients. After 60 minutes, the number of deposited particles per unit area ($373/\text{mm}^2$) with low temperature gradient (78.9 K/m) is more than doubled from $163/\text{mm}^2$ with high temperature gradient (6846.9 K/m).

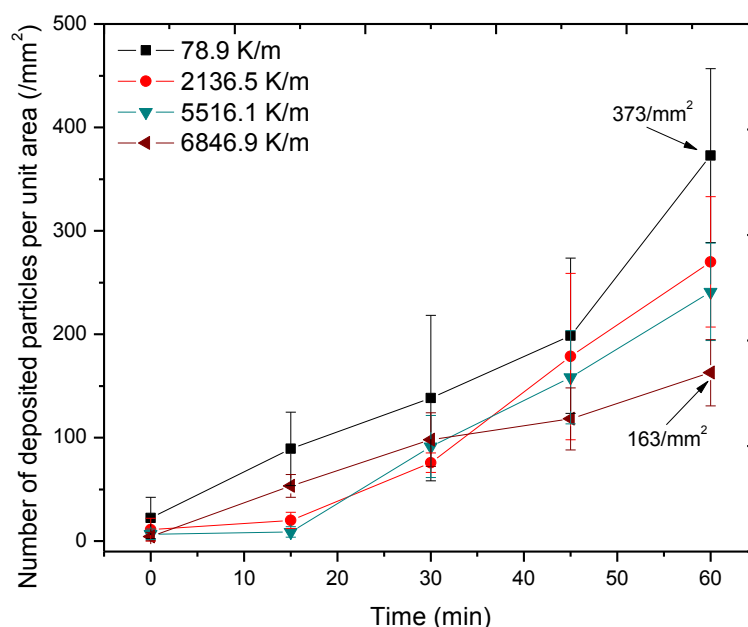


Figure 5.6 Number of deposited particles per unit area versus deposition time for four different temperature gradients at 78.9 K/m, 2136.5 K/m, 5516.1 K/m and 6846.9 K/m. Data are for fluorescent polystyrene particles dispersed in a *NaCl* solution (5×10^{-4} M). The sample flow rate is fixed at 0.1 mL/h. Sample solution is supplied to the microchannel after a stable temperature gradient is formed inside the microchannel. The corresponding bulk solution temperatures for each temperature gradient are 332.73 K, 330.20 K, 324.65 K, 322.26 K, 316.84 K, respectively.

Figure 5.7 summarises the Sherwood numbers from the experimental measurements (Sh_{exp}) and the numerical calculations (Sh_{num}) for different temperature gradients. It can be seen that the Sherwood number is monotonically decreased with increasing the temperature gradient along the vertical direction inside the microchannel. The Sherwood number is reduced by more than 50% from 0.0186 to 0.0082 when the temperature gradient is increased from 78.9 K/m to 6846.9 K/m in experiments. This indicates that the temperature gradient has negative effect on the particle deposition process in microchannels, leading to a reduction of particle deposition rate. The numerical results of Sherwood number (Sh_{num}) is calculated based on the derived model with the given experimental conditions as input parameters of modelling. The values of numerical results (Sh_{num}) in Figure 5.7 are comparable with the corresponding experimental results. It is suggested that the particle deposition under temperature gradient can be reasonably described by the mass transport equation developed on the basis of the modified DLVO theory.

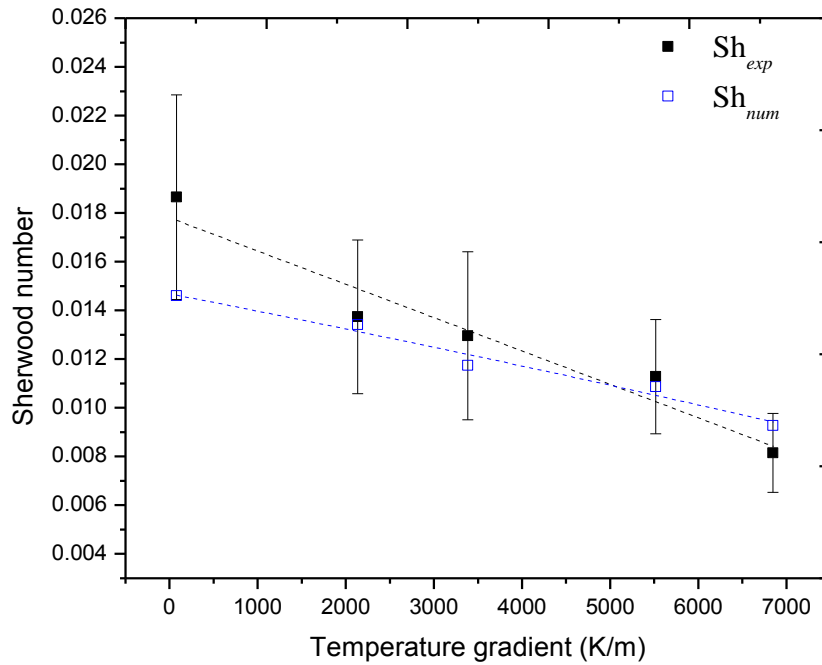


Figure 5.7 Dimensionless static deposition rate (Sherwood number) as a function of the temperature gradients at 78.9 K/m, 2136.5 K/m, 3385.7 K/m, 5516.1 K/m and 6846.9 K/m. Solid squares (■) indicate the measured Sherwood number Sh_{exp} shown in Eq. (5.1) from experiments, and empty squares (□) show the calculated Sherwood number Sh_{num} by Eq. (5.4) from modelling. The dotted line shows the least-square fitting line. Data are for fluorescent polystyrene particles dispersed in a *NaCl* solution (5×10^{-4} M) with fixed flow rate 0.1 mL/h. The corresponding bulk solution temperatures for each temperature gradient are 332.73 K, 330.20 K, 324.65 K, 322.26 K, 316.84 K, respectively.

The reduction of particle deposition rate (Sh) with temperature gradient in Figure 5.7 is probably due to the following two reasons. Firstly, the thermophoretic force is a repulsive long-range force, which points upward against the particle deposition in this study. The thermophoretic force is increased with increasing the temperature gradient in the microchannel. When particles are far away from the channel surface, the transport of particles from the bulk solution to the near-wall region is mainly controlled by the external forces including the thermophoretic force. With higher temperature gradient, the particles would experience larger resistance from thermophoretic force so that fewer particles could approach to the near-wall region. Secondly, the bulk solution temperature inside the channel is reduced with increasing the temperature gradient in the experiments, as shown in Figure 5.4. The energy barrier is therefore increased with reducing the bulk solution temperature in the microchannel, which hinders the particle deposition in the near-wall region. Subsequently, the particle deposition rate is reduced by the collective effects of the temperature gradient and the bulk solution temperature as observed in the experiments. In other words, a higher temperature gradient is an unfavourable condition for the particle deposition in this study, because fewer particles could approach to the channel surface, especially, when the bulk solution temperature is low. Deposition rate of particles would be consequently reduced with increasing the temperature gradient in experiments.

Interaction potential curve

In order to better understand the effect of temperature gradient on the particle deposition at elevated temperatures, the total particle-channel interaction potential (\bar{V}) is calculated based on Eq. (3.18), and is plotted versus the dimensionless separation distance H in Figure 5.8. It can be clearly seen in Figure 5.8-a that the shapes of interaction potential curves for different temperature gradients are similar, having an energy barrier with both the primary energy minimum (PEM) and the shallow secondary energy minimum (SEM). Because the thermophoretic force acts in long distance compared with the colloidal forces, it would mainly influence the transport of particles from bulk solution to the PEM region. As shown in Figure 5.8-

b, the total interaction potential at $H = 10$ is increased by 50% from 0.38 to 0.58, when the temperature gradient is increased from 78.9 K/m to 6846.9 K/m. The positive total interaction potential with high temperature gradient ($H = 10$) may hinder the particles approaching to the channel surface. As a result, it is more difficult for the particles to transport to the near-wall region with high temperature gradient, leading to reduction of the particle deposition rate. Besides, the colloidal interactions (EDL and vdW forces) dominate the particle deposition process after the particles reach the near-wall region. A repulsive energy barrier is formed by the competition of vdW and EDL interactions to prevent particle attachment onto the channel surface. The energy barrier is plotted versus the temperature gradient in Figure 5.8-b. It shows that the energy barrier is increased by 92% from 0.91 to 1.75 with increasing the temperature gradient. This is mainly caused by the decreased bulk solution temperature from 332.73 K to 316.66 K as shown in Figure 5.4. The increased energy barriers at high temperature gradients would further attenuate the particle deposition. With the aid of the discussions about interaction potential curve, the observed trend of particle deposition rate with increasing the temperature gradient can be well explained.

It can be concluded that the particle deposition rate is monotonically reduced with increasing the temperature gradient in the present study. The reduction of particle deposition rate observed in the experiments is attributed to the increased resistance for the particle deposition, induced by the enhanced thermophoretic force with the temperature gradient. The thermophoretic force is a repulsive interaction, and mainly influences the transport of the particles from the bulk solution to the microchannel surface. Fewer particles could be transported to the near-wall region at high temperature gradient. Besides, the reduced particle deposition rate is caused by the decreased bulk solution temperature with the temperature gradient in the experiments. The energy barrier is increased with the decreased bulk solution temperature, which can impede the particle deposition in the final stage of particle attachment.

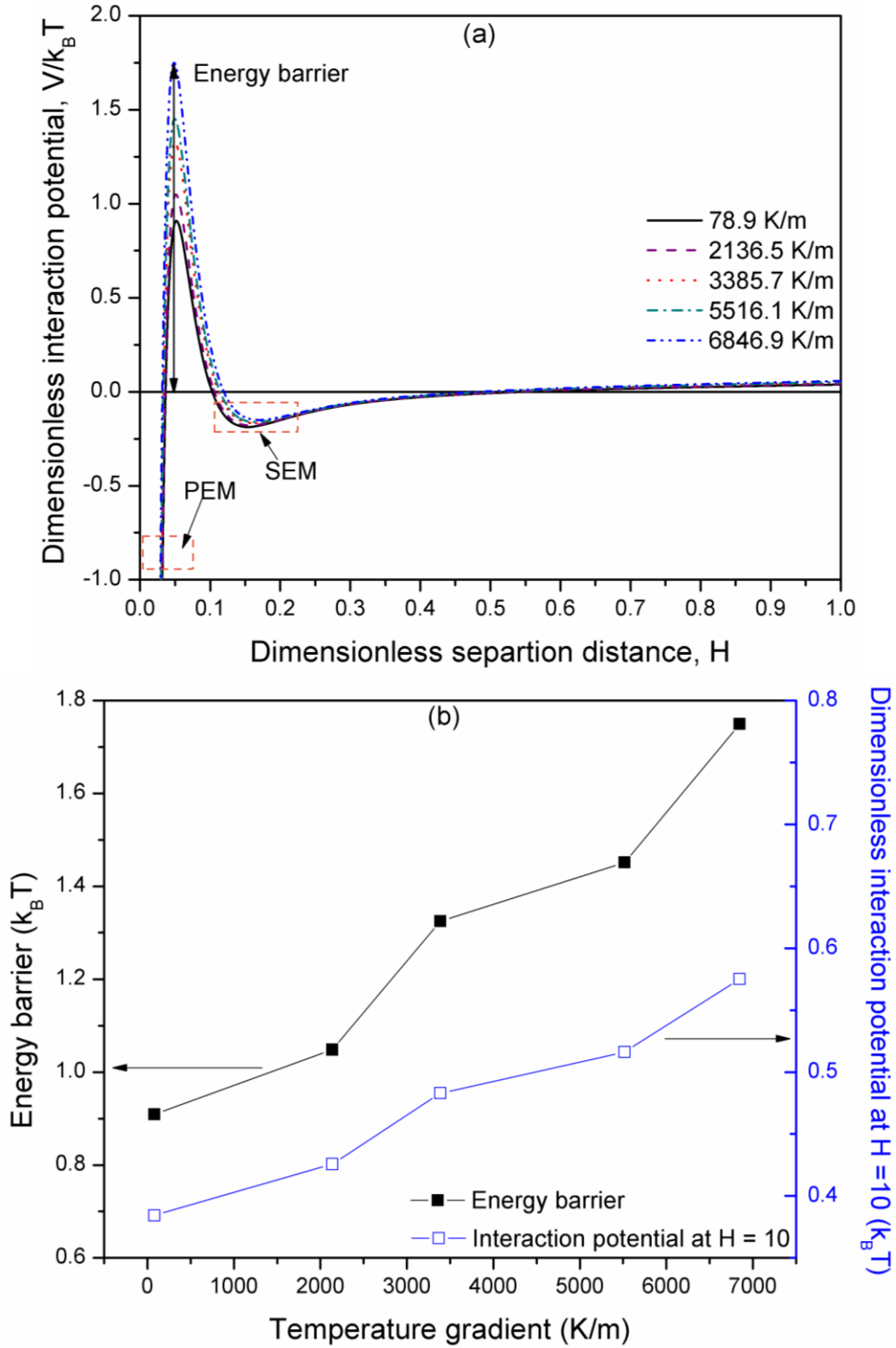


Figure 5.8 (a) Dimensionless particle-microchannel interaction potential \bar{V} versus the dimensionless separation distance H for different temperature gradients. (b) The energy barrier (shown by \blacksquare) and the interaction potential at $H = 10$ (shown by \square) as a function of the temperature gradient. Data are calculated based on Eq. (3.18) for fluorescent polystyrene particles dispersed in a *NaCl* solution (5×10^{-4} M) with a fixed sample flow rate 0.1 mL/h. The dotted square SEM indicates the secondary energy minimum region, and the dotted square PEM indicates the primary energy minimum region.

5.3.2 EFFECT OF ELECTROLYTE CONCENTRATION ON PARTICLE DEPOSITION UNDER TEMPERATURE GRADIENTS

Electrolyte concentration

Electrolyte concentration or ionic strength is a common parameter encountered in particle deposition processes. In this section, the effect of electrolyte concentration on particle deposition in microchannels was studied with different temperature gradients at elevated temperatures. Experiments were conducted by varying the molar concentration of *NaCl* solution for three different solutions (DI water, 5×10^{-4} M, 5×10^{-2} M) while the sample flow rate was fixed at 0.1 mL/h. For each electrolyte concentration, three temperature gradients were investigated including 78.9 K/m, 3385.7 K/m and 6846.9 K/m.

Figure 5.9 shows the number of deposited particles per unit area changing with time when the sample flow rate and temperature gradient are fixed at 0.1 mL/h and 6846.9 K/m, respectively. As shown in Figure 5.9, the number of deposited particles per unit area is increased gradually with time for different electrolyte concentrations, but is increased much faster with high electrolyte concentration (5×10^{-2} M) than that with the medium electrolyte concentration (5×10^{-4} M) and DI water. Moreover, it can be seen clearly that there is no appreciable change of the number of deposited particles for the DI water case. After 60 minutes, the number of deposited particles per unit area with high electrolyte concentration (5×10^{-2} M), 528/mm², is more than ten times larger than 37/mm² for DI water.

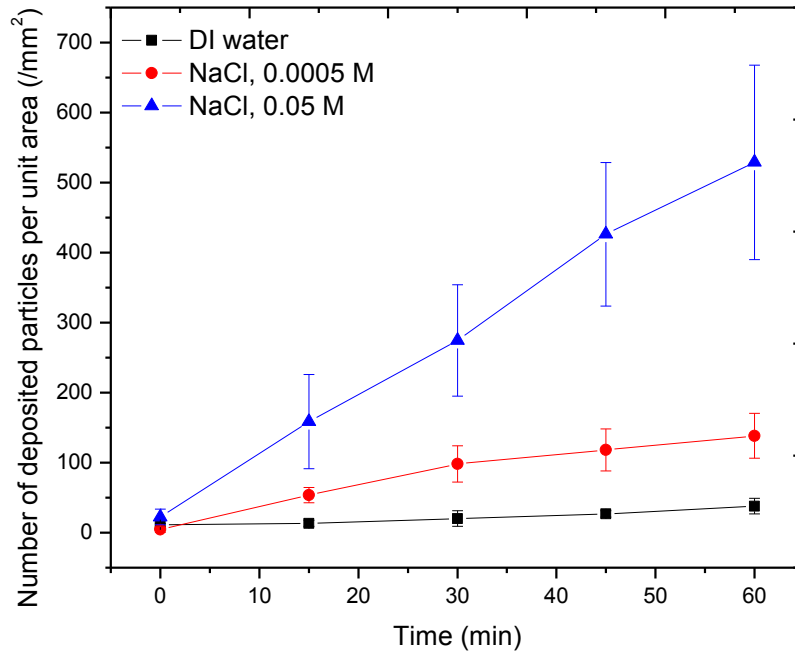


Figure 5.9 Number of deposited particles per unit area versus deposition time at different electrolyte concentrations with fixed temperature gradient at 6846.9 K/m and constant sample flow rate at 0.1 mL/h. Data are for fluorescent polystyrene particles dispersed in DI water and *NaCl* solutions (5×10^{-4} M, 5×10^{-2} M). Sample solution is supplied to the microchannel after a stable temperature gradient is formed inside the microchannel.

The dimensionless static particle deposition rate from the experiments (Sh_{exp}) and modelling (Sh_{num}) for different electrolyte concentrations are plotted versus the electrolyte concentration with the constant sample flow rate of 0.1 mL/h in Figure 5.10. It illustrates that the Sherwood number is monotonically increased with increasing the electrolyte concentration of the sample fluid. The Sherwood number (Sh_{exp}) is significantly increased by about 16 times, from 0.0013 to 0.0022, with increasing the electrolyte concentration from DI water to 5×10^{-2} M for the high temperature gradient of 6846.9 K/m. For the low temperature gradient (78.9 K/m), the enhancement of the particle deposition rate (Sh_{exp}) from DI water to 5×10^{-2} M are about 8 times, from 0.005 to 0.044, shown in Figure 5.10. These scenarios indicate that the electrolyte concentration plays a crucial role on the particle deposition process with a given temperature gradient, and the effects of electrolyte concentration become more significantly with higher temperature gradients in the microchannel.

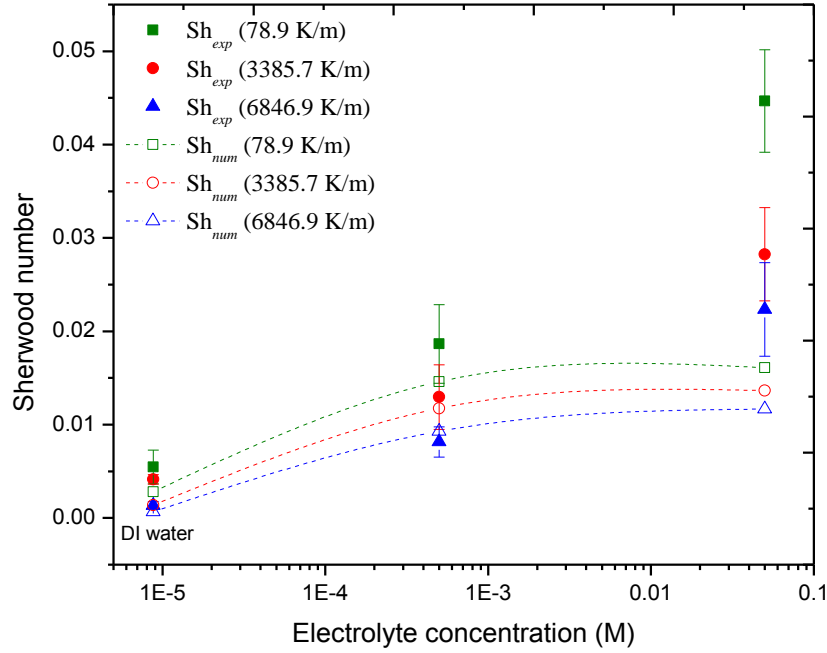


Figure 5.10 Dimensionless static deposition rate (Sherwood number) versus the electrolyte concentration for DI water, 5×10^{-4} M and 5×10^{-3} M. Solid symbols indicate the measured Sherwood number Sh_{exp} shown in Eq. (5.1) from experiments, and empty symbols show the calculated Sherwood number Sh_{num} by Eq. (5.4) from modelling. Squares show the results for the temperature gradient of 78.9 K/m. Triangles show the results for the temperature gradient of 3385.7 K/m. Circles show the results for the temperature gradient of 6846.9 K/m. Data are for fluorescent polystyrene particles dispersed in DI water and *NaCl* solutions. The sample flow rate is fixed at 0.1 mL/h.

The calculated Sherwood numbers (Sh_{num}) from the derived model are also presented in Figure 5.10. It shows that the calculated Sherwood numbers demonstrate a similar trend to the measured data (Sh_{exp}) in experiments. The numerical results (Sh_{num}) fairly agree with the experimental results (Sh_{exp}) in the same magnitude for DI water and medium electrolyte concentration case (5×10^{-4} M), though a discrepancy can be seen for the high electrolyte concentration case (5×10^{-2} M). The discrepancy between the experimental and numerical results could be due to the errors induced by the empirical correlations for the dependences of temperature and electrolyte concentration from literature.

The observed variations of Sherwood number with changing electrolyte concentration can be understood as follows. Because both polystyrene particle and PDMS channel surfaces carry negative charges, a repulsive EDL interaction exists between these two surfaces. The Debye length (κ^{-1}), which is usually used to characterise the EDL thickness, is reduced with increasing the electrolyte concentration of sample fluids. Besides, the zeta potentials of particle and

microchannel are decreased with the electrolyte concentration. In other words, the increased electrolyte concentration can not only compress the EDL thickness but also reduce the magnitude of the EDL interaction, leading to a favourable environment for particle deposition. The remarkable enhancement with high temperature gradient could be attributed to the changes of interactions related to thermal conditions. Thus, the particle deposition rate is increased with the electrolyte concentration at fixed sample flow rates and thermal conditions.

Interaction potential curve

In order to better understand the results of particle deposition with different electrolyte concentrations under temperature gradients, the interaction potential curve is plotted in Figure 5.11 based on Eq. (3.18). It can be observed in Figure 5.11-a that three distinct shapes of the interaction potential curves are observed for the three electrolyte concentrations. For the DI water case, only energy barrier with PEM is presented in Figure 5.11-a. The energy barrier for DI water is much larger than those for the medium electrolyte concentration (5×10^{-4} M) and the high electrolyte concentration (5×10^{-2} M) in Figure 5.11-b. This indicates that the particles in DI water have lower chances to overcome the energy barrier and leads to fewer particles deposited at PEM. After increasing the electrolyte concentration to 5×10^{-4} M, an interaction potential curve with a moderate energy barrier and PEM together with a shallow SEM can be seen in Figure 5.11-a. The energy barrier is reduced by 80% with increasing the electrolyte concentration to 5×10^{-4} M in Figure 5.11-b. The reduced energy barrier would improve the particle deposition condition, and allow more particles could overcome the energy barrier to attach onto the channel surface. For the high electrolyte concentration case (5×10^{-2} M), there is only PEM without energy barrier as shown in Figure 5.11-a. It is expected that the particles can easily deposit onto the channel surface after approaching to the near-wall region.

On the other hand, it can be observed in Figure 5.11-b that the energy barrier at the high temperature gradient (6846.9 K/m) is reduced from 5.85 to 0 with increasing the electrolyte concentration from DI water to 5×10^{-2} M, which is larger than the reduction from 4.67 to 0 for

the low temperature gradients (78.9 K/m). The energy barrier under different temperature gradients for a given electrolyte concentration is mainly determined by the bulk solution temperature. Because the bulk solution temperature is reduced with the temperature gradient in the experiments as shown in Figure 5.4, the energy barrier is increased with the reduced bulk solution temperature. This could explain that the effect of electrolyte on particle deposition is more remarkable with the high temperature gradient than that with low temperature gradient, as observed in Figure 5.10.

It can be concluded that the particle deposition is strongly affected by the electrolyte concentration of sample fluid which determines the magnitude of repulsive energy barrier for a given thermal condition. The particle deposition rate is monotonically increased with increasing the electrolyte concentration. The enhancement of particle deposition with the electrolyte concentration becomes more remarkable with high temperature gradient than low temperature gradient.

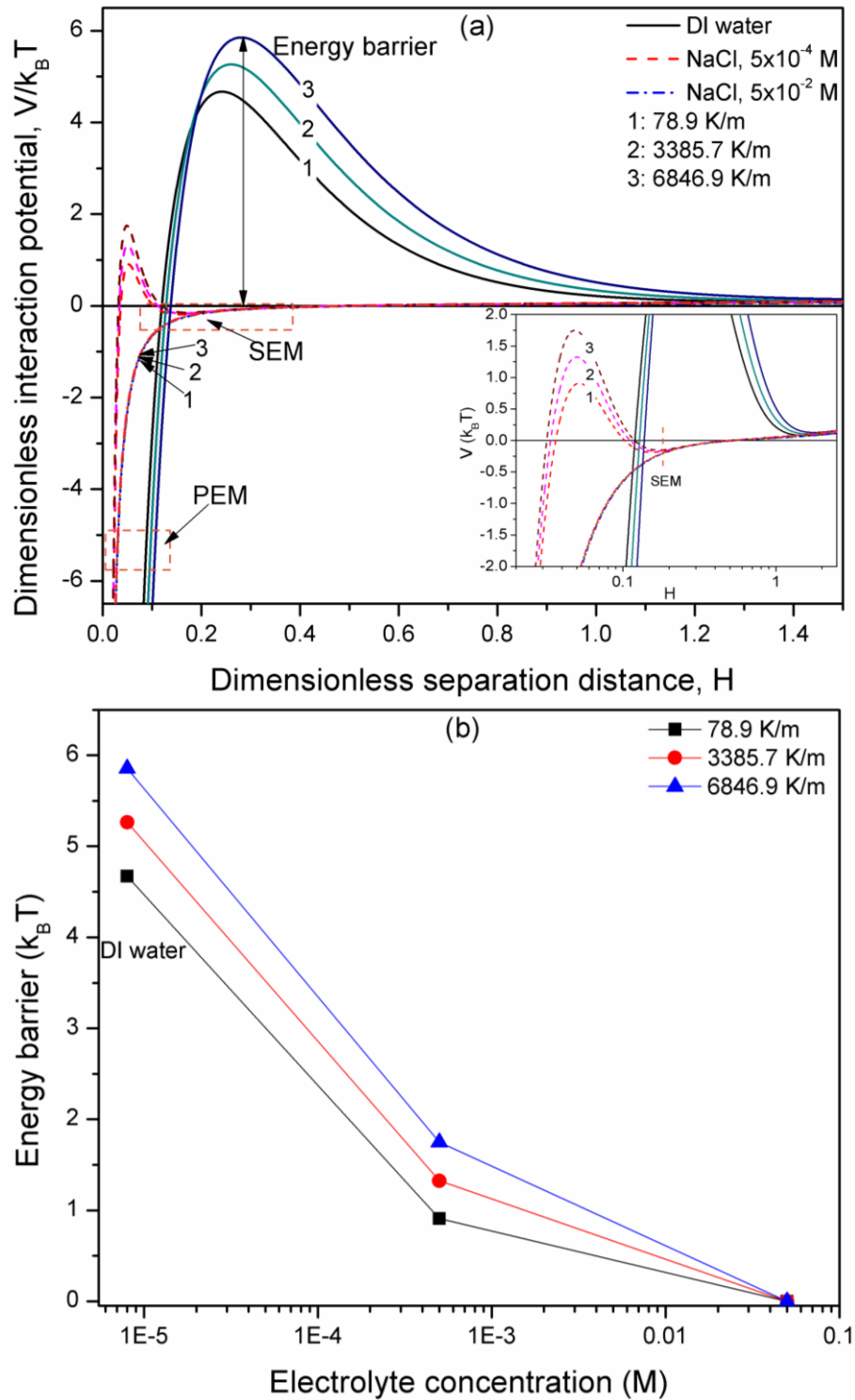


Figure 5.11 (a) Dimensionless particle-microchannel interaction potential \bar{V} versus the dimensionless separation distance H for three electrolyte concentrations: DI water, 5×10^{-4} M and 5×10^{-2} M under different temperature gradients (1: 78.9 K/m, 2: 3385.7 K/m, 3: 6846.9 K/m), Inset shows the enlarged view for the electrolyte concentrations at 5×10^{-4} M and 5×10^{-2} M. (b) The energy barrier as a function of the electrolyte concentration for three different temperature gradients. Data are calculated based on Eq. (3.18) for fluorescent polystyrene particles dispersed in DI water and *NaCl* solution (Sample flow rate: 0.1 mL/h). The dotted square SEM indicates the secondary energy minimum region, and the dotted square PEM indicates the primary energy minimum region.

5.4 SUMMARY

In this chapter, a specially designed temperature-gradient microfluidic system provides a useful platform to study the particle deposition process with a wide range of thermal conditions. To the best knowledge of the author, it could be the first time to directly observe the dynamic process of particle deposition along the direction of applied temperature gradient. Experimental results show that the particle deposition in microchannels at elevated temperature is not only affected by the temperature gradient but is also influenced by the electrolyte concentration or ionic strength of sample fluids.

With a given sample flow rate and electrolyte concentration, the dimensionless static particle deposition rate (Sh) is observed to decrease with increasing temperature gradient. By keeping the hydrodynamic and thermal conditions as constant, results show that Sherwood number is monotonically increased with increasing electrolyte concentration of sample fluids. Based on the analysis of the derived model, the observed reduction of particle deposition rate with temperature gradient is due to the collective effect of the temperature gradient and the bulk solution temperature on the two steps of particle deposition process, including the particle transport and the particle attachment. The results show that the temperature gradient affects the transport of particles at long range by the thermophoretic force acting on particles, while the bulk solution temperature determines the energy barrier to impede the particle attachment at the attachment step. The enhancement of particle deposition with increasing electrolyte concentration is due to the decreased energy barrier resulting from the compressed EDL thickness and reduced magnitude of EDL interaction. The enhancement of particle deposition with the electrolyte concentration becomes more remarkable with high temperature gradient than low temperature gradient.

Chapter 6

Effect of Hydrodynamic Flow on Particle Deposition in Microchannels at Elevated Temperatures

6.1 INTRODUCTION

Hydrodynamic flow is an important parameter for particle deposition, and it could influence the particle deposition rate by inducing the hydrodynamic interaction between particles and solid surfaces. Two types of hydrodynamic flows have been widely implemented in lab-on-chip applications, including steady flow and pulsatile flow. As shown in Figure 6.1, the steady flow with a parabolic velocity profile provides a constant flow rate in the channel, while the pulsatile flow generates a retarded velocity profile and a time-dependent flow rate over time in the channel. A pulsatile flow can be decomposed into a steady flow component and an oscillatory flow component. The general form of flow rate for pulsatile flow in the channel can be described by

$$Q_{pul} = Q_s + Q_{os} \quad (6.1)$$

where Q_{pul} is the flow rate of the pulsatile flow, Q_s is the steady component, and Q_{os} is the oscillatory component.

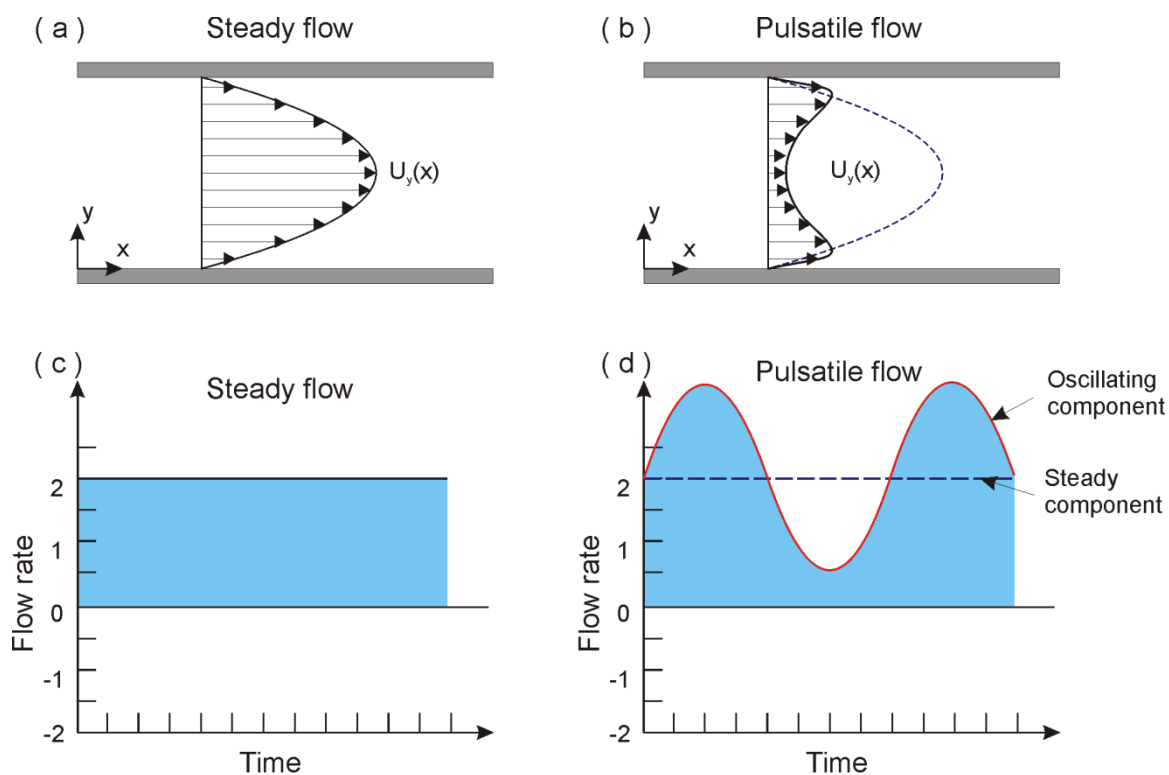


Figure 6.1 Characteristics of steady flow and pulsatile flow. (a) and (b) Schematics of axial velocity profiles across channels, (c) and (d) Schematics of flow rate versus time for steady flow and pulsatile flow, respectively. Area filled by colour indicates the volume of fluid moved during a certain period of time. The volume of fluid moved by pulsatile flow can be decomposed to a steady component from steady flow and an oscillating component from oscillatory flow (Figures are not drawn to scale).

In this chapter, the effect of hydrodynamic flow on particle deposition is investigated as an option to mitigate the particle deposition in microchannels at elevated temperatures. Steady flow and pulsatile flow are experimentally studied by using the designed microfluidic system. (1) The steady flow is supplied to the microchannel by a syringe pump. Experimentally and numerically determined particle deposition rates are presented for different flow rates of sample solution in the microchannel. Thermal effect on the particle deposition in a steady flow is studied with a fixed volume flow rate. (2) The pulsatile flow is generated by a specially designed pulsation generation unit together with the syringe pump. The oscillatory component of the pulsatile flow is regulated by the pulsation generation unit while the steady component is controlled by the syringe pump. The effect of flow pulsation on particle deposition at elevated temperatures is experimentally investigated by comparing the experimental results of pulsatile flow with those of the steady flow.

6.2 EXPERIMENT

6.2.1 EXPERIMENTAL SETUP

Figure 6.2 shows the schematics of the microfluidic system, consisting of fluid supply parts, a microchip, a data acquisition unit and a pulsation generation unit. One syringe pump (sample pump) is used to supply sample fluids to the microchip for different hydrodynamic flows, and another two syringe pumps (hot water pump) are implemented to supply hot water to regulate the thermal environment of the microchip. The temperature in the microchannel is well controlled by regulating the flow rate of the hot water sucked from a water bath. The temperature of hot water in the water bath is maintained constant (60 °C) in this study. The microchip and data acquisition unit are the same as those used in Chapter 4. More details can be found in Chapter 4. In addition, for experiments with pulsatile flow, a pulsation generation unit (PGU) is installed between the sample pump and the microchip to generate a controllable flow pulsation into the sample flow. The frequency and amplitude of the driving signal for the PGU can be controlled by a function generator.

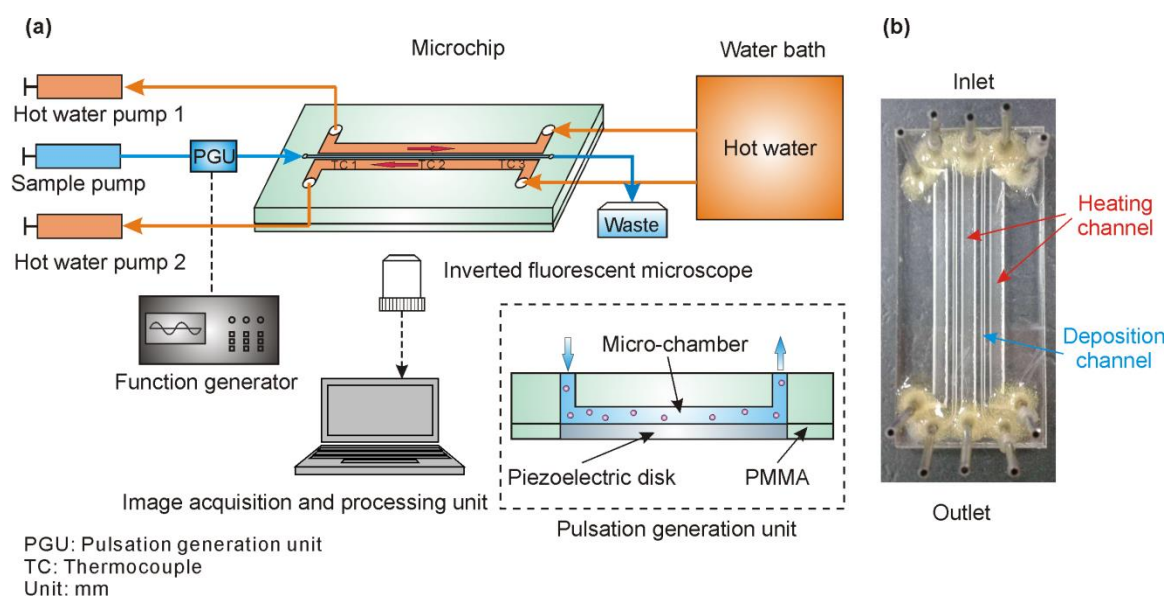


Figure 6.2 The layout of the microfluidic system. (a) Schematic of the microfluidic system with pulsatile flow for the direct observation of the particle deposition kinetics in microchannels. Inset: Cross-section view of pulsation generation unit. A pulsation generation unit (PGU) connecting to a function generator is implemented to generate a controllable flow pulsation into the hydrodynamic flow in the microchannel. (b) Photo of the microchip used in the experiments (Figure is not drawn to scale)

6.2.1.1 MATERIALS

In this study, red fluorescent dyed polystyrene microparticles (R900, Duke Inc., USA) are used to study the particle deposition under different bulk solution temperatures. The particles have a density of 1.05 g/cm^3 and a diameter of $0.93 \text{ }\mu\text{m}$ (a_p) with a size variation of up to $0.03 \text{ }\mu\text{m}$. Particle samples are prepared by first diluting a particle dispersion with a concentration (n_∞) of $5.6 \times 10^6/\text{ml}$ into de-ionized (DI) water, and then mixing with sodium chloride solutions (NaCl , Sigma-Aldrich, ACS reagent, $\geq 99.0\%$) for a constant electrolyte concentrations ($5 \times 10^{-4} \text{ M}$). The samples are homogenized by using an ultrasonic bath (Elmasonic E30H, Elma Ultrasonics) for half an hour before loading into a syringe for testing. The ambient temperature of the laboratory is recorded at $25.0 \pm 1.0 \text{ }^\circ\text{C}$ for all the experiments.

6.2.1.2 PULSATION GENERATION UNIT

In this study, a pulsation generation unit (PGU) is designed to generate and control the pulsatile flow in the microchannel. With the help of this pulsation generation unit, the flow field in the microchannel can be readily switched from a steady flow to a pulsatile flow. The pulsation generation unit consists of a circular microchamber embedded with a piezoelectric (PZT) disk. The PZT disk is driven by the function generator as shown in Figure 6.2. Figure 6.3 shows the schematic and images of the pulsation generation unit, which is composed with three layers. The top layer is a square PMMA plate ($50 \text{ mm} \times 50 \text{ mm} \times 3 \text{ mm}$) where two circular holes are cut through as the inlet and outlet for the sample solution. The middle layer as a spacer is made of a thin adhesive tape ($50 \text{ mm} \times 50 \text{ mm} \times 0.075 \text{ mm}$) with a circular laser-cut hole (radius: 14 mm) at the centre. This adhesive layer is carefully placed on one side of the top layer in a concentric manner. The bottom layer is made of a PMMA sheet ($40 \text{ mm} \times 40 \text{ mm} \times 1 \text{ mm}$) where a circular hole (radius: 12 mm) is cut through at the central part. The piezoelectric disk is inserted into the hole of the bottom layer, and attached to the adhesive layer by pressing the backside of the PZT disk. The gap between the disk and the bottom layer is firmly sealed with epoxy glue to prevent

leakage. Finally, a microchamber (height: 50 μm) is formed between the top and bottom layers, and a steady laminar pulsatile flow can be generated by turning on the piezoelectric disk with required frequency and amplitude. The frequency and amplitude of the driving signal to the PZT disk can be controlled by the function generator.

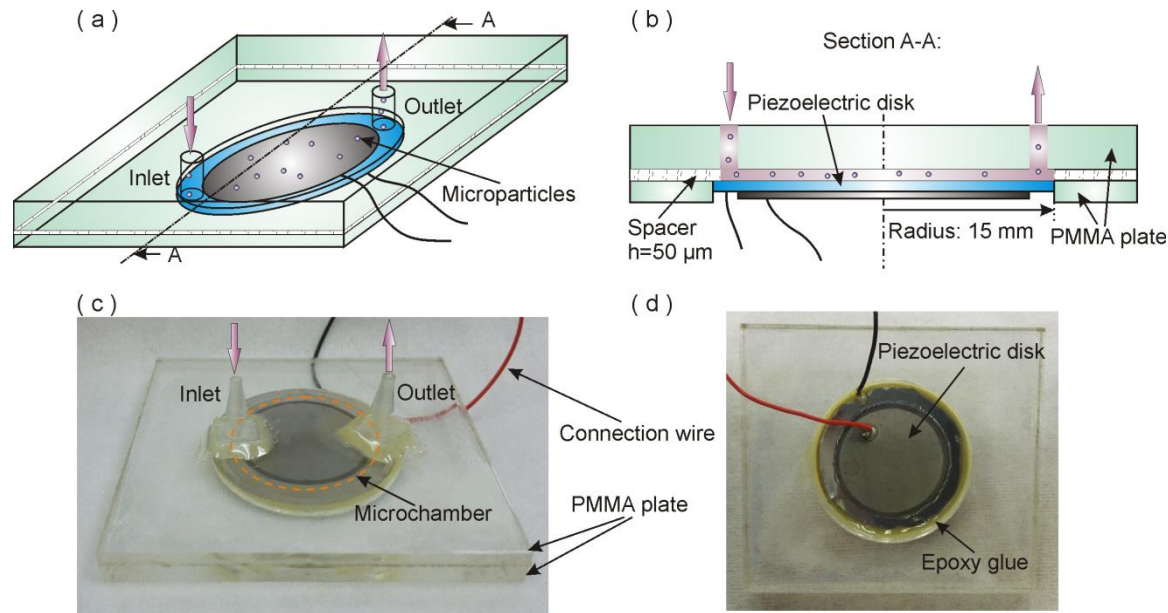


Figure 6.3 Schematic of pulsation generation unit, (a) isometric view, (b) cross-section view, (c) and (d) Images of the fabricated pulsation generation unit. The piezoelectric (PZT) disk is connected to a function generator to generate a controllable pulsation in the sample flow. The frequency and amplitude of the PZT disk is well controlled by regulating the sinusoidal signal from the function generator.

6.2.1.3 CHARACTERISATION OF THE OSCILLATORY FLOW GENERATED BY THE PULSATION GENERATION UNIT

In order to characterise the oscillatory component of the pulsatile flow generated by the pulsation generation unit, a purely oscillatory flow was generated by the designed pulsation generation unit. Measurements were conducted for the oscillatory flows with the following setup and procedure.

Two glass capillaries with internal diameter of 0.335 mm were fixed onto the inlet and outlet of the pulsation generation unit. To measure the average flow properties of oscillatory flow with zero back pressure, the glass capillaries were positioned horizontally as shown in Figure 6.4. The

microchamber of the pulsation generation unit and the glass capillaries were filled with DI water. The function generator was connected to the pulsation generation unit, and provided different sinusoidal signals for the piezoelectric (PZT) disk embedded in the pulsation generation unit. The electric signals were converted to mechanical deflections of the PZT disk. These motions were transferred to the DI water in the microchamber. As a result, an oscillatory flow was generated in the DI water and can be visualised through the glass capillaries. The water/air interface meniscus oscillated under the periodic vibration of the PZT disk. A CCD camera was implemented to record the motion of the centre point of water/air interface for post processing of data.

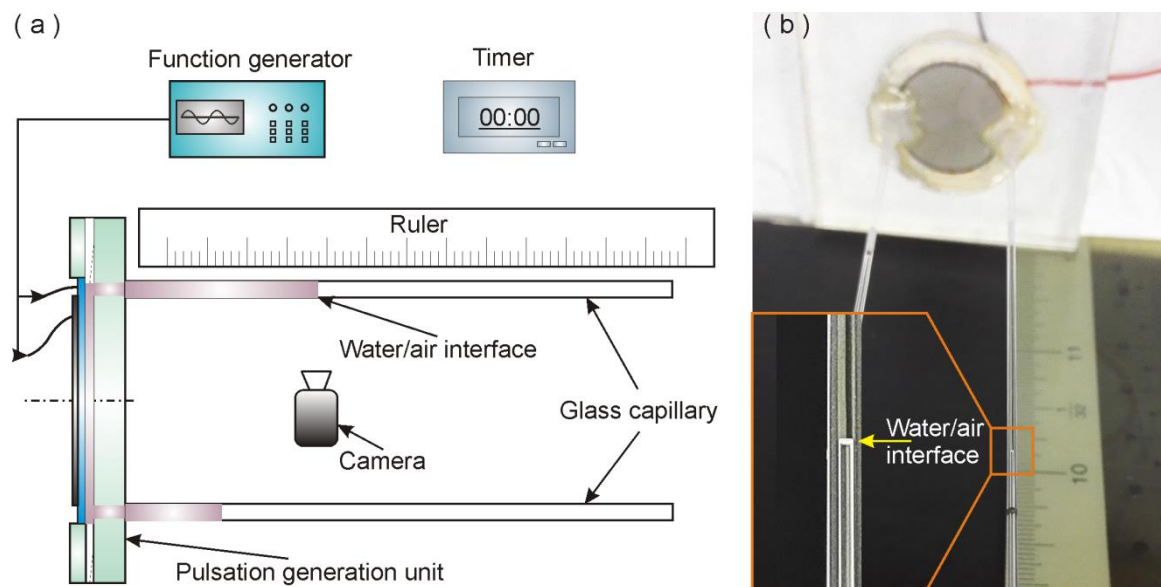


Figure 6.4 (a) Schematic of the experimental setup for characterisation of the oscillatory flow generated by the pulsation generation unit, (b) Photo of the flow rate measurement of the oscillatory flow.

The procedure for characterising the oscillatory flow under different frequency is listed below:

- 1) DI water was filled into the pulsation generation unit and capillary tubes. Air bubbles were expelled out of the system before fixing the unit horizontally on table.
- 2) The function generator was connected with the PZT disk by using electric wires.
- 3) The mode of signal was selected as sinusoidal via the control panel of the function generator. The peak-to-peak voltage of the sinusoidal signal was set at 0.5 V.
- 4) After the signal output was turned on, the CCD camera was used to record the displacement of the centre point of water/air interface (h) varying with time (t).

Thereafter, the frequency of the sinusoidal signal (f) was adjusted (0.2 Hz, 0.4 Hz, 0.6 Hz, 0.8 Hz, 1 Hz), and the measurement was repeated to record the displacement of the water/air interface and time for each frequency.

- 5) The displacement of the centre point of the water/air interface was plotted versus time, after processing the video captured by the CCD camera. Figure 6.5 has shown that the displacement of the centre point of the water/air interface was plotted versus time for the frequency of 0.6 Hz. It can be seen that the displacements of the centre point versus time well fit the sine fitting curve. Thus, the displacement of the water/air interface (h) at different time can be approximated as

$$h_{os} = h_{amp} \sin(2\pi ft) \quad (6.2)$$

where h_{amp} is the amplitude of the displacement, f is the frequency of the oscillation (unit: Hz) which is taken as the same as the frequency of the driving signal (sinusoidal) in this study, and t is the time (Unit: s).

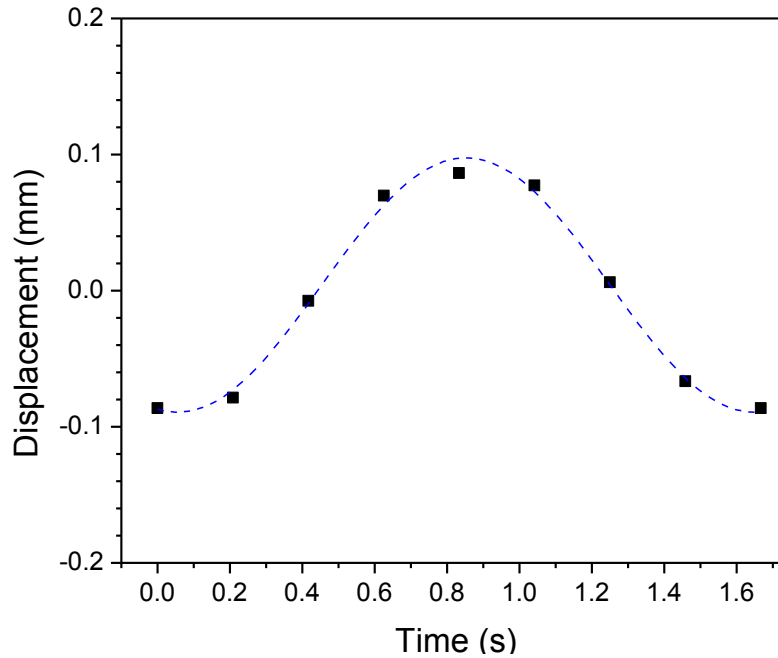


Figure 6.5 Displacement of the centre point of the water/air interface versus time. Solid squares (■) denote the measured data, and dot line indicates the sine curve fit. Data were obtained with the sinusoidal signal of peak-to-peak voltage, 0.5 V, and frequency, 0.6 Hz.

With the displacement of centre point of the water/air interface measured in the experiments, the average velocity of the water/air interface at different time can be described by

$$\bar{u}_{os} = \frac{dh_{os}}{dt} = \bar{u}_{amp} \cos(2\pi ft) \quad (6.3)$$

where h_{os} is the displacement of the centre point of the water/air interface at different time (t), f is the frequency of the oscillation, \bar{u}_{amp} is the amplitude of the average velocity of the water/air interface and can be determined by

$$\bar{u}_{amp} = 2\pi f \cdot h_{amp} \quad (6.4)$$

Thus, the volume flow rate of the oscillatory flow (Q_{os}) can be estimated as

$$Q_{os} = A \cdot \bar{u} = Q_{amp} \cos(2\pi ft) \quad (6.5)$$

$$Q_{amp} = A \cdot \bar{u}_{amp} = \frac{\pi d^2}{4} \cdot 2\pi f h_{amp} \quad (6.6)$$

where A is the cross-section area of the glass capillary, d is the glass capillary diameter (0.335 mm), Q_{amp} is the amplitude of the average volume flow rate of the oscillatory flow. Based on the measurement data, the amplitude of the average volume flow rate is plotted versus oscillation frequency in Figure 6.6. It can be seen that the amplitude of the volume flow rate of the oscillatory flow is about 0.09 mL/h for different oscillation frequencies from 0.2 Hz to 1 Hz.

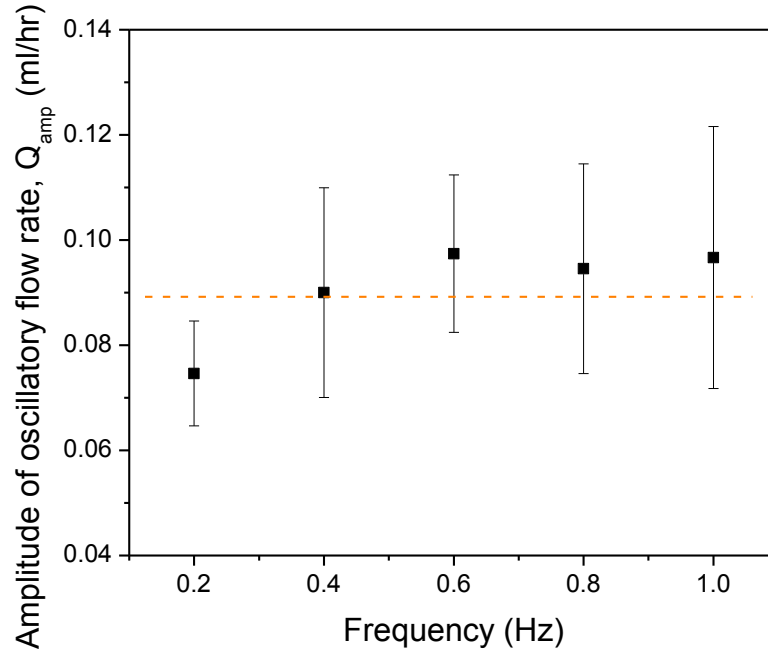


Figure 6.6 Amplitude of the volume flow rate of the oscillatory flow (Q_{amp}) versus the oscillation frequency (f). Experiments were conducted with constant voltage of the sinusoidal signal to the PZT disk ($V_{pp} = 0.5$ V). Dot line represents the average value of the amplitude of oscillatory flow rate.

6.2.2 EXPERIMENTAL PROCEDURES

To conduct the experiments with hydrodynamic flow, the general procedures are similar to those introduced in Section 4.1.2:

- 1) The microchannel chip was cleaned in with DI water ultrasonic cleaner for about 2 hours. The sample fluids (polystyrene particle, diameter: 930 nm) with *NaCl* solution (5×10^{-4} M) were homogenized in an ultrasonic bath before loading into the syringe.
- 2) The temperature of water bath and flow rate of hot water were set to the designed values via the control panels of water bath and syringe pump, respectively. The microchip was connected to the syringes and water bath with silicon tubes. The laser was turned on to warm up for about 10 minutes.
- 3) The captured area of interest ($597 \times 436 \mu\text{m}^2$) was fixed at the centre point of the deposition channel in the longitude direction. The CCD camera was switched on and its exposure time was set as 1s.
- 4) For experiments with steady flow, the volume flow rate of sample fluid was set to the designed values (0.01 ml, 0.025 mL/h, 0.05 mL/h, 0.1 mL/h, 0.5mL/h, 1 mL/h, 2 mL/h) for each test, via the control panel of the sample syringe pump.
- 5) For experiments with pulsatile flow, the piezoelectric disk was connected to the function generator with electric wires. The volume flow rate of sample fluid was set as constant at 1 mL/h. To generate different vibrations of piezoelectric disk, the frequency and amplitude of the sinusoidal signal were set to the designed values via the function generator. The frequency was varied from 0 Hz to 1 Hz with fixed amplitude of the PZT at 0.5 V (peak-to-peak voltage).
- 6) Sequences of image were taken with a time interval of five minutes. At the first 15 minutes, images were taken without supplying hot water in order to provide a reference result at room temperature. Thereafter, hot water was continuously supplied to the heating channel with the constant flow rate.

- 7) After 90 minutes, the experiment was finished, and all the images were stored in computer for analysis. A software “Image Pro Plus” was employed to process the images of particle deposition by counting the number of deposited particles within the area of interest.

After completing the deposition measurements for a given system setting, the static dimensionless deposition rate, Sherwood number, can be computed as

$$\text{Sh}_{\text{exp}} = \frac{J_{\text{exp}}}{D_{\infty} n_{\infty, p} / a_p} \quad (6.7)$$

where J_{exp} is the measured particle deposition flux onto the bottom surface of the deposition channel, $n_{\infty, p}$ is the particle concentration of the bulk fluid, a_p represents the average particle radius of the sample. D_{∞} denotes the diffusion coefficient in bulk fluid which can be determined by the Stokes-Einstein equation. More details can be found in Section 4.1.2.

To evaluate the effect of pulsatile flow on particle deposition, the normalized particle deposition rate ($\overline{\text{Sh}}$) is computed as

$$\overline{\text{Sh}} = \frac{\text{Sh}}{\text{Sh}_0} \quad (6.8)$$

where Sh_0 denotes the Sherwood number for steady flow (1 mL/h) without oscillatory component, Sh represents the Sherwood number for pulsatile flow with oscillatory component. If the value of normalized particle deposition rate is smaller than 1, it means that particulate fouling can be mitigated by the pulsatile flow.

6.2.3 UNCERTAINTY ANALYSIS IN MEASUREMENTS

In this study, the uncertainty of the Sherwood number in experiments arises from three sources: the number of deposited particles, the measured observation area and the duration of the test. The uncertainty of the number of deposited particles is estimated based on the standard deviation of the counted deposited particle numbers for all of the repeated tests, which gives an

uncertainty within 21% (shown as the error bar in the figures in Section 6.4). The accuracy of measuring the area of observed region and duration of experiment are about $1 \mu\text{m}^2$ and 1 s, respectively. The measurement uncertainties of the area of the observed region and experiment duration are about 0.000384% and 0.019%. Overall, the relative uncertainty for the experimental Sherwood number measured in the present study is approximated within 21%. In addition, the accuracy of the temperature measurement is about 0.2°C in this study base on results of temperature uniformity test by using micro-thermocouples. The current and voltage were measured by the multiple-meter with estimated errors of 0.01A and 0.1V, respectively according to the manual of the multiple-meter. The accuracy of the flow rate is determined by the syringe pump (KDS 210, USA), giving a value of 1%.

6.3 THEORETICAL MODELLING

In Chapter 3, the one-dimensional mass transport equation with consideration of thermal effect has been derived on the basis of the modified DLVO theory for the particle deposition in microchannels at elevated temperatures. This model is employed in this chapter to analyse the effect of hydrodynamic flow on the particle deposition in microchannels for steady flow.

For particles suspended in a hydrodynamic flow, the forces exerted on the particles consist of electric double layer force (shown in Eq. 3.25), van der Waals force (shown in Eq. 3.37), gravity (shown in Eq. 3.44) and hydrodynamic lift force induced by hydrodynamic flow. In this study, the dimensionless lift force is approximated as

$$\bar{F}_L = \frac{S_1 a_p}{k_B T_0} (2a^+)^{S_2} \rho_l v^2 \quad (6.9)$$

where a^+ is the dimensionless particle radius, v is the kinematic viscosity of the fluid (DI water), ρ_l indicates the density of fluid (DI water), k_B is the Boltzmann constant, and T_0 depicts the reference temperature, a_p is the radius of the particle. The coefficients, S_1 and S_2 , are referred to

the published works by Hall (1988) and Saffman (1965). The positive signs on the right hand side of Eqs. (6.9) indicate the lift force and its potential are repulsive to prevent particle deposition.

The lift potential (\bar{V}_L) can be obtained by integrating the lift force with the separation distance (H) at different temperatures as

$$\bar{V}_L = \frac{S_1 a_p}{k_B T_0} (2a^+)^{s_2} \rho_l v^2 H. \quad (6.10)$$

The viscosity (μ) and density (ρ_l) of DI water at different temperatures are obtained from the published data sheet as shown in Table 3.2 (Maidment 1993, Wagner and Pruß 2002). As a result, the hydrodynamic lift force at different temperatures can be computed with the corresponding fluid properties at elevated temperatures, and can be substituted into the mass transport equation for solutions of the particle deposition rate.

The dimensionless particle number concentration (\bar{n}) is computed by solving the one-dimensional mass transport equation shown in Eq. (3.20) with the two boundary conditions shown in Eqs. (3.21-3.22). In this study, a software Comsol Multiphysics (V.4.2) is adopted to numerically solve the mass transport equation with an iterative equation solver. Computational test are conducted to estimate the influence of H_0 on the numerical results. It is found that the numerical results are not affected significantly by the specific value of the integration limits as long as $H_0 \leq 0.005$ and $H_\infty \geq 20$. Thus, the lower and upper integration limits are taken as $H_0 = 0.001$ and $H_\infty = 100$, respectively.

With the solved dimensionless particle number concentration distribution (\bar{n}), the dimensionless particle deposition rate onto the channel surface ($H = H_0$) is calculated as

$$Sh_{num} = \frac{j_0}{(D_\infty n_\infty / a_p)} = -f_1(H_0) \left(\frac{d\bar{n}}{dH} \right)_{H=H_0} \quad (6.11)$$

where $f_1(H)$ is the universal hydrodynamic correction coefficient.

The dimensionless concentration (\bar{n}) and Sherwood number (Sh_{num}) for given experimental conditions can be calculated with the parameters listed in Table 4.2. Details can be found in

Section 4.2. Finally, the Sherwood number (Sh) will be used to compare with the experimental results, and gain more insights of the hydrodynamic effect on the particle deposition in microchannels in the following sections. The total interaction potential (\bar{V} shown in Eq. (3.18)) will be plotted versus the dimensionless separation distance ($H = h/a_p$), also known as the interaction potential curve of particle deposition. This interaction potential curve will be implemented to qualitatively analyse the experimental results in the following sections.

6.4 RESULTS AND DISCUSSION

In this section, studies on steady flow and pulsatile flow at elevated temperatures are presented. First, the effects of flow rates (0.01 mL/h ~ 2 mL/h) on particle deposition are observed and discussed for a steady flow at elevated temperatures. The experimental results are compared with the numerical results from the modelling. Next, the results for pulsatile flow are presented, for a constant steady flow component (1 mL/h) and four different oscillatory flow components with frequencies of 0.2 Hz, 0.4 Hz, 0.6 Hz, 0.8 Hz and 1 Hz. The effects of the oscillation frequency on particle deposition are discussed by comparing with the results in steady flow at elevated temperatures.

6.4.1 EFFECT OF FLOW RATE OF PARTICLE SOLUTION (STEADY FLOW)

Flow rate of particle solution (steady flow)

In order to investigate the hydrodynamic effect on the particle deposition in microchannels at elevated temperatures, particle solutions with different volumetric flow rates are supplied by the syringe pump into the microchannel. The volumetric flow rate of particle solution (V') was varied from 0.01 mL/h to 2 mL/h while the solution temperature and electrolyte concentration were maintained at 324.85 K and 5×10^{-4} M, respectively. The number of deposited particles per unit

area observed in experiments is plotted versus time for different sample flow rates shown in Figure 6.7. The number of deposited particles per unit area is increased with time, and its final value is strongly affected by the sample flow rate after 90 minutes. Fewer particles are found to deposit onto the channel surface with higher flow rates.

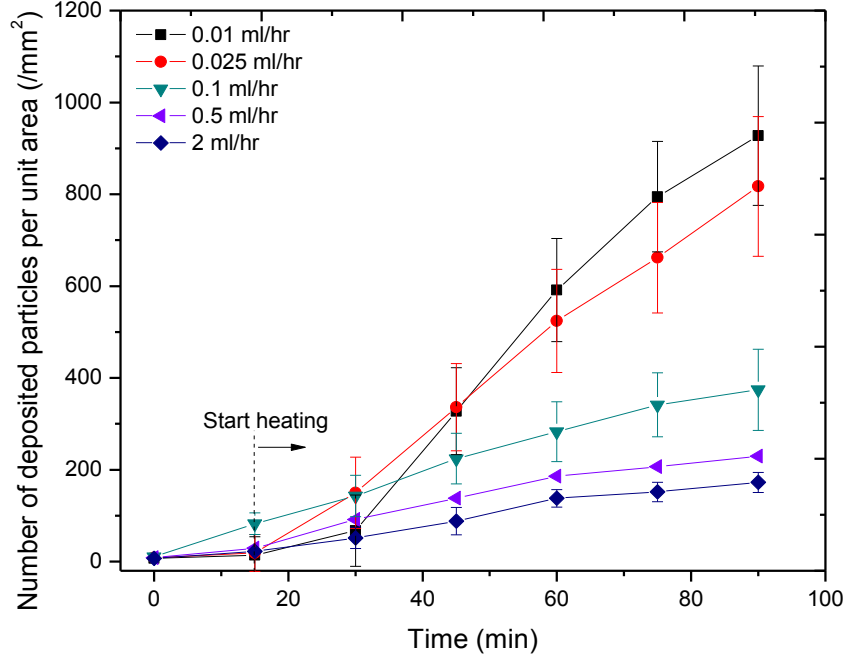


Figure 6.7 Number of deposited particles per unit area versus time for different sample flow rates inside the microchannel (0.01 mL/h, 0.025 mL/h, 0.1 mL/h, 0.5 mL/h, 2 mL/h) Data are for fluorescent polystyrene particles dispersed in *NaCl* solution (5×10^{-4} M). The solution temperature is kept at 324.85 K.

Figure 6.8 shows the dimensionless particle deposition rates (Sh_{exp}) measured in experiments versus the Reynolds number. The Reynolds number is defined as

$$Re = \frac{\rho_l U_{avg} L}{\mu} \quad (6.12)$$

where ρ_l is the water density, L is the hydraulic diameter of the microchannel (533 μm), μ is the dynamic viscosity of the sample solution. U_{avg} is the average flow velocity defined as

$$U_{avg} = \frac{V'}{A} \quad (6.13)$$

where V' refers to the volumetric flow rate of the sample fluids and A is the cross-section area of the deposition channel. The corresponding Reynolds number for the tested flow rates in experiments are calculated based on Eqs. (6.12-6.13) and shown in inset of Figure 6.8.

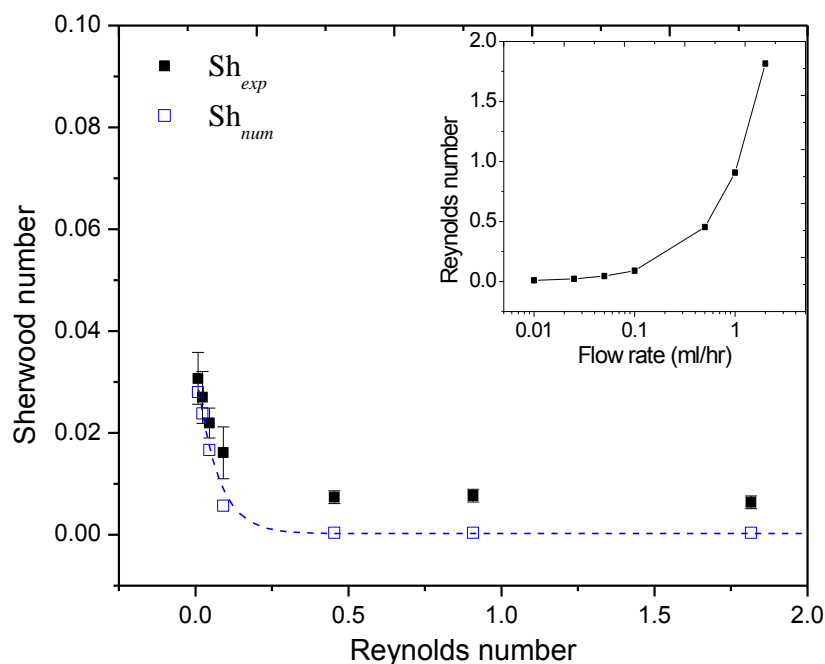


Figure 6.8 Dimensionless static deposition rate (Sherwood number) versus the Reynolds number of the sample flow. Solid squares (■) indicate the measured Sherwood number Sh_{exp} shown in Eq. (6.7) from experiments, and empty squares (□) show the calculated Sherwood number Sh_{num} by Eq. (6.11) from modelling. The dotted line shows the least-square fitting line. Inset shows the Reynolds numbers of the sample fluid as a function of the sample flow rates. Data are for fluorescent polystyrene particles dispersed in stationary *NaCl* solution (5×10^{-4} M). The solution temperature is kept at 324.85 K.

It can be clearly seen from Figure 6.8 that the particle deposition rate (Sherwood number) in the microchannel at elevated temperatures is strongly dependent on the Reynolds number. When the Reynolds number is increased from 0.009 to 0.091, the Sherwood number measured in experiments is steeply reduced from 0.031 to 0.016 and almost remains unchanged with further increasing the Reynolds number to 1.82. The reduction of particle deposition rate can be attributed to augment of the repulsive hydrodynamic lift force by increasing the Reynolds number of the sample fluid flow. Given a fixed solution temperature and electrolyte concentration of the sample fluid, various forces (van der Waals force, electric double layer force and gravity) acting on particles remain unchanged while the repulsive hydrodynamic lift force is appreciably increased by increasing the flow rate. As a result, it is difficult for particles to overcome the resistance induced by the hydrodynamic flow, in order to approach the channel surface. When the Reynolds number is further increased more than 0.091, the repulsive hydrodynamic interaction

could be increased beyond a threshold value. The particles in bulk phase might be kept being pushed away from the channel wall, and cannot deposit onto the surface.

The calculated results of Sh_{num} from modelling are computed for various Reynolds numbers based on Eq. (6.11), and are presented in Figure 6.8. The calculated Sherwood number Sh_{num} shows a similar trend with the measured data Sh_{exp} in experiments. A fair agreement in the same magnitude can be found between Sh_{exp} and Sh_{num} for the range of low Reynolds number ($Re \leq 0.091$), though a discrepancy is observed for the high Reynolds number region ($Re > 0.091$). The results suggest that the hydrodynamic effect on the particle deposition in microchannels at elevated temperature can be approximately described by the proposed model derived on the basis of the modified DLVO theory. Moreover, it is noted that the measured Sherwood numbers in experiments are constantly higher than the corresponding calculated Sherwood number in simulation, especially for high flow rate range ($Re > 0.091$). The discrepancy between the experimental and numerical results is likely caused by lack of accurate mathematical expression for hydrodynamic lift force in microfluidics and the neglected influence of convection in the longitude direction of channel (x axis) as assumed in Chapter 3. The numerical results demonstrate that the hydrodynamic conditions overwhelmingly controlled the particle deposition in microchannels at elevated temperatures. Increasing hydrodynamic intensity, such as the flow rate or Reynolds number, can be an option to mitigate the particle deposition in microchannels at elevated temperatures.

Interaction potential curve

In order to better understand the effect of hydrodynamic interactions on the particle deposition at elevated temperatures, the total particle-channel interaction potential (\bar{V}) is calculated based on Eq. (3.18), and is plotted versus the dimensionless separation distance H shown in Figure 6.9. It can be clearly seen in Figure 6.9-b that the energy barrier in the PEM region does not change noticeably with increasing the Reynolds number of the sample flow. Besides, the total interaction potential presents an additional barrier at large distance ($H \sim 10$) for

high Reynolds number cases ($Re > 0.091$) as shown in Figure 6.9-a. This additional barrier is caused by the strong repulsive hydrodynamic interaction (F_L), because the hydrodynamic lift force acts in a relatively long range compared with the colloidal forces. The hydrodynamic lift force would mainly influence the transport of particles from bulk fluid to the near-wall region. As shown in Figure 6.9-b, the interaction potential at $H = 10$ is increased from -0.3 to 11.6 with increasing the Reynolds number from 0.009 to 1.82. It should be noted that the sign of interaction potential is changed from negative to positive. In other words, the overall effect of interaction between the particle and channel surface is changed from attractive to repulsive with increasing the Reynolds number. The positive total interaction potential with high Reynolds numbers ($H = 10$) could impede particles approaching the channel surface at closer distance. Meanwhile, the mobility of particles could be reduced by the particle-wall hydrodynamic interaction. As a result, the particles could rarely overcome the energy barrier to deposit onto the channel surface, leading to the reduction of the particle deposition rate observed in the experiments. Especially, the repulsive potential of lift force is comparable with the energy barrier in the near-wall region for high Reynolds numbers ($Re > 0.091$). As such, the repulsive interaction is so strong that particles could be pushed away from the channel surface. Consequently, the deposition rate is maintained at a low value with no further change by increasing the Reynolds number ($Re > 0.091$) shown in Figure 6.8.

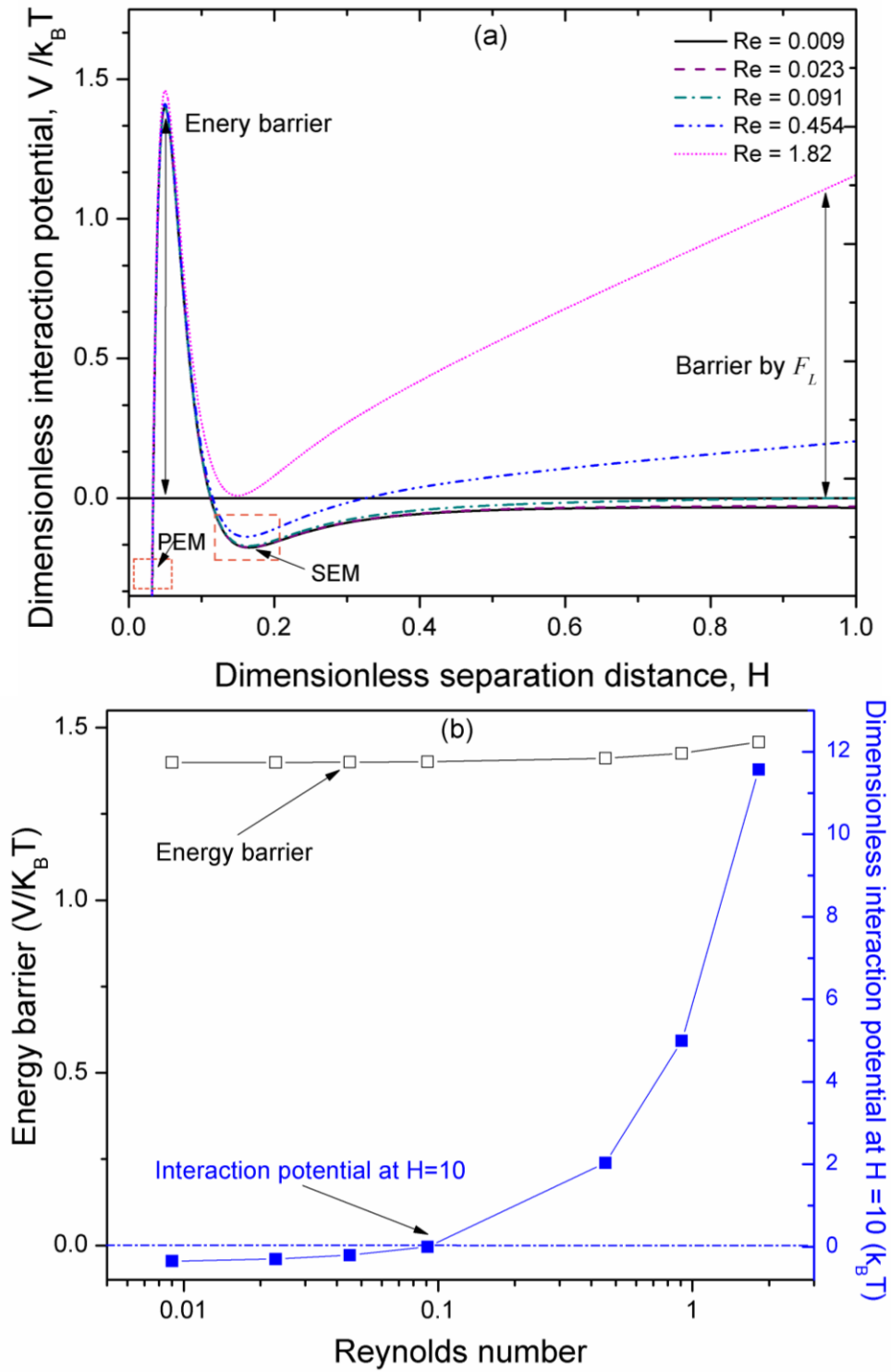


Figure 6.9 (a) Dimensionless particle-microchannel interaction potential \bar{V} versus the dimensionless separation distance H for different Reynolds number of the sample flow. (b) The energy barrier (shown by \square) and the interaction potential at $H = 10$ (shown by \blacksquare) as a function of the Reynolds number of the sample flow. Data are calculated based on Eq. (3.18) for fluorescent polystyrene particles dispersed in a $NaCl$ solution (5×10^{-4} M). The solution temperature is kept at 324.85 K. The dotted square SEM indicates the secondary energy minimum region, and the dotted square PEM indicates the primary energy minimum region.

Effect of bulk solution temperature with hydrodynamic flow

To examine the effect of bulk solution temperature with a hydrodynamic flow, the solution temperature was varied from room temperature (297.25 K) to 339.25 K while sample flow rate was fixed at 0.1 mL/h ($Re = 0.091$) and the electrolyte concentration was 5×10^{-4} M. Figure 6.10 shows the number of deposited particles per unit area changing with time. It can be clearly seen that particles deposit much faster with high temperature (339.25 K) than the room temperature case (297.25 K) after heating is on (starting from 15 minutes). After 90 minutes, the number of deposited particle per unit area is $1077/\text{mm}^2$ at 339.25 K, which is about three times larger than $265/\text{mm}^2$ at the room temperature (297.25 K).

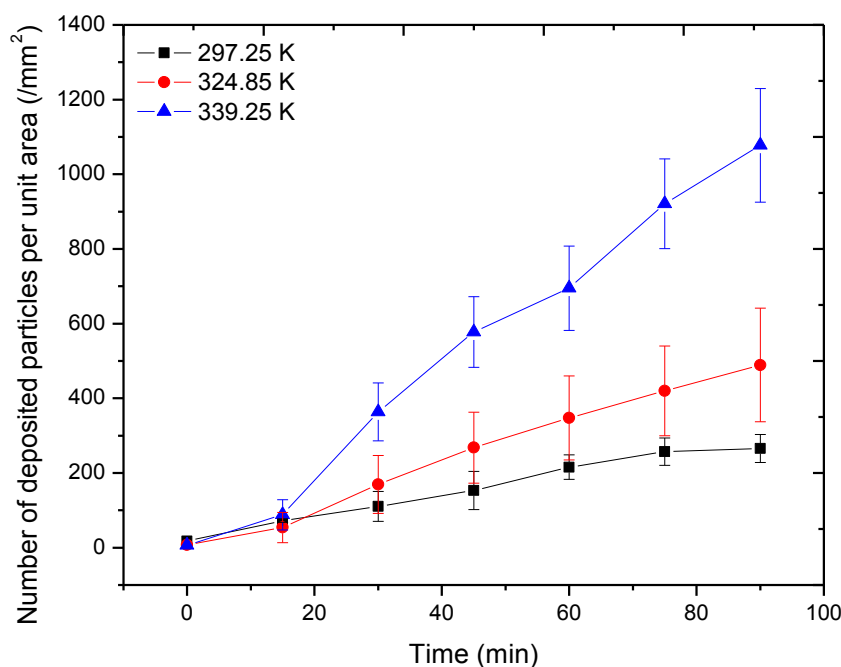


Figure 6.10 Number of deposited particles in area of interest versus time for different solution temperature in a hydrodynamic flow. Data are for fluorescent polystyrene particles dispersed in *NaCl* solution (5×10^{-4} M) while the sample flow rate is fixed at 0.1 mL/h ($Re = 0.091$).

The dimensionless static particle deposition rates measured in experiments (Sh_{exp}) for different solution temperatures are presented in Figure 6.11. The calculated particle deposition rate (Sh_{num}) is solved from modelling with given experimental conditions, and is presented in Figure 6.11. It can be seen that both the measured and calculated Sherwood numbers are monotonically increased with solution temperature. The enhancement of particle deposition is

attributed to the augmented attractive interactions (van der Waals force and gravity) and attenuated repulsive interactions (electric double layer force) with increasing the solution temperature for a given sample flow rate. Besides, the hydrodynamic lift force is also reduced because of the reduction of the viscosity of water at elevated temperatures. Consequently, the repulsive energy barrier for particle deposition is reduced so that more particles can overcome the barrier to attach onto the channel surface.

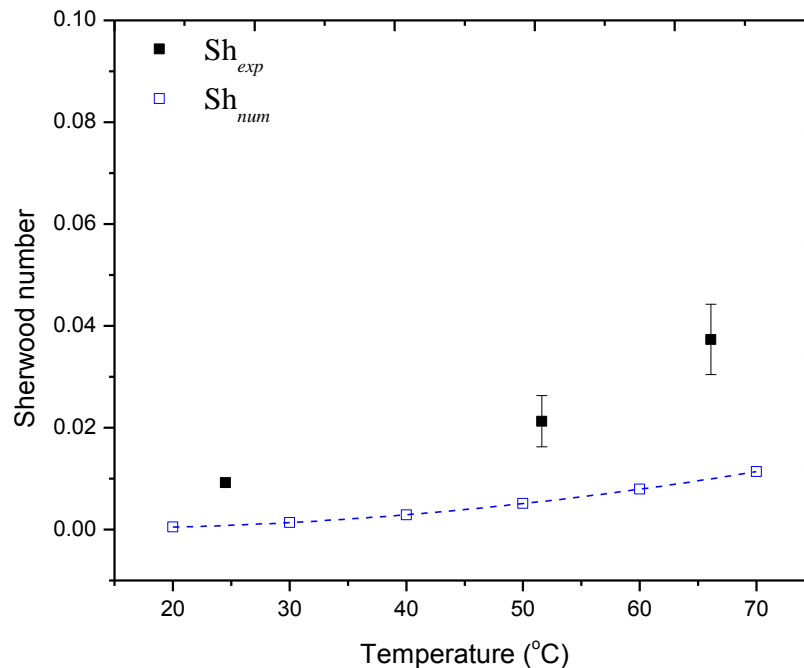


Figure 6.11 Dimensionless static deposition rate (Sherwood number) as a function of the temperature of solution at three different temperatures, 297.25 K, 324.85 K and 339.25 K. Solid squares (■) indicate the measured Sherwood number Sh_{exp} shown in Eq. (6.7) from experiments, and empty squares (□) show the calculated Sherwood number Sh_{num} shown in Eq. (6.11) from modelling. The dotted line shows the least-square fitting line. Data are for fluorescent polystyrene particles dispersed in a *NaCl* solution (5×10^{-4} M) while the sample flow rate is fixed at 0.1 mL/h ($Re = 0.091$).

It is noted from Figure 6.11 that the numerical solutions of Sh_{num} demonstrates a similar trend with the experimental observations in the same magnitude. Besides, the measured Sherwood numbers in experiments are constantly higher than the corresponding calculated Sherwood number in simulation. The discrepancy between the experimental and numerical results could result from lack of accurate mathematical expressions for zeta potentials at elevated temperatures, hydrodynamic lift force in microfluidics, and the neglected influence of convection in the longitude direction of channel (x axis). However, the trend of the varying particle deposition rates

with the solution temperatures in a hydrodynamic flow is well demonstrated by the proposed model with the given conditions from the experiments.

6.4.2 EFFECT OF FLOW OSCILLATION FREQUENCY (PULSATILE FLOW)

In Section 6.4.1, the results show that the particle deposition at elevated temperature can be mitigated by increasing the flow rate of the sample fluids. The experimental results show that the reduction of the particle deposition rate is insignificant by increasing flow rate above 0.5 mL/h. Besides, increasing flow rate of sample fluids may not be a desired option for particle deposition mitigation for practical microfluidic applications, because higher flow rates would result in more energy consumption of pump and larger mechanic stress exerted upon microchannel structures in practical applications.

In this section, pulsatile flow is suggested as a potential solution to further mitigate particle deposition at elevated temperatures in the microchannel. The particle deposition rates with pulsatile flow are measured experimentally, for a constant steady flow component (1 mL/h) and five different flow oscillation frequencies of 0.2 Hz, 0.4 Hz, 0.6 Hz, 0.8 Hz and 1 Hz. The effects of flow oscillation frequency on particle deposition are discussed by comparing with the results in steady flow at elevated temperatures. In the present study, the amplitude of the sinusoidal AC signal is maintained as constant at 0.5 V. As shown in Figure 6.6, the average amplitude of the volume flow rates of the oscillatory flow is 0.09 mL/h (Q_{amp}) for different flow oscillation frequencies, which are much smaller than the volume flow rate of the steady flow component, 1 mL/h. The oscillatory component of the pulsatile flow is much weaker than the steady component. Thus, no reversing flow can occur in the microchannel.

The normalised particle deposition rate (\overline{Sh} in Eq. 6.8) is plotted against the flow oscillation frequency in Figure 6.12. It can be seen that the normalised deposition rate is observed to be generally reduced from 1 for the steady flow to 0.52 for the pulsatile flow with oscillation

frequency of 1 Hz. In other words, the particle deposition in microchannels at elevated temperatures can be mitigated by a small pulsation in the hydrodynamic flow. The particle deposition rate is reduced with increasing the flow oscillation frequency while the steady flow component and amplitude of pulsation are kept as constants. The observed reduction could be attributed to the small disturbance generated by the oscillatory component of the pulsatile flow. Compared with the steady flow, the oscillatory component of the pulsatile flow could induce additional resistance for particle deposition, and cause the reduction of particle deposition onto the channel surface. The resistance could be enhanced with the flow oscillation frequency. Similar phenomena have been found in the theoretical works by Moschandreou et al. (2010). They claimed that the mass transport rate to the wall for a pulsatile flow was reduced by increasing the frequencies within a low range (beginning from zero).

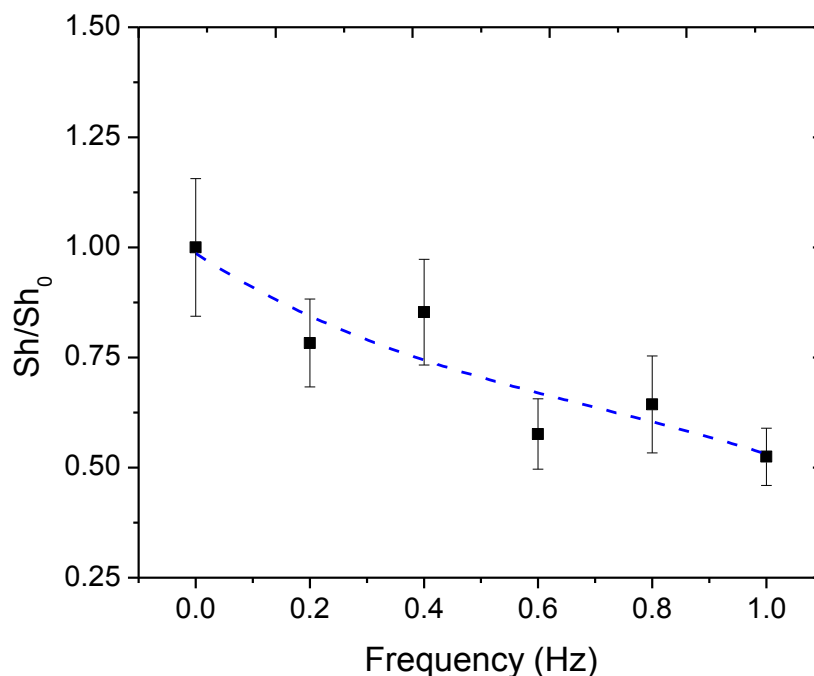


Figure 6.12 The normalised particle deposition rate Sh/Sh_0 in Eq. (6.8) versus the flow oscillation frequency for the microfluidic flow. Data are for the PMMA microchannel and the polystyrene microparticles (Diameter: 930 nm) suspended in a $NaCl$ solution (5×10^{-4} M). The flow rate of the steady flow is maintained at 1 mL/h, and the solution temperature is kept at 51.6 °C. The amplitude of the PZT disk is fixed at 0.5 V and the average amplitude of the flow oscillation (Q_{amp}) is 0.09 mL/h. The dotted line represents the least-squares fitting curve.

The results in this study suggest that the particle deposition at elevated temperatures can be further mitigated by applying a pulsatile flow, superimposing a small oscillatory component into

the steady flow. The pulsatile flow implemented in this study is a flow with low frequencies (≤ 1 Hz) and small amplitudes (0.5 Vpp). Compared with the conventional mitigation approach by increasing the flow rate of the sample solution, the pulsatile flow could cost less energy consumption, and exerts smaller stress on the microchannel. These advantages make the pulsation be a possible solution for the particle deposition in microchannel at elevated temperatures.

6.5 SUMMARY

In this chapter, the effect of hydrodynamic flow on particle deposition at elevated temperatures has been experimentally investigated in a microfluidic system incorporated with a designed pulsation generation unit. Two types of flow have been studied experimentally, including steady flow and pulsatile flow.

With a given solution temperature and an electrolyte concentration, the dimensionless static particle deposition rate (Sh) is overwhelmingly influenced by the flow rate of the steady flow (Reynolds number). The Sherwood number is reduced with the Reynolds number and changes insignificantly for Reynolds number beyond 0.091 (0.5 mL/h) within the tested range. The observed reduction of particle deposition rate with Reynolds number is due to fact that the augment of hydrodynamic lift force prevents the transport of particles from bulk solution to the near-wall region where the colloidal interactions dominate. Increasing hydrodynamic intensity, such as the flow rate or Reynolds number, can be used to mitigate the particle deposition in microchannels at elevated temperatures.

A controllable pulsatile flow has been generated by regulating the vibration of piezoelectric disk embedded in the designed pulsation generation unit. The normalised particle deposition rate is calculated by comparing the Sherwood numbers of the pulsatile flow and that of the steady flow. Based on the preliminary experimental results, the pulsatile flow has considerable influence on the particle deposition rate in microchannels at elevated temperatures. The normalised particle deposition rate is reduced significantly as the frequency is increased from 0 Hz to 1 Hz, while the

steady flow component and the amplitude of driving signal are kept as constants at 1 mL/h and 0.5 V, respectively. The results suggest that pulsatile flow can be a potential option for the particle deposition mitigation in microchannels at elevated temperatures. The physical mechanism of the particle deposition mitigation with pulsatile flow in microchannels at elevated temperature is recommended for future study.

Chapter 7

Conclusions and Recommendations

Following the objectives of this study, the thermal effects of particle deposition in microchannels at elevated temperature have been investigated by both experimental characterisation and theoretical modelling. The important findings in the present study are concluded in this chapter. Recommendations are made for future study based on the results obtained in this study.

7.1 CONCLUSIONS

Two crucial thermal parameters for particle deposition at elevated temperature, bulk solution temperature and temperature gradient, have been investigated using a microfluidic approach in this study. Both experimental characterisation and theoretical modelling have been performed to examine the effects of bulk solution temperature and temperature gradient. Besides, the effect of hydrodynamic flow in the microchannel has been investigated by applying two types of flow, the steady flow and the pulsatile flow. The main conclusions from the present study are drawn as follows:

- 1) A microfluidic device was designed and fabricated to provide various bulk temperatures for particle deposition experiments. The dynamic process of particle deposition in the microfluidic device has been directly observed within a wide range of bulk solution temperatures, from room temperature (297.25 K) to 339.25 K. To the best knowledge of the author, it is the first time that the thermal effect (bulk temperature) on the particle deposition in microchannels is studied. The particle deposition rates onto the microchannel surface, which is characterised by the Sherwood number, are found to be strongly dependent on the solution temperature. For both stationary and flowing samples,

the particle deposition rates are higher with increasing the bulk solution temperature. Significant enhancement of the particle deposition rate up to 300% is found with increasing the bulk solution temperature from 297.25 K (room temperature) to 339.25 K. With a fixed elevated temperature, the Sherwood number is monotonically increased with increasing the electrolyte concentration of sample solution.

- 2) Theoretical modelling within the framework of the DLVO theory has been derived for particle deposition at elevated temperatures, based on a simplified one-dimensional mass transport model with consideration of the temperature dependence of the physiochemical properties involved in the particle deposition process. The modelling results agree qualitatively with the experimental measurements in terms of the particle deposition rate (Sherwood number) at various bulk solution temperatures. The modelling also provides the interaction potential curves between the particles and the microchannel surface at elevated temperatures. The bulk solution temperature determines the energy barrier impeding the particle attachment in the near-wall region, with a given electrolyte concentration and hydrodynamic flow conditions. The repulsive energy barrier is remarkably reduced with increasing the bulk solution temperature, leading to the enhanced particle deposition observed in experiments.
- 3) A new design of microfluidic temperature-gradient microchip has been developed, and the microfluidic chip consists of three layers: a top layer using with a thermoelectric (TEC) unit as cooler, a middle layer with a PDMS microchannel, and a bottom layer using a transparent Indium tin oxide (ITO) coated glass as heater. This design allows one for direct observation of the dynamic particle deposition along the same direction as the applied temperature gradient, which provides an effective microfluidic platform for investigating the particle-surface interaction phenomena under non-equilibrium thermal environments. Experiments have been conducted to study the particle deposition rate with different temperature gradients. The results show that the Sherwood number is decreased by 56%, with increasing the temperature gradients inside microchannel from 78.9 K/m to

6946.9 K/m. The mechanism of temperature gradient effect has been analysed by using a derived one-dimensional model. The modelling results show that the temperature gradient affects the transport of particles at long range via the thermophoretic force acting on particles, while the bulk solution temperature determines the energy barrier to hinder the particle attachment in the near-wall region. The observed reduction of particle deposition rate with increasing temperature gradient is due to the combined effects of the temperature gradient and the bulk solution temperature on the two steps of particle deposition process, including the particle transport and the particle attachment.

- 4) The effects of hydrodynamic flow on the particle deposition at elevated temperatures have been studied with consideration of a steady flow and a pulsatile flow in the microchannel. For the steady flow, the Sherwood number is reduced with increasing the Reynolds number of the hydrodynamic flow and its value is maintained at a minimum within the tested range ($Re: 0.009 - 1.82$). The reduction of particle deposition rate with increasing the Reynolds number is due to fact that the augment of hydrodynamic lift force prevents the transport of particles from the bulk solution to the near-wall region where the colloidal interactions dominate. For the pulsatile flow, a microfluidic pulsation generation unit embedded with a piezoelectric (PZT) disk is designed to superimpose a controllable oscillatory flow component in the main steady flow. The effect of the flow oscillation frequency on the particle deposition rate has been experimentally studied. By comparing the Sherwood numbers for the steady flow and the pulsatile flow with different oscillation frequencies, the results show that the normalised particle deposition rate is reduced by 50% as the frequency is increased from 0 Hz to 1 Hz, while the steady flow rate (1 mL/h) and the amplitude of the flow oscillation (0.09 mL/h) are fixed. This simple design and low energy consumption make the pulsatile flow as a potential option for mitigating particle deposition in microfluidic applications at elevated temperatures.

7.2 RECOMMENDATIONS

This thesis has presented the thermal effects on particle deposition in microchannels for the first time. Based on the results obtained in the present study, the following are recommended for future work:

- 1) The current study shows the thermal effects on the particle deposition for a dilute particle suspension, in which the interactions among the particles are neglected. As many practical applications involve concentrated particle suspensions, it would be important to investigate the particle deposition in microchannels at elevated temperatures for different particle concentrations.
- 2) Discrepancy between the experimental results and the numerical results has been found for the cases of the elevated temperatures and the electrolyte solutions. The dependence of particle deposition on the temperature and the electrolyte concentration needs to be further studied for the colloidal interactions (i.e. the electric double layer force and the van der Waals force).
- 3) The experiments with the hydrodynamic flow at elevated temperatures have shown that the particle deposition in a microfluidic flow can be mitigated by varying the hydrodynamic intensity (Reynolds number and flow oscillation) in the microchannel. A further study of the physical mechanisms of the particle-wall interaction in the pulsatile flow would be an interesting topic as the pulsatile flow has been proposed for a number of heat exchanger applications. However, few experimental and theoretical works currently have been reported for the particle deposition in microchannel flows in the literature.

References

- Adamczyk, Z., Dabros', T., Czarnecki, J. and Van De Ven, T. G. M. (1983). "Particle transfer to solid surfaces." Advances in Colloid and Interface Science **19**(3): 183-252.
- Adamczyk, Z. and Van De Ven, T. G. M. (1981). "Deposition of particles under external forces in laminar flow through parallel-plate and cylindrical channels." Journal of Colloid And Interface Science **80**(2): 340-356.
- Adamczyk, Z. and Warszyński, P. (1996). "Role of electrostatic interactions in particle adsorption." Advances in Colloid and Interface Science **63**(0): 41-149.
- Anderson, J. L. (1991). "Colloidal Dispersions. By W. B. RUSSEL, D. A. SAVILLE and W. R. SCHOWALTER. Cambridge University Press, 1989. 525 pp. £60. Colloidal Hydrodynamics. By T. G. M. VAN DE VEN. Academic Press, 1989. 582 pp. £43." Journal of Fluid Mechanics **222**: 692-694.
- Barisik, M., Atalay, S., Beskok, A. and Qian, S. (2014). "Size Dependent Surface Charge Properties of Silica Nanoparticles." The Journal of Physical Chemistry C **118**(4): 1836-1842.
- Becker, M., Mansouri, A., Beilein, C. and Janasek, D. (2009). "Temperature gradient focusing in miniaturized free-flow electrophoresis devices." Electrophoresis **30**(24): 4206-4212.
- Bendersky, M. and Davis, J. M. (2011). "DLVO interaction of colloidal particles with topographically and chemically heterogeneous surfaces." Journal of Colloid and Interface Science **353**(1): 87-97.
- Bernardin, J. D. and Chan, S. H. (1991). Magnetics Effects on Simulated Brine Properties Pertaining to Magnetic Water Treatment. Fouling and Enhancement Interactions,. 28th National Heat Transfer Conference. Minneapolis, Minnesota, USA.
- Bert, R. (2001). "CRC Materials Science and Engineering Handbook (Book Review)." Civil Engineering (08857024) **71**(8): 87.
- Bhattacharjee, S., Chen, J. Y. and Elimelech, M. (2000). "DLVO interaction energy between spheroidal particles and a flat surface." Colloids and Surfaces A: Physicochemical and Engineering Aspects **165**(1-3): 143-156.
- Bott, T. R. (1995). Fouling of Heat Exchangers, Elsevier B. V.
- Bowen, W. R. and Jenner, F. (1995). "Theoretical descriptions of membrane filtration of colloids and fine particles: An assessment and review." Advances in Colloid and Interface Science **56**: 141-200.
- Briscoe, W. H. and Attard, P. (2002). "Counterion-only electrical double layer: A constrained entropy approach." The Journal of Chemical Physics **117**(11): 5452-5464.
- Brzozowska, A. M., Parra-Velandia, F. J., Quintana, R., Xiaoying, Z., Lee, S. S. C., Chin-Sing, L., Jańczewski, D., Teo, S. L. M. and Vancso, J. G. (2014). "Biomimicking Micropatterned Surfaces and Their Effect on Marine Biofouling." Langmuir **30**(30): 9165-9175.

Casimir, H. B. G. and Polder, D. (1948). "The Influence of Retardation on the London-van der Waals Forces." Physical Review **73**(4): 360-372.

Chandra, S. V. J., Uthanna, S. and Rao, G. M. (2008). "Effect of substrate temperature on the structural, optical and electrical properties of dc magnetron sputtered tantalum oxide films." Applied Surface Science **254**(7): 1953-1960.

Chatterjee, R., Bhattacharjee, S. and Mitra, S. K. (2012). "Particle transport in patterned cylindrical microchannels." Microfluidics and Nanofluidics **12**(1-4): 41-51.

Claesson, P. M. and Christenson, H. K. (1988). "Very long range attractive forces between uncharged hydrocarbon and fluorocarbon surfaces in water." The Journal of Physical Chemistry **92**(6): 1650-1655.

de Gennes, P. G. (1987). "Polymers at an interface; a simplified view." Advances in Colloid and Interface Science **27**(3): 189-209.

de Mello, A. J., Habgood, M., Lancaster, N. L., Welton, T. and Wootton, R. C. R. (2004). "Precise temperature control in microfluidic devices using Joule heating of ionic liquids." Lab on a Chip **4**(5): 417-419.

Derjaguin, B. V. (1934). "Analysis of friction and adhesion, IV. The theory of the adhesion of small particles." Kolloid Z. **69**: 155-164.

Derjaguin, B. V. and Landau, E. M. (1941). "Theory of the stability of strongly charged lyophobic sols and of the adhesion of strongly charged particles in solutions of electrolytes." Acta Physicochim **14**: 633-662.

Dzyaloshinskii, I. E., Lifshitz, E. M. and Lev, P. P. (1961). "General Theory of van der Waals' forces." Soviet Physics Uspekhi **4**(2): 153.

Edwards, T. L., Gale, B. K. and Frazier, A. B. (2002). "A microfabricated thermal field-Flow fractionation system." Analytical Chemistry **74**(6): 1211-1216.

Elimelech, M. (1994). "Particle deposition on ideal collectors from dilute flowing suspensions: Mathematical formulation, numerical solution, and simulations." Separations Technology **4**(4): 186-212.

Elimelech, M., Gregory, J., Jia, X. and Williams, R. A. (1995). Particle Deposition & Aggregation: Measurement, Modelling and Simulation. Oxford, Butterworth-Heinemann.

Eslahian, K. A., Majee, A., Maskos, M. and Wurger, A. (2014). "Specific salt effects on thermophoresis of charged colloids." Soft Matter **10**(12): 1931-1936.

Evenhuis, C. J., Guijt, R. M., Macka, M., Marriott, P. J. and Haddad, P. R. (2006). "Variation of zeta-potential with temperature in fused-silica capillaries used for capillary electrophoresis." Electrophoresis **27**(3): 672-676.

Falahati, H., Wong, L., Davarpanah, L., Garg, A., Schmitz, P. and Barz, D. P. J. (2014). "The zeta potential of PMMA in contact with electrolytes of various conditions: Theoretical and experimental investigation." Electrophoresis **35**(6): 870-882.

Frens, G. and Overbeek, J. T. G. (1972). "Repeptization and the theory of electrostatic colloids." Journal of Colloid And Interface Science **38**(2): 376-387.

Genzer, J. and Efimenko, K. (2006). "Recent developments in superhydrophobic surfaces and their relevance to marine fouling: a review." Biofouling **22**(5): 339-360.

Grabbe, A. and Horn, R. G. (1993). "Double-Layer and Hydration Forces Measured between Silica Sheets Subjected to Various Surface Treatments." Journal of Colloid and Interface Science **157**(2): 375-383.

Gregory, J. (1970). "The calculation of Hamaker constants." Advances in Colloid and Interface Science **2**(4): 396-417.

Gu, Y. and Li, D. (2002a). "Deposition of spherical particles onto cylindrical solid surfaces: I. Numerical simulations." Journal of Colloid And Interface Science **248**(2): 315-328.

Gu, Y. and Li, D. (2002b). "Deposition of spherical particles onto cylindrical solid surfaces: II. Experimental studies." Journal of Colloid And Interface Science **248**(2): 329-339.

Gudipaty, T., Stamm, M. T., Cheung, L. S. L., Jiang, L. and Zohar, Y. (2011). "Cluster formation and growth in microchannel flow of dilute particle suspensions." Microfluidics and Nanofluidics **10**(3): 661-669.

Guha, R., Shang, X., Zydney, A. L., Velegol, D. and Kumar, M. (2015). "Diffusiophoresis contributes significantly to colloidal fouling in low salinity reverse osmosis systems." Journal of Membrane Science **479**(0): 67-76.

Guijt, R. M., Dodge, A., van Dedem, G. W. K., de Rooij, N. F. and Verpoorte, E. (2003). "Chemical and physical processes for integrated temperature control in microfluidic devices." Lab on a Chip **3**(1): 1-4.

Gupta, S. K., Patel, T. R. D. and Ackerman, R. C. (1982). "Wall heat/mass transfer in pulsatile flow." Chemical Engineering Science **37**(12): 1727-1739.

Hall, D. (1988). "Measurements of the mean force on a particle near a boundary in turbulent flow." Journal of Fluid Mechanics **187**: 451-466.

Hamaker, H. C. (1937). "The London-van der Waals attraction between spherical particles." Physica **4**(10): 1058-1072.

Hasson, D. and Bramson, D. (1985). "Effectiveness of magnetic water treatment in suppressing calcium carbonate scale deposition." Industrial & Engineering Chemistry Process Design and Development **24**(3): 588-592.

Healy, T. W. and La Mer, V. K. (1964). "The energetics of flocculation and redispersion by polymers." Journal of Colloid Science **19**(4): 323-332.

Hogg, R., Healy, T. W. and Fuerstenau, D. W. (1966). "Mutual coagulation of colloidal dispersions." Transactions of the Faraday Society **62**: 1638-1651.

Horn, R. G. and Israelachvili, J. N. (1981). "Direct measurement of structural forces between two surfaces in a nonpolar liquid." The Journal of Chemical Physics **75**(3): 1400-1411.

Hough, D. B. and White, L. R. (1980). "The calculation of hamaker constants from liftshitz theory with applications to wetting phenomena." Advances in Colloid and Interface Science **14**(1): 3-41.

IAPWS (1997a). Release on the refractive index of ordinary water substance as a function of wavelength, temperature and pressure. Erlangen, Germany, International Association for the Properties of Water and Steam.

IAPWS (1997b). Release on the static dielectric constant of ordinary water substance for temperatures from 238K to 873K and pressure up to 1000 Mpa. Erlangen, Germany, International Association for the Properties of Water and Steam.

Incropera, F. P. and DeWitt, D. P. (2002). Fundamentals of Heat and Mass Transfer. New York, John Wiley & Sons.

Israelachvili, J. N. (1972). "The Calculation of Van Der Waals Dispersion Forces between Macroscopic Bodies." Proceedings of the Royal Society of London A: Mathematical, Physical and Engineering Sciences **331**(1584): 39-55.

Israelachvili, J. N. (1992). Intermolecular and surface forces. Burlington, MA, Academic Press.

Israelachvili, J. N. and Pashley, R. M. (1984). "Measurement of the hydrophobic interaction between two hydrophobic surfaces in aqueous electrolyte solutions." Journal of Colloid and Interface Science **98**(2): 500-514.

Israelachvili, J. N. and Wennerstrom, H. (1997). "Hydration in electrical double layers." Nature **385**(6618): 690-690.

Jiao, Z., Nguyen, N.-T., Huang, X. and Ang, Y. (2007). "Reciprocating thermocapillary plug motion in an externally heated capillary." Microfluidics and Nanofluidics **3**(1): 39-46.

Jiao, Z. J., Huang, X. Y. and Nguyen, N. T. (2008). "Manipulation of a droplet in a planar channel by periodic thermocapillary actuation." Journal of Micromechanics and Microengineering **18**(4): 045027.

Kar, A., Guha, R., Dani, N., Velegol, D. and Kumar, M. (2014). "Particle Deposition on Microporous Membranes Can Be Enhanced or Reduced by Salt Gradients." Langmuir **30**(3): 793-799.

Karamercan, O. E. and Gainer, J. L. (1979). "The Effect of Pulsations on Heat Transfer." Industrial & Engineering Chemistry Fundamentals **18**(1): 11-15.

Kazi, S. (2012). Fouling and fouling mitigation on heat exchanger surfaces, INTECH Open Access Publisher.

Kazi, S. N., Duffy, G. G. and Chen, X. D. (2013). "Fouling mitigation of heat exchangers with natural fibres." Applied Thermal Engineering **50**(1): 1142-1148.

Khandurina, J., McKnight, T. E., Jacobson, S. C., Waters, L. C., Foote, R. S. and Ramsey, J. M. (2000). "Integrated System for Rapid PCR-Based DNA Analysis in Microfluidic Devices." Analytical Chemistry **72**(13): 2995-3000.

- Kim, K. and Chun, M.-S. (2012). "Pulsatile Poiseuille flows in microfluidic channels with back-and-forth mode." Korea-Australia Rheology Journal **24**(2): 89-95.
- Kim, S.-J., Wang, F., Burns, M. A. and Kurabayashi, K. (2009). "Temperature-Programmed Natural Convection for Micromixing and Biochemical Reaction in a Single Microfluidic Chamber." Analytical Chemistry **81**(11): 4510-4516.
- Kirby, B. J. and Hasselbrink, E. F. (2004). "Zeta potential of microfluidic substrates: 2. Data for polymers." Electrophoresis **25**(2): 203-213.
- Knox, J. H. and McCormack, K. A. (1994). "Temperature effects in capillary electrophoresis. 1: Internal capillary temperature and effect upon performance." Chromatographia **38**(3-4): 207-214.
- Kralj-Iglič, V. and Iglič, A. (1996). "A Simple Statistical Mechanical Approach to the free Energy of the Electric Double Layer Including the Excluded Volume Effect." J. Phys. II France **6**(4): 477-491.
- Krisher, A. S. (1978). "Raw Water Treatment in the CPI." Chemical Engineering **85**: 78-98.
- Lao, A. I. K., Lee, T. M. H., Hsing, I. M. and Ip, N. Y. (2000). "Precise temperature control of microfluidic chamber for gas and liquid phase reactions." Sensors and Actuators A: Physical **84**(1-2): 11-17.
- Leckband, D. and Israelachvili, J. (2001). "Intermolecular forces in biology." Quarterly Reviews of Biophysics **34**(02): 105-267.
- Lee, S.-M., Kim, K.-S., Pippel, E., Kim, S., Kim, J.-H. and Lee, H.-J. (2012). "Facile Route Toward Mechanically Stable Superhydrophobic Copper Using Oxidation-Reduction Induced Morphology Changes." The Journal of Physical Chemistry C **116**(4): 2781-2790.
- Lee, S., Choi, S. U. S., Li, S. and Eastman, J. A. (1999). "Measuring Thermal Conductivity of Fluids Containing Oxide Nanoparticles." Journal of Heat Transfer **121**(2): 280-288.
- Leighton, D. and Acrivos, A. (1985). "The lift on a small sphere touching a plane in the presence of a simple shear flow." Zeitschrift für angewandte Mathematik und Physik ZAMP **36**(1): 174-178.
- Liang, Y., Hilal, N., Langston, P. and Starov, V. (2007). "Interaction forces between colloidal particles in liquid: Theory and experiment." Advances in Colloid and Interface Science **134-135**(0): 151-166.
- Liu, Y., McFarlin, G. T., Yong, X., Kuksenok, O. and Balazs, A. C. (2015). "Designing Composite Coatings That Provide a Dual Defense against Fouling." Langmuir **31**(27): 7524-7532.
- London, F. (1930). "Zur Theorie und Systematik der Molekularkräfte." Zeitschrift für Physik **63**(3): 245-279.
- Ludlow, J. C., Kirwan, D. J. and Gainer, J. L. (1980). "Heat transfer with pulsating flow." Chemical Engineering Communications **7**(4-5): 211-218.
- Maidment, D. R. (1993). Handbook of Hydrology, New York : McGraw-Hill, c1993.

- Maltezos, G., Johnston, M., Taganov, K., Srichantaratsamee, C., Gorman, J., Baltimore, D., Chantratita, W. and Scherer, A. (2010). "Exploring the limits of ultrafast polymerase chain reaction using liquid for thermal heat exchange: A proof of principle." Applied Physics Letters **97**(26): 264101.
- Mao, H., Yang, T. and Cremer, P. S. (2002). "A Microfluidic Device with a Linear Temperature Gradient for Parallel and Combinatorial Measurements." Journal of the American Chemical Society **124**(16): 4432-4435.
- Marcinichen, J. B., Olivier, J. A., Lamaison, N. and Thome, J. R. (2013). "Advances in electronics cooling." Heat Transfer Engineering **34**(5-6): 434-446.
- Margenau, H. (1931). "The role of quadrupole forces in van der Waals attractions." Physical Review **38**(4): 747-756.
- Marshall, J. S. (2007). "Particle aggregation and capture by walls in a particulate aerosol channel flow." Journal of Aerosol Science **38**(3): 333-351.
- Martines, E., Csaderova, L., Morgan, H., Curtis, A. S. G. and Riehle, M. O. (2008). "DLVO interaction energy between a sphere and a nano-patterned plate." Colloids and Surfaces A: Physicochemical and Engineering Aspects **318**(1-3): 45-52.
- Masliyah, J. H. and Bhattacharjee, S. (2006). Electrokinetic and colloid transport phenomena. Hoboken, N.J., Wiley-Interscience.
- Matsui, T., Franzke, J., Manz, A. and Janasek, D. (2007). "Temperature gradient focusing in a PDMS/glass hybrid microfluidic chip." Electrophoresis **28**(24): 4606-4611.
- Mavraki, E., Moschou, D., Kokkoris, G., Vourdas, N., Chatzandroulis, S. and Tserepi, A. (2011). "A continuous flow μ PCR device with integrated microheaters on a flexible polyimide substrate." Procedia Engineering **25**(0): 1245-1248.
- Milner, S. T., Witten, T. A. and Cates, M. E. (1988). "Theory of the grafted polymer brush." Macromolecules **21**(8): 2610-2619.
- Miralles, V., Huerre, A., Malloggi, F. and Jullien, M.-C. (2013). "A review of heating and temperature control in microfluidic systems: techniques and applications." Diagnostics **3**(1): 33-67.
- Miralles, V., Huerre, A., Williams, H., Fournie, B. and Jullien, M.-C. (2015). "A versatile technology for droplet-based microfluidics: thermomechanical actuation." Lab on a Chip **15**(9): 2133-2139.
- Mollinger, A. M. and Nieuwstadt, F. T. M. (1996). "Measurement of the lift force on a particle fixed to the wall in the viscous sublayer of a fully developed turbulent boundary layer." Journal of Fluid Mechanics **316**: 285-306.
- Moschandreou, T. E., Ellis, C. G. and Goldman, D. (2010). "Mass transfer in a rigid tube with pulsatile flow and constant Wall Concentration." Journal of Fluids Engineering **132**(8): 081202.
- Müller-Steinhagen, H., Malayeri, M. R. and Watkinson, A. P. (2011). "Heat exchanger fouling: mitigation and cleaning strategies." Heat Transfer Engineering **32**(3-4): 189-196.

Muller-Steinhagen, H. M. (1993). Fouling: the ultimate challenge for heat exchanger design. The sixth International Symposium on Transport Phenomena in Thermal Engineering. Seoul, Korea: 1-13.

MÜller-Steinhagen, H. M. and Middis, J. (1989). "Particulate fouling in plate heat exchangers." Heat Transfer Engineering **10**(4): 30-36.

Mustin, B. and Stoeber, B. (2010). "Deposition of particles from polydisperse suspensions in microfluidic systems." Microfluidics and Nanofluidics **9**(4-5): 905-913.

Mustin, B. and Stoeber, B. (2016). "Single layer deposition of polystyrene particles onto planar polydimethylsiloxane substrates." Langmuir **32**(1): 88-101.

Napper, D. H. (1969). "The steric stabilization of hydrosols by nonionic macromolecules." Journal of Colloid and Interface Science **29**(1): 168-170.

Nazemifard, N., Masliyah, J. H. and Bhattacharjee, S. (2006a). "Particle deposition onto charge heterogeneous surfaces: Convection-diffusion-migration model." Langmuir **22**(24): 9879-9893.

Nazemifard, N., Masliyah, J. H. and Bhattacharjee, S. (2006b). "Particle deposition onto micropatterned charge heterogeneous substrates: Trajectory analysis." Journal of Colloid And Interface Science **293**(1): 1-15.

Newson, I. H., Miller, G. A., Haynes, J. W., Bott, T. R. and Williamson, R. D. (1988). Particulate fouling: studies of deposition, removal and sticking mechanisms in a haematite/water system. UK National Conference on Heat Transfer. Glasgow, United Kingdom.

Ninham, B. W. and Parsegian, V. A. (1970). "van der Waals Forces." Biophysical Journal **10**(7): 646-663.

Nosonovsky, M. and Bhushan, B. (2009a). "Multiscale effects and capillary interactions in functional biomimetic surfaces for energy conversion and green engineering." Philosophical Transactions of the Royal Society of London A: Mathematical, Physical and Engineering Sciences **367**(1893): 1511-1539.

Nosonovsky, M. and Bhushan, B. (2009b). "Superhydrophobic surfaces and emerging applications: Non-adhesion, energy, green engineering." Current Opinion in Colloid & Interface Science **14**(4): 270-280.

Park, J. E. and Thome, J. R. (2010). "Critical heat flux in multi-microchannel copper elements with low pressure refrigerants." International Journal of Heat and Mass Transfer **53**(1-3): 110-122.

Parkinson, G. and Price, W. (1984). "Getting the most out of cooling water." Chemical Engineering: 22-25.

Pashley, R. M. and Israelachvili, J. N. (1984). "DLVO and hydration forces between mica surfaces in Mg²⁺, Ca²⁺, Sr²⁺, and Ba²⁺ chloride solutions." Journal of Colloid and Interface Science **97**(2): 446-455.

Perry, J. and Kandlikar, S. (2008). "Fouling and its mitigation in silicon microchannels used for IC chip cooling." Microfluidics and Nanofluidics **5**(3): 357-371.

- Piazza, R. (2008). "Thermophoresis: moving particles with thermal gradients." Soft Matter **4**(9): 1740-1744.
- Prieve, D. C. and Russel, W. B. (1988). "Simplified predictions of Hamaker constants from Lifshitz theory." Journal of Colloid and Interface Science **125**(1): 1-13.
- Rabinovich, Y. I. and Derjaguin, B. V. (1988). "Interaction of hydrophobized filaments in aqueous electrolyte solutions." Colloids and Surfaces **30**(3-4): 243-251.
- Ruckenstein, E. and Manciu, M. (2002). "The coupling between the hydration and double layer interactions." Langmuir **18**(20): 7584-7593.
- Ruckenstein, E. and Prieve, D. C. (1976). "Adsorption and desorption of particles and their chromatographic separation." AIChE Journal **22**(2): 276-283.
- Sabirianov, R. F., Rubinstein, A. and Namavar, F. (2011). "Enhanced initial protein adsorption on engineered nanostructured cubic zirconia." Physical Chemistry Chemical Physics **13**(14): 6597-6609.
- Saffman, P. G. (1965). "The lift on a small sphere in a slow shear flow." Journal of Fluid Mechanics **22**(02): 385-400.
- Salim, M., Wright, P. C. and McArthur, S. L. (2009). "Studies of electroosmotic flow and the effects of protein adsorption in plasma-polymerized microchannel surfaces." Electrophoresis **30**(11): 1877-1887.
- Sanders, R. S., Chow, R. S. and Masliyah, J. H. (1995). "Deposition of Bitumen and Asphaltene-stabilized emulsions in an impinging jet cell." Journal of Colloid and Interface Science **174**(1): 230-245.
- Selva, B., Cantat, I. and Jullien, M.-C. (2011). "Temperature-induced migration of a bubble in a soft microcavity." Physics of Fluids **23**(5): 052002.
- Song, L. and Elimelech, M. (1993). "Calculation of particle deposition rate under unfavourable particle-surface interactions." Journal of the Chemical Society, Faraday Transactions **89**(18): 3443-3452.
- Song, L. and Elimelech, M. (1995). "Particle deposition onto a permeable surface in laminar flow." Journal of Colloid And Interface Science **173**(1): 165-180.
- Spielman, L. A. and Friedlander, S. K. (1974). "Role of the electrical double layer in particle deposition by convective diffusion." Journal of Colloid And Interface Science **46**(1): 22-31.
- Stamm, M. T., Gudipaty, T., Rush, C., Jiang, L. and Zohar, Y. (2011). "Particle aggregation rate in a microchannel due to a dilute suspension flow." Microfluidics and Nanofluidics **11**(4): 395-403.
- Stern, O. (1924). "The theory of the electrolytic double shift." Z. Elektrochem **30**: 508-516.
- Suganthi, K. S. and Rajan, K. S. (2012). "Temperature induced changes in ZnO-water nanofluid: Zeta potential, size distribution and viscosity profiles." International Journal of Heat and Mass Transfer **55**(25-26): 7969-7980.

Sureda, M., Miller, A. and Diez, F. J. (2012). "In situ particle zeta potential evaluation in electroosmotic flows from time-resolved microPIV measurements." Electrophoresis **33**(17): 2759-2768.

Suzuki, A., Ho, N. F. H. and Higuchi, W. I. (1969). "Predictions of the particle size distribution changes in emulsions and suspensions by digital computation." Journal of Colloid and Interface Science **29**(3): 552-564.

Tabor, D. and Winterton, R. H. S. (1969). The Direct Measurement of Normal and Retarded van der Waals Forces.

Tijing, L. D., Kim, H. Y., Lee, D. H., Kim, C. S. and Cho, Y. I. (2010). "Physical water treatment using RF electric fields for the mitigation of CaCO₃ fouling in cooling water." International Journal of Heat and Mass Transfer **53**(7-8): 1426-1437.

Tipping, E. (1988). "Colloids in the aquatic environment." Chemistry and Industry CHINAG **15**.

Troup, D. H. and Richardson, J. A. (1978). "Scale nucleation on a heat transfer surface and its prevention." Chemical Engineering Communications **2**(4-5): 167-180.

Tuckerman, D. B., Pease, R. F. W., Guo, Z., Hu, J. E., Yildirim, O., Deane, G. and Wood, L. (2011). "Microchannel heat transfer: early history, commercial applications, and emerging opportunities." ASME Conference Proceedings **2011**(44649): 739-756.

Unni, H. N. (2007). Transport and Deposition of Colloidal Particles in MicroChannel Flow. Ph.D. Dissertation, Nanyang Technological University.

Unni, H. N. and Yang, C. (2009). "Colloidal particle deposition from electrokinetic flow in a microfluidic channel." Electrophoresis **30**(5): 732-741.

Velve Casquillas, G., Fu, C., Le Berre, M., Cramer, J., Meance, S., Plecis, A., Baigl, D., Greffet, J.-J., Chen, Y., Piel, M. and Tran, P. T. (2011). "Fast microfluidic temperature control for high resolution live cell imaging." Lab on a Chip **11**(3): 484-489.

Verwey, E. J. W. and Overbeek, J. T. G. (1948). "Theory of the stability of lyophobic colloids." Nature **162**: 315-316.

Vigolo, D., Rusconi, R., Piazza, R. and Stone, H. A. (2010). "A portable device for temperature control along microchannels." Lab on a Chip **10**(6): 795-798.

Vrij, A. (1976). "Polymers at interfaces and the interactions in colloidal dispersions." Pure and Applied Chemistry **48**(4): 471-483.

Wagner, W. and Pruß, A. (2002). "The IAPWS Formulation 1995 for the thermodynamic properties of ordinary water substance for general and scientific use." Journal of Physical and Chemical Reference Data **31**(2): 387-535.

Wang, P. and Keller, A. A. (2009). "Natural and engineered nano and colloidal transport: role of zeta potential in prediction of particle deposition." Langmuir **25**(12): 6856-6862.

Wang, S. (1927). "The mutual influence between the two atoms of hydrogen." Zeitschrift für Physik **28**: 663-666.

- Wu, J., Cao, W., Wen, W., Chang, D. C. and Sheng, P. (2009). "Polydimethylsiloxane microfluidic chip with integrated microheater and thermal sensor." Biomicrofluidics **3**(1): 012005.
- Yan, Z., Huang, X. and Yang, C. (2015). "Deposition of colloidal particles in a microchannel at elevated temperatures." Microfluidics and Nanofluidics **18**(3): 403-414.
- Yang, C., Dabros, T., Li, D., Czarnecki, J. and Masliyah, J. H. (1998). "Kinetics of particle transport to a solid surface from an impinging jet under surface and external force fields." Journal of Colloid And Interface Science **208**(1): 226-240.
- Yang, J., Liu, Y., Rauch, C. B., Stevens, R. L., Liu, R. H., Lenigk, R. and Grodzinski, P. (2002). "High sensitivity PCR assay in plastic micro reactors." Lab on a Chip **2**(4): 179-187.
- Yap, Y.-F., Tan, S.-H., Nguyen, N.-T., Sohail Murshed, S. M., Wong, T.-N. and Yobas, L. (2009). "Thermally mediated control of liquid microdroplets at a bifurcation." Journal of Physics D: Applied Physics **42**(6): 065503.
- Yiantsios, S. G. and Karabelas, A. J. (1995). "Detachment of spherical microparticles adhering on flat surfaces by hydrodynamic forces." Journal of Colloid And Interface Science **176**(1): 74-85.
- Yiantsios, S. G. and Karabelas, A. J. (1998). "The effect of gravity on the deposition of micron-sized particles on smooth surfaces." International Journal of Multiphase Flow **24**(2): 283-293.
- Yiantsios, S. G. and Karabelas, A. J. (2003). "Deposition of micron-sized particles on flat surfaces: effects of hydrodynamic and physicochemical conditions on particle attachment efficiency." Chemical Engineering Science **58**(14): 3105-3113.
- Zhang, L.-x., Chen, Y.-b., Gao, M., Li, X. and Lin, Z.-h. (2016). "Validation of electronic anti-fouling technology in the spray water side of evaporative cooler." International Journal of Heat and Mass Transfer **93**: 624-628.
- Zhao, C., Ebeling, D., Siretanu, I., van den Ende, D. and Mugele, F. (2015). "Extracting local surface charges and charge regulation behavior from atomic force microscopy measurements at heterogeneous solid-electrolyte interfaces." Nanoscale **7**(39): 16298-16311.
- Zhao, Y., Zhao, C., He, J., Zhou, Y. and Yang, C. (2013). "Collective effects on thermophoresis of colloids: a microfluidic study within the framework of DLVO theory." Soft Matter **9**(32): 7726-7734.

Appendix A

Parameters for temperature dependence of water properties

Table A.1 Parameter table for the calculation of the static dielectric constant, ϵ , in Eq. 3.35

Symbol	Parameter	Value
g	Harris-Alderg-factor	
k	Boltzmann constant	$1.380658 \times 10^{-30} \text{ J K}^{-1}$
M_w	Molar mass of water	$0.018015268 \text{ kg/mol}$
N_A	Avogadro number	$6.0221367 \times 10^{23}/\text{mol}$
ϵ_0	Permittivity of vacuum	$8.85 \times 10^{-12} \text{ C/V m}$
T_c	Critical temperature	647.096 K
α	Mean molecular polarizability of the isolated water molecule	$1.636 \times 10^{-40} \text{ C}^2 \text{J}^{-1} \text{ m}^2$
μ	Dipole moment of the isolated water molecule	$6.138 \times 10^{-30} \text{ C m}$
ρ_c	Critical density	$322/M_w \text{ mol/m}^{-3}$
ρ	Amount of substance (molar) density	
T	Absolute temperature, ITS-90	

Table A.2 Coefficient for calculation of Harris-Alderg-factor, g in Eq. 3.36

h	N_h	i_h	j_h
1	0.978224486826	1	0.25
2	-0.957771379375	1	1
3	0.237511794148	1	2.5
4	0.714692244396	2	1.5
5	-0.298217036956	3	1.5
6	-0.108863472196	3	2.5
7	$0.949327488264 \times 10^{-1}$	4	2
8	$-0.980469816509 \times 10^{-2}$	5	2
9	$0.165167634970 \times 10^{-4}$	6	5
10	$0.937359795772 \times 10^{-4}$	7	0.5
11	$-0.123179218720 \times 10^{-9}$	10	10
12	$0.196096504426 \times 10^{-2}$		
$\rho_c = 322/M_w \text{ mol/m}^{-3}$		$T_c = 647.096 \text{ K}$	

Table A.3 Coefficient for calculation of the refractive index, n , in Eq. 3.40

$a_0 = 0.244257733$	$a_4 = 1.58920570 \times 10^{-3}$
$a_1 = 9.74634476 \times 10^{-3}$	$a_5 = 2.45934259 \times 10^{-3}$
$a_2 = -3.73234996 \times 10^{-3}$	$a_6 = 0.900704920$
$a_3 = 2.68678472 \times 10^{-4}$	$a_7 = -1.66626219 \times 10^{-2}$
$\bar{\lambda}_{UV} = 0.229202$	$\bar{\lambda}_{IR} = 5.432937$

Appendix B

Protocol for ITO glass etching

Note: This protocol is optimised for the MEMS facility in the Clean Room of School of Mechanical & Aerospace Engineering, NTU. Setting parameters could be varied if equipment are different.

1. Clean ITO glass plates:

- i. Immerse the ITO glass in acetone with ultra-sound on for 2 minutes.
- ii. Immerse in Isopropanol (IPA) with ultra-sound on for 1 minute..
- iii. Rinse in DI water and blow dry.
- iv. Heat the ITO glass on hot plate at 120 C for 4 minutes.

2. Photoresist spin coat (~ 2 um thick coat):

For photoresist AZ9260 (AZ7220)

- i. Parameter set:

pre-spin speed = 500 rpm

pre-spin time = 10 sec

spin speed = 5000 rpm (2000)

spin time = 30 sec

- ii. Photoresist coat:

- a. Put a piece of ITO glass on the spinner with the ITO coated side up, and then fix it by vacuum.
- b. Pour the positive photoresist onto the center of the glass plate and spread it all over the plate.
- c. Press the “Start” button to begin spinning and “stop”

- d. Probably, there will be some PR which get around the corners and adhere to the bottom side of the glass. Remove it by clean room wiper with acetone. This is an important step to ensure good exposure on corners.
 - e. Bake on the hotplate at 100 C – 1 min and 110 C – 3 mins. (Bake on hotplate at 100 for 90 sec for AZ7220)
3. UV Exposure - ~ 35 to 40 sec (15-20 sec for AZ7220)
- i. Place the mask on the glass plate using tape to bind it tightly and fix it onto the rectangular mask-holder
 - ii. Put the mask-holder onto the machine after turning vacuum on
 - iii. Set parameters to soft, 45 s exposure time.
 - iv. Load the cooled and resist coated ITO glass slide onto the wafer holder and align it using the 4 holes in the corners of the wafer holder
 - v. Adjust the left, right and center scales to 10, 15 and center line respectively. Loss of wafer vacuum is ok
 - vi. Expose the substrate
 - vii. Unload the substrate and repeat for the next 5 substrates
4. No post bake for AZ 9260. Post bake at 110 C for 60 sec for AZ 7220
5. Photoresist develop
- i. Pour the respective developer into the small container (dilute twice for AZ9260 and no dilution for AZ7220)
 - ii. Transfer the glass plates into the developer and stir the container for 4 mins for AZ 9260 (2 mins for AZ 7220)
 - iii. Transfer the glass slides into the DI water container
 - iv. Clean the glass slide with DI water and blow dry.
 - v. Test the patterns using the microscope if required develop further.
 - vi. If there are any regions where two electrodes are in contact, use a tissue dipped in acetone to remove the photoresist layer and hence to detach the patterns from each other

6. Bake the glass plated at 120 C for 45 mins
7. ITO etching
 - i. Wear all the PPE and take extreme caution while using the acids and their mixtures.
Always add acid to water.
 - ii. Add $\text{HCl}:\text{H}_2\text{O}:\text{HNO}_3$ into the glass container in the ratio 4:2:1
 - iii. Place the glass plates into the etching solution for 4 mins.
 - iv. Clean the glass plates with water and blow dry.
 - v. Test the glass slide for conductivity. If the surface is non-conductive (other than the electrode patterns) the etching process is complete. If the surface is conductive, etch the glass plates for another min.
 - vi. Clean the wet bench area and transfer the etching solution into the waste container within the wet bench.
8. Photo resist removal
 - i. Immerse the glass slide into acetone for few seconds
 - ii. Wash the glass slide with IPA and water and blow dry.

Publications arising from this thesis

Journal article:

Yan, Z., Huang, X. and Yang, C. (2015). "Deposition of colloidal particles in a microchannel at elevated temperatures." Microfluidics and Nanofluidics **18**(3): 403-414.

Conference article and presentation:

Yan, Z.; Huang, X.; Yang, C. (2016). "Particulate fouling and mitigation approach in microchannel heat exchanger." In ASME 5th International Conference on Micro/Nanoscale Heat and Mass Transfer; 4 - 6 January 2016, Biopolis, Singapore, American Society of Mechanical Engineers: 2016, p V001T03A007.

Yan, Z.; Huang, X.; Yang, C. (2014). "Experimental study of thermal effect on particle deposition in a hydrodynamic Flow." In 5th International Conference on Heat Transfer and Fluid Flow in Microscale; 22 - 26 April 2014, Marseilles, France.